2008-09-24

Mechanistic Investigation of Ash Deposition in Pulverized-Coal and Biomass Combustion

Shrinivas Sadashiv Lokare
Brigham Young University - Provo

A MECHANISTIC INVESTIGATION OF ASH DEPOSITION IN PULVERIZED-COAL AND BIOMASS COMBUSTION

by

Shrinivas S. Lokare

A dissertation submitted to the faculty of

Brigham Young University

in partial fulfillment of the requirements for the degree of

Doctor of Philosophy

Department of Chemical Engineering

Brigham Young University

December 2008

This dissertation is dedicated to

Aai and Tatya

BRIGHAM YOUNG UNIVERSITY

GRADUATE COMMITTEE APPROVAL

of a dissertation submitted by

Shrinivas S. Lokare

This thesis has been read by each member of the following graduate committee and by a majority vote has been found satisfactory.

_____	_____
Date	Larry L. Baxter, Chair
_____	_____
Date	Dale R. Tree
_____	_____
Date	Thomas H. Fletcher
_____	_____
Date	Kenneth Solen
_____	_____
Date	Merrill W. Beckstead

BRIGHAM YOUNG UNIVERSITY

As chair of the candidate's graduate committee, I have read the dissertation of Shrinivas S. Lokare in its final form and have found that (1) its format, citations, and bibliographical style are consistent and acceptable and fulfill university requirements; (2) its illustrative material including figures, tables, and charts are in place; and (3) the final manuscript is satisfactory to the graduate committee and is ready for submission to the university library.

_____ _____

Date

Larry L. Baxter
Chair, Graduate Committee

Accepted for the Department

_____

Larry L. Baxter
Graduate Coordinator

Accepted for the College

_____

Alan R. Parkinson
Dean, Ira A. Fulton College of Engineering and Technology

ABSTRACT

MECHANISTIC INVESTIGATION OF ASH DEPOSITION IN

PULVERIZED-COAL AND BIOMASS COMBUSTION

Shrinivas S. Lokare

Department of Chemical Engineering

Doctor of Philosophy

This investigation details the effects of fuel constituents on ash deposition through systematic experimental and theoretical analyses of fundamental particle experiments and a suite of fuels with widely varying inorganic contents and compositions. The experiments were carried out in the Multifuel Flow Reactor (MFR) at Brigham Young University. Fuels included several biomass fuels (straw, sawdust and mixtures of straw-sawdust with other additives such as $Al(OH)_3$, $CaCO_3$, etc.) and four commercially-used coals (Illinois#6, Powder River Basin – Caballo and Cordero, Blind Canyon, and Lignite – Beulah Zap). The data from the series of experiments quantitatively illustrate the effects of fuel properties, physical and/or chemical, on ash deposition rate mechanisms.

In deposition investigation, the most significant deposition mechanisms in a general ash deposition model – inertial impaction, condensation and eddy impaction –

were selected. In this PhD work, these three mechanisms are analyzed using simulation techniques such as Fluent and programming languages such as C++. The experimental data was collected for deposition rate measurements to provide a data set for the model validations except for eddy impaction. In this model analyses, the impaction efficiency model predictions from this work indicated lower impaction efficiencies than the traditional potential flow model presented by others (Israel 1983). The experimental data by others (Lokare 2003) and the data collected in this work support these predictions and present a new impaction efficiency correlation as a function of Stokes number. Similarly, the capture and condensation models perform well and are supported by the respective experimental data. The comprehensive ash deposition model predicts ash deposition rates within 10% of experimental data and is able to distinguish the role of various additives in recipe fuels combustion. As an additional results, NO_X behavior of Illinois#6 and PRB (Caballo) in oxyfuel combustion show evidence of inherent NO_X reducing feature of oxyfuel combustion.

ACKNOWLEDGEMENTS

I would like to thank a number of people who have provided me with a great deal of help to complete this project and dissertation work. I am grateful to my advisor, Larry L. Baxter, and Dale R. Tree, a member of my graduate committee, who supported me in dealing with the difficult and rather complicated issues involved in this investigation. I am also grateful to David Dunaway, David Moulton, Marc Anderson, Douglas Rogers, Brent Poole, Hong Lu and Bob Chan who helped me putting all the pieces of this work together. I am also thankful to Krzyzstof Waclawiak for his input and assistance as a visiting scholar to BYU during a part of this research project. I would like to thank Neal L. Adair, whose previous work on the same facility helped me understand the information regarding the facility and its operation. I am grateful to John Gardener and Michael Standing for their support in SEM analysis work.

I am thankful to Tech-wise, Denmark, Alliant Energy, EPRI, GE and US DOE for the supply of the bio-fuel suite for the experiments. I would also like to thank Helle Junker, Tech-wise for her support and encouragement towards this research work.

Finally, I express my gratitude to my parents, my brother, and my sister who have been with me at every step before and during this project completion. I am grateful to my wife, Snehal, for her constant support and love throughout this process. I would like to thank every hand that helped me directly or indirectly in completion of this project work.

TABLE OF CONTENTS

LIST OF FIGURES

LIST OF TABLES

1 Introduction

Coal represents an important energy source by humankind and has done so for couple of centuries. Although fossil fuels are currently, and will remain for some time, the major resource to meet increasing worldwide energy demands, it is imperative to search for alternate sources of energy. Along with its energy content, coal brings unwanted issues with it, such as pollutant (NO_X, SO_X, CO_2, particulate, Hg, etc.) emissions. EPA emissions regulations, periodically getting more stringent, combined with operational issues largely led to major changes in the types of coal consumed and the types of equipment used for coal conversion. Widely anticipated regulations regarding CO_2 management will undoubtedly have additional large impacts on coal conversion systems. As "renewable" and "clean" being the most desired requirements from alternate fuels, biomass may replace coal in part or in whole in power generation plants. Though there is far too little biomass to replace coal globally, cofired biomass coal plants enjoy many operational, efficiency, and cost-effective advantages not available to either dedicated coal or dedicated biomass plants (Baxter 2005, Green 1994).

During recent years, there has been extensive research related to the combustion of biomass as a single fuel as well as co-firing. Currently, forest and agricultural residues and waste represent the most widely used biomass fuels in energy production. Energy crops represent additional potential biomass resources. In existing PC-fired boilers, biomass co-fired with coal reduces some of the emissions from coal (primarily SO_X and CO_2) while increasing the energy conversion efficiency of biomass as compared to

dedicated biomass-based systems (Hein 1998). Biomass rarely competes economically with coal in the absence of carbon-emission taxes or credits, but when co-fired with coal it is often the least expensive form of renewable energy generation (Baxter 2005).

Although most biomass fuels contain low sulfur and are renewable, they have disadvantages such as extensive ash deposition and corrosion problems. Highly variable ash content and ash chemistry result in potential deposition issues in operational facilities even more widely ranging than those caused by coal ash. Coal and biomass power plant operation and design depend strongly on ash deposition and corrosion.

Ash deposition represents a long-standing operational and design issue at both practical and academic levels. Computer simulations and fuel performance indices help select proper fuels and operating conditions to reduce ash deposition problems. However, relatively little quantitative experimental data exist for validating predictions from ash deposition simulations, in general, and from deposition specifically in advanced combustion processes. Detailed and quantitative ash deposition and corrosion data and models could significantly improve thermal processing (combustion, gasification, etc.) designs and performance. Literature on qualitative deposition and corrosion mechanisms is extensive in academic journals, conference proceedings and less formal publications.

2 Literature Review

2.1 Background

Coals and other fuels used in power generation boilers vary in ash content and amount. Coal exhibits wide variations in many of its properties, including composition. One classification of coal is by rank, which correlates with the degree of coalification – a process in which vegetable matter converts into coal with anthracite as the final product– but is quantitatively based on heating value and, for the highest ranks, fixed carbon, meaning the amount of organic residue upon pyrolysis at a fixed temperature (Smith 1994).

The major coal ranks are lignite, subbituminous coal, bituminous coal and anthracite in increasing order of heating value or fixed carbon. Coal type, age, elemental composition and other properties generally correlate with rank. The lowest rank coals (lignites) contain high moisture and volatile matter, while the highest rank coals (anthracites) have low volatiles and moisture content. Similarly, inorganic materials in coals show variation depending on rank of individual coal. Low-rank coals commonly contain relatively large amounts of organically associated elements such as Na, Mg, Ca, K, and Sr present as salts of organic acid groups, as well as mineral grains, although they commonly contain less chlorine than high-rank coals. By contrast, high-rank coals commonly contain more iron and sulfur than low-rank coals. Variation in such inorganic content changes the deposition and corrosion potential of coals, thus presenting it as one

of the most investigated issues in power generation. Figure 1 presents the extent of variation in 2 different coals as well as coals and some biomass fuels which are currently among the best renewable energy options for coals. These coal and biomass fuels are the representative fuels of the fuel matrix used in this PhD work. The fuel and ash chemistry analyses for the coals were performed by WAL (Wyoming Analytical Laboratory), while the analyses for biomass fuels were performed by research colleagues in Denmark. The ultimate analysis for the coals and biomass shown in Figure 1 indicates high carbon contents in coals than biomass. Biomass generally also includes more moisture than coal, although this highly variable analysis is not included in the figure.

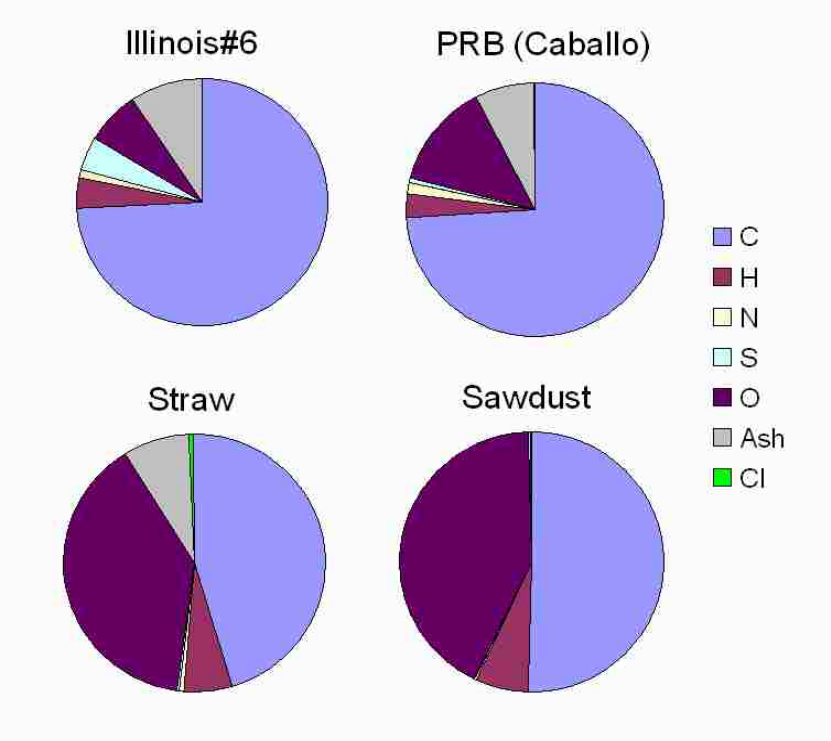

Figure 1: Variation in fuel chemistry of coals and biomass fuels. All results on a dry basis.

The ash chemistry charts in Figure 2 show that the coal ash analyses exhibit modest variation, while those for biomass fuels exhibit large variation. Biomass ash usually contains higher alkali and chlorine contents compared to coal ash while coal ash contains sulfur which is low concentration in most biomass ash and fuel. Such differences create significant changes in combustion characteristics, making it harder to accommodate a wide variety of fuels in a single furnace as described later in this section.

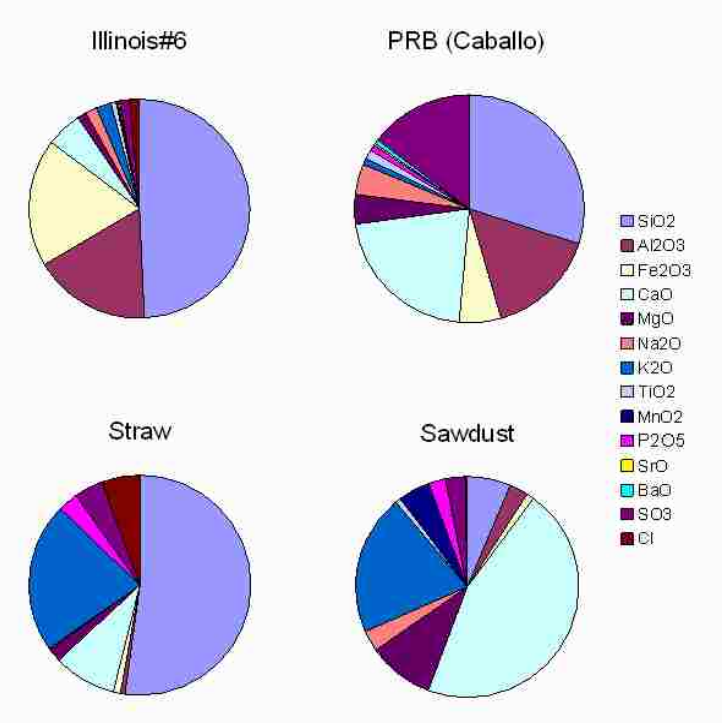

Figure 2: Variation in ash chemistry of coal and biomass fuels

The ash contents in the figure appear as oxide fractions as is traditional. However, the inorganic material does not generally occur in these oxide forms in the fuel or even after combustion. The tradition of representing the ash fractions as oxides arises from the convenience of comparing the measured total ash fraction with the sum of the oxides.

These numbers generally differ only slightly. However, the actual forms of the inorganic material include clays/silicates, carbonates, sulfides, sulfates, phosphates, and some oxides.

It is a common misunderstanding that the terms ‘inorganic material’, ‘mineral matter’, and ‘ash’ refer to the same material contained in the coal. There are important distinctions among these terms, though not all literature honors these distinctions. ‘Inorganic material’ comprises all the non-organic moieties in coal including often large fractions of material ionically or otherwise bound to the organic backbone (Baxter 2000). In contrast, ‘mineral matter’, commonly used synonymously with inorganic material, technically refers to only the mineral grains in coal and specifically does not include atomically bound or other non-mineral forms of inorganic material. ‘Ash’ is one of the products of coal combustion which is not the same as the inorganic material or mineral matter in the coal but is the solid residue resulting from complete fuel oxidation. Because mineral species commonly include hydrates, carbonates, and sulfates that are less prevalent or absent in ash, the mass of inorganic material in coal generally exceeds the mass of coal ash by 10-15%.

Slagging generally denotes deposition of fly ash on heat-transfer surfaces and refractory in the furnace volume primarily subjected to radiant heat transfer, not necessarily implying the formation of molten material despite the implication of the term. Fouling denotes deposit formation on convective heat transfer surfaces (Bryers 1996). The quantity and characteristics of ash deposited through these two major pathways, fouling and slagging, are major concerns to design and operation of the equipment. While the combustion characteristics of coal play a role in sizing the furnace, the net deposition

of the ash is the primary consideration driving the overall size, geometry and, operating conditions of the boiler.

The pre-combustion fuel-related factors that affect deposition are inorganic content (amount and composition) within coals and particle size distribution. Inorganic material in pulverized coal exists either as included (i.e. associated with or contained within a carbonaceous coal particle), or "excluded" (i.e. not having any carbonaceous material associated with it) material (Smith 1994). Depending on whether the minerals (e.g. pyrites) are included or excluded, ash formation proceeds differently. Srinivasachar and others (Srinivasachar 1990; Srinivasachar 1990; Wall 1992) showed that inclusion or exclusion of the minerals affects the surface characteristics of ash particles (see Figure 3).

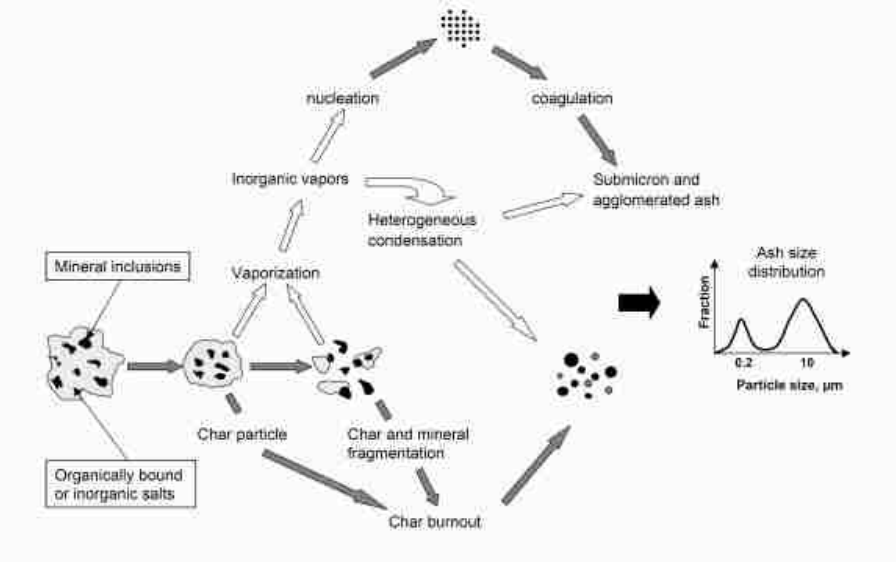

Figure 3: Mineral matter transformation during pulverized coal combustion

For example, particle stickiness depends on magnetite crystallization time during pyrite transformation. The mineral distribution also determines the ash particles size.

Included minerals tend to produce smaller ash particles than excluded minerals. However, excluded minerals fragment more extensively due to inner gas expansion at high temperatures producing smaller ash particles. Following the fragmentation of excluded minerals and/or release of included minerals, these small particles coalesce and produce larger ash particles. This coalescence depends on particle composition and combustion temperature. Vapor formation from inorganic species, and subsequent recondensation, forms the smallest fly ash particles. Post combustion research in deposition mainly involves ash deposit properties such as thermal conductivity, porosity, emissivity, etc. and dependence of these parameters on combustion conditions. As ash deposits grow, their thickness increases and porosity decreases due to sintering, consolidation and slagging, which increase deposit thermal conductivity (Baxter 1998; Baxter 2000; Robinson 2001; Robinson 2001). Many researchers described the connection between the physical structures of a deposit and its radiative properties qualitatively and mechanistically. The absorptivity and emittance are the most important factors in predicting the thermal behavior of ash deposits in the radiant section of combustors while the thermal conductivity plays a dominant role in the convective and a secondary role in the radiant sections (Baxter 1988; Baxter 1993; Wall 1993; Wall 1995; Wall T.F. 1996; Baxter 1998; Baxter 2001; Zbogar, Frandsen et al. 2005). Inorganic transformation not only affects the chemistry, but also the size distribution of ash particles as shown in Figure 4. Lokare (Lokare 2003) demonstrated the variation in ash particle size distribution from the combustion of fuels with similar fuel particle size distributions. This significant variation is partly due to varying ash content and partly due to mineral inclusions/exclusions. These ash particles of varying sizes and masses undergo

different ash deposition mechanisms described in next subsection. Heavier particles deposit primarily through inertial impaction while light particles deposit through eddy impaction and/or thermophoresis. Vapors and gases also deposit on surfaces, typically through condensation and heterogeneous reactions, respectively.

2.2 Ash deposition mechanisms

Fouling and slagging are complex phenomena depending on: (a) transformation of the inorganic components of ash in fuels; (b) chemical reactions between gas, liquid, and solid phases in suspension and on surfaces; (c) reaction kinetics and species transport rates; and (d) attachment of ash particles to surfaces and the release of deposited liquids and solids (Bryers 1996). Thus, it is apparent that fireside problems cannot be simply represented by a single rate of deposition on a target by ash characterized by a single elemental analysis. Deposits form by at least five mechanisms: Inertial Impaction, Thermophoresis, Condensation, Eddy Impaction, and Chemical Reaction (Baxter 1993). Each of these mechanisms has a specific driving force, namely momentum, temperature gradients, vapor pressure of alkali salt vapors, turbulence intensity, and species concentration gradients, respectively. This leads to a large range of parameters controlling each of these mechanisms. A deposition rate based on these mechanisms is described by 2.1.

$$\frac{dm}{dt} = I \bullet G + E + T + C + R \qquad 2.1$$

Where:

I = Inertial impaction rate, G = Capture efficiency, E = Eddy impaction rate, T = Thermophoretic deposition rate, C = Condensation rate, R = Chemical reaction rate.

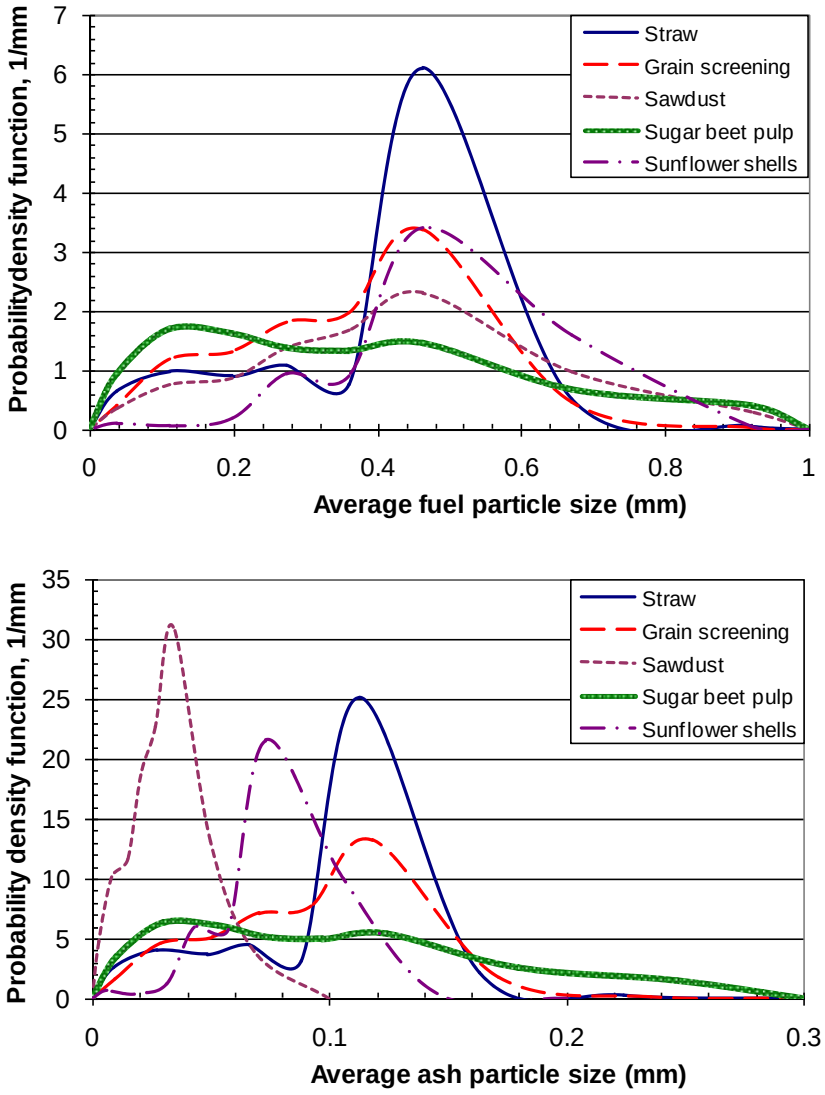

Figure 4: Fuel (Top) and Ash (Bottom) particle size distribution for different biomass fuels (Lokare 2003)

***Inertial impaction**:*

Inertial impaction is typically the primary source of ash deposition on superheater boiler tubes. Inertial impaction takes place when the momentum of the particle toward the tube is large enough to overcome drag forces produced by fluid flow, which direct particles around the tube. As a result, particles pass through the boundary layer and

stagnation zone, and impact the tube. The particle capture efficiency describes the propensity of these particles to stay on the surface once they impact. Both particle and surface properties such as the roughness of a metal surface and surface tension force play significant roles in determining the particle capture efficiency. A more detailed discussion of this mechanism including the capture efficiency is given below as it is assumed to be the major pathway for the ash to deposit on superheater tubes.

Eddy impaction:

Eddy impaction involves fine ash particles that entrained in turbulent eddies. These eddies add momentum to the particles and disrupt steady streamlines such that they have enough momentum to impact tube surfaces even though they would be too small to impact based on average gas velocities. Particles deposited by eddy impaction are usually too small to deposit via inertial impaction. Since turbulent eddies are difficult to describe, this process is less understood than any of the processes discussed in this section, and its description is related mainly to empirical coefficients. Eddy impaction is relevant only for small particles.

Thermophoresis*:*

Thermophoresis is the process of particle motion in a gas due to local temperature gradients. Thermophoretic forces on a particle may be induced either by temperature gradient in the gas in which the particle is suspended, or as a consequence of temperature gradient in the particle itself. In general, these forces act in the direction opposite to that of the temperature gradient, although they can act in the direction of the gradient under certain conditions of particle surface temperature. Thermophoretic deposits are finer grained (sub-micron particles) and more evenly distributed around a tube surface than

deposits formed by inertial impaction. Deposit accumulation on the tube surface decreases the temperature gradient in the thermal boundary layer, decreasing the rate of thermophoresis.

***Condensation**:*

Condensation is the mechanism by which vapors (mainly alkali chlorides) are collected on cooled heat transfer surfaces. If the partial pressure of a vapor at the relatively cold temperature of a tube exceeds the vapor pressure, the vapor will condense on the tube. However, the vapor pressure of alkali chlorides depends on the concentration of the chlorides in the gas phase; therefore condensation of alkali salts is also governed by the mass fraction of the salts in the fuel. All vapors that enter the thermal boundary layer around a heat transfer surface are assumed to become deposited on the surface. Condensates are common in fuels such as biomass and low-grade coal, which contain higher inorganic materials compared to other fuels. Condensates are deposited more evenly on tube surfaces compared to the previously mentioned mechanisms of ash deposition. However, condensation is favored at the leading edge of tube compared to the trailing edge due to high degrees of heat and mass transfer at the leading edge.

Chemical reaction:

Heterogeneous chemical reactions between the gas and either the existing deposit materials or the deposit surfaces can also add or remove mass. The rate of conversion depends on mass transfer rates to the surface and on chemical kinetics of the heterogeneous reactions involved. Among the most important chemical reactions with respect to ash deposition are 1) sulfation, 2) alkali absorption, and 3) oxidation. The principle sulfating species of concern are compounds containing the alkali metals such as

sodium and potassium. These elements readily form hydroxides that easily sulfate under the given conditions. Silica absorbs alkali material to form silicates. Silicates (SiO_3^{2-}) are less rigid and melt at lower temperature than silica (SiO_2). The transformations of silica to silicates in deposits can induce sintering and significant changes in deposit properties. These reactions are slow relative to sulfation.

***Other mechanisms**:*

There are several other mechanisms of deposit growth other than those described above. Among these are electrostatic interactions, photophoresis, and Brownian motion. There is not enough evidence to suggest that these mechanisms are significant contributors to deposit formation, hence they are not discussed in detail here.

Boiler design and operation, especially combustion chamber aerodynamics, also effect boiler deposition since highly swirling flows may throw particles to the transfer surfaces, resulting in enhanced deposition (Baxter 1993; Hein 1996; Huang 1996; Jensen 1997; Baxter 2000; Kaufmann 2000; Das 2003). According to Lee (Lee 1999), the amount of fly ash particles trapped in the boundary layer and the particle arrival rate are very sensitive to particle size and density. Pyykonen et al. (Pyykonen and Jokiniemi 2003) present model results on fume particle and condensable alkali chloride vapor behavior in superheater tube boundary layers. Simulations of alkali chloride behavior in the heat exchanger section of a boiler indicate that both boundary layer condensation and subsequent particle thermophoretic deposition and direct vapor deposition are significant deposition mechanisms for alkali chlorides. Critical deposit properties such as thermal conductivity and strength depend strongly on deposit microstructure (Zbogar, Frandsen et al. 2005). The measurements indicated that high-temperature deposits have more

interconnected and coarser structure than the low-temperature deposits. These differences arise from the effects of particle temperature on deposit microstructure. Higher-temperature conditions create deposits with more porous structure but whose particles are more interconnected because of sintering and deformation (Kweon 2003).

Several researchers have investigated how submicron particle deposition relates to temperature differences in a boiler radiant section and relatively cooler superheater sections. Rosner and coworkers (Eisner 1986; Rosner 1986; Rosner 2000) show that thermophoresis dominated Brownian diffusion by factors up to about 1000 during submicron particle deposition from sooting, premixed hydrocarbon/air flames. Mackowski (Mackowski 1990; Mackowski 1994) demonstrate that, apart from size, the submicron particle deposition is affected by particle shape and symmetry. Thermal slip forces arising from radiative cooling of an asymmetric particle can lead to significant thermophoretic velocities. Costen et al. (Costen 2000) show that without the incorporation of the effect of thermophoresis, particles below 10 micron do not deposit significantly and remain trapped in the flow because of their lower momentum and reduced ability to penetrate viscous boundary layers. Thus, both the deposition rate and deposition pattern of finer particles depend on operating conditions, namely, furnace aerodynamics, and the thermophoretic effects.

2.3 Biomass ash deposition

Biomass can be a CO_2-neutral alternative to coal, either as a co-fired fuel in a coal-based system or in a dedicated biomass system (Green 1994; Hein 1998; Jenkins 1998). Biomass fuels represent one of the best solutions for both increased energy and reduced net CO_2 production. However, biomass in many combustion systems can

produce severe ash deposition and corrosion. Ash deposition rates for biomass fuels can vary greatly compared to coal, due to significant differences in fuel composition. For example, ash in wood is generally very low (1-3%) while that in straw is as high as 14-21%. Wood ash is very rich in calcium as calcite or carbonate (about 50-60%) with minor amounts of quartz (10% or less), while straw ash has a high content of alkali chlorides and silicates (Jensen 1997; Heinzel 1998). Lokare et al. (Lokare 2006) show the influence of fuel chemistry on ash deposition rates of biomass fuels. Making an appropriate choice of biomass fuels based on the ash chemistry and mixing them in proper ratio can lead to reduced deposition and corrosion rates.

Although potassium occurs in minor concentrations in biomass fuel compared to silica, its level of concentration is 4-5 times that found in coal and generally high compared to most fuels. Similarly, chlorine content of biomass is higher than that of coal, which leads to some biomass fuels producing high concentrations of alkali chloride in combustion gas. These gas-phase alkali chlorides form a smooth and sticky condensed layer on superheater tubes enhancing ash deposition processes (Baxter 1998; Kaufmann 2000; Coda 2001; Bakker 2002; Lokare 2003). Agricultural waste products, such as straws, can have large ash fractions, with alkali chlorine and silica as the major constituents. These alkali salts also play a significant role in deposition due to their ability to bind ash particles together through sintering or chemical reactions. These higher degrees of ash deposition are sometimes associated with corrosion. Alkali, chlorine and silicates are the main fractions of the ash deposit irrespective of the fuel type. The differences in absolute amounts of these compounds are due to the elemental fuel composition and the combustion properties. Thermodynamically, alkali chlorides are the

most stable form of alkali and chlorine in the gas phase at flame temperatures (Wall 1995; Jenkins 1998). When chlorine presence in the fuel is negligible, corrosion can still proceed by the formation of sulfates in large amounts at high surface temperatures. In particular, alkali trisulfates are known to be aggressive on heat transfer surfaces (Robinson 1998).

2.4 Deposit chemistry and corrosion

In all coal/biomass-fired boilers, the problems of ash deposition are accompanied by corrosion issues. Corrosion mainly depends on fuel inorganic chemistry and operating conditions. The release mechanisms of the inorganic content depend on boiler operating conditions. This may lead to different pathways for compounds that initiate or accelerate the corrosion process. In pulverized-coal-fired boilers, high-temperature corrosion due to chlorine is potentially troublesome. The forms in which chlorine occurs are important as they determine the mineral transformation during combustion, which ultimately affects the fireside behavior of the species, and their potential for removal during the fuel preparation as a remedial measure for fireside problems (Bryers 1996). The cycle of high-temperature corrosion begins with the condensation of chlorine through salt vapors and/or gaseous Cl_2 released by the coal, which penetrates the initial oxide scale and reacts with elemental iron to form $FeCl_2$, physically separating the protective oxide coating and corrosion product from the tube surface. The $FeCl_2$ vapor diffuses outward through the oxide scale and on its way is oxidized to Fe_3O_4 and Fe_2O_3, releasing fresh Cl_2 for attack of base metal (Lokare 2003; Lokare 2006). The cyclic occurrence of reducing and oxidizing conditions at a particular location strongly affect corrosion rates, since reducing conditions are essential to releasing the initial Cl_2, while oxidizing conditions are

required for the corrosion to proceed. Lee (Lee 1999) reports that $FeCl_2$ has a specific volume 11 times that of the reacted metal. $FeCl_2$ formation creates non-protective porous scales. On low temperature surfaces, HCl may react with the protective coating of Fe_2O_3 to form $FeCl_3$. Experiments by Mayer and Manulesco (Bryers 1996) indicated 0.2 volume percent of HCl can make a Fe_2O_3 layer porous while 0.8 volume percent will completely disintegrate the layer. The $FeCl_3$ is volatile and will not remain on tube surfaces in most steam generators.

Corrosion associated with sulfur depends on the boiler temperature profile. The products of sulfur (e.g. pyrosulfates, trisulfates) tend to have relatively low melting points, and even lower melting points in the case of the eutectic mixtures formed with silicates. The pyrosulfates form under reducing conditions, and corrosion depends on a molten phase. For high-temperature corrosion due to sulfur, the presence of alkali pyrosulfates in furnace wall deposits and alkali-iron trisulfates on the leading edge of the final superheater tube surface are the primary cause for tube wastage. The sulfates interact with Fe_2O_3 in ash and, with SO_3 present at the tube surface, to form alkali trisulfates. Research on alkali trisulfates reveals that high-temperature corrosion of furnace walls and superheater surfaces is minimized by maintaining an oxidizing environment and avoiding flame impingement on furnace walls, limiting steam temperatures to approximately 537^{o}C, using shielding to raise exposed surfaces to temperatures exceeding the melting temperatures of the alkali trisulfates and restricting the sulfur (i.e. iron level) and alkali level of high alkali bituminous coals (Bryers 1996).

Researchers propose various mechanisms for corrosion. Gas-phase corrosion attack may be caused by several chlorine-containing species, the most common being

HCl and Cl_2 (Baxter 1993; Hein 1996; Kaufmann 2000). There are two mechanisms proposed in the literature describing how solid-phase chlorides in deposits may affect corrosion. The first mechanism involves generation of gaseous chlorine from sulfation of alkali chlorides or by reaction between the chlorides in the deposit and the metal scale, followed by a mechanism similar to the gas-phase corrosion. The second mechanism involves formation of low-temperature eutectics from chlorides that may flux the oxide layer. In the solid deposit layer, potassium chloride reacts with gaseous SO_2 and/or SO_3 to form condensed potassium sulfate that is thermodynamically stable at those conditions. After sulfation, the released gaseous Cl-species diffuses back to the metal surface to follow the gas-phase corrosion mechanism described earlier, resulting in similar transport of metal from metal surface to the scale surface (Wall 1995).

In molten phase corrosion attack, the presence of a liquid-phase on the metal surface is usually necessary for high corrosion rates, as reactions take place faster in a liquid-phase than in a solid phase. Potassium chloride has a moderately high melting point (776 ^{o}C) with respect to typical heat transfer surface temperatures (450-600 ^{o}C), but can form low-temperature eutectics with various other alkali salts (NaCl, K_2SO_4, Na_2SO_4, etc.) (Nielsen 2000). Because of such low-temperature eutectics, at the usual tube surface temperatures, a local liquid phase could be formed at the deposit-metal interface that triggers a further corrosion mechanism. However, these metal chlorides and eutectic mixtures cannot stay in the liquid state above their respective melting points. They readily evaporate and give rise to corrosion by the gas-phase mechanism. Therefore, the rate of corrosion for the molten phase is non-monotonic with temperature and shows a maximum corrosion rate in a narrow high-temperature range with the rate diminishing on

either side of this peak. This instability of the liquid phase lowers the contribution of molten phase mechanism to the total corrosion at some conditions, but contributes substantially at other conditions.

Along with these mechanisms, investigations show that proper management of chlorine and sulfur content can help prevent corrosion. Figure 5 (Baxter 1998) illustrates the effect of fuel sulfur content on deposit chlorine content.

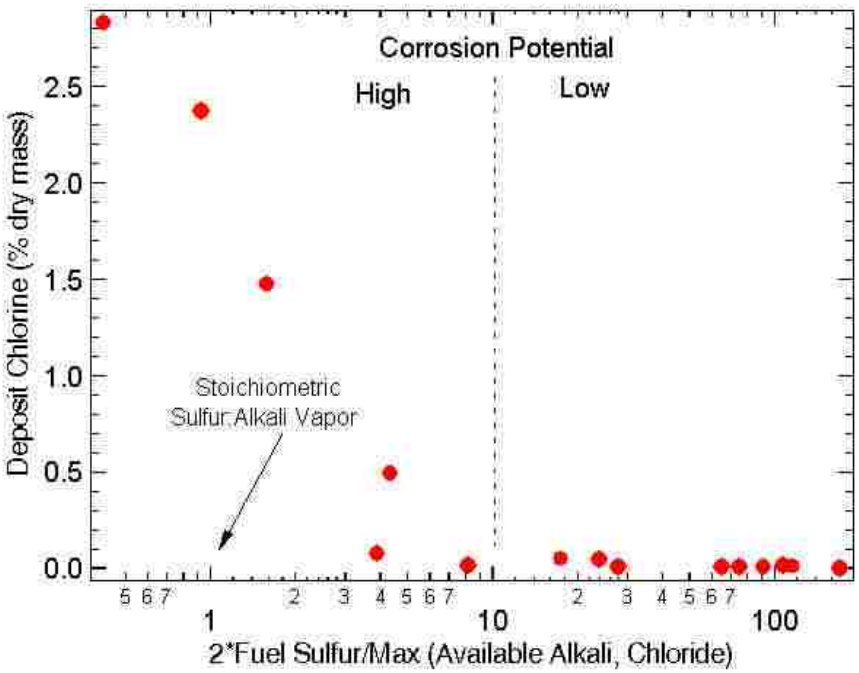

Figure 5: The decrease in deposit bound chlorine with increasing sulfur

The abscissa is twice the ratio of total fuel sulfur to maximum "available" alkali chloride, both on molar bases. Available alkali chloride is the minimum of the amount of fuel chlorine that is not stably associated with another material and the amount of fuel alkali that is not stably existent in another form. For clean biomass fuels (energy crops), the available alkali chlorides essentially equal total alkali chlorides. Fuels containing

different types of additives or soil impurities (most commercial biomass) generally have significant amounts of clay-bound alkali, which basically is the difference between total alkali and available alkali. In theory, at equilibrium, the Cl in the deposit is replaced by sulfur when the ratio of fuel sulfur to maximum available alkali chloride exceeds unity. In practice, the value of this parameter needs to be around 10 to eliminate chlorine and the associated corrosion, due to transport and kinetic limitations in chloride conversion to sulfates (Baxter 1998). These data suggest that the availability of alkali and chlorine affects all these corrosion mechanisms significantly. Lokare (2003) examined the corrosion potential under conditions that are thermodynamically favored but kinetically or otherwise constrained.

Complimentary to experimental data, researchers have developed empirical indices and constants, computer simulations, and predictive models for ash deposition behavior with kinetic, thermodynamic and transport properties. However, empirical procedures used to evaluate slagging or fouling are usually limited to a small range of fuels. These procedures are best only for captive coal situations where variations in inorganic material are small, mechanisms of deposition are consistent, and design and operating variables remain constant. For example, in the case of sintering, more than one mode of sintering may be taking place simultaneously or in series as the deposit develops. Thus, knowledge of the dominant sintering process is necessary to duplicate the operating conditions (Bryers 1996). The fundamental studies, although directed at very specific situations, have made it possible to place limitations on gas or metal temperatures for specific categories of coal. All the research efforts, however, have been directed at establishing the potential for coal to create a fouling, slagging or corrosive

situation. Unlike early stages of large-scale power generation, modern power plants operate on a variable fuel supply, including coals of different rank containing different inorganic composition. To meet these expectations, detailed fuel characterization and the fundamentals of inorganic transformation, composition, and deposition need to be further investigated. Thus, empirical approaches to fireside behavior of impurities in coal frequently fall short of satisfactorily predicting fouling and slagging. Several researchers made attempts to predict ash deposition behavior or some aspects of it. Wang and Harb (1997) used a slagging submodel integrated into a comprehensive combustion code to provide such information. This model included the effects of operating conditions as well as ash chemistry on deposit formation. The integrated model was used to simulate ash deposition in both pilot scale combustor and a utility boiler. Fan et al. (Fan 2001) developed a model to simulate deposit growth under slagging conditions for predicting particle sticking probability and deposit properties.

2.5 Particle impaction and capture

Among five ash deposition mechanisms, inertial impaction and condensation stand out for their significant contribution towards deposition extent and corrosion chemistry. Researchers have focused on inertial impaction for its major contribution to deposit mass accumulation, while condensation has been of special interest for its tendency of enhancing deposition rates as well as corrosion initiation (Baxter 1993; Bryers 1996; Dayton 1996; Jensen 1997; Dayton 1999; Hansen 2000; Nielsen 2000; Nielsen 2000; Coda 2001; Sami 2001; Wessel and Baxter 2003; Lokare 2006). The measure for inertial impaction is combined of two parameters: 1) impaction efficiency (η) which governs particle impaction and is defined as ratio of number of particles impacting

a target to total number of particles flowing through projected target area, 2) capture efficiency which determines particle capture extent and is defined as ratio of number of particles captured by target surface to total number of particles that impacted the target surface. Impaction efficiency is a function of a generalized Stokes number and particle Reynolds number, and Israel and Rosner (Israel 1983) recommended, for an incompressible and inviscid flow, an expression for impaction efficiency as a function of generalized Stokes number with a curve fit of following type:

$$\eta(Stk_{eff}) = \left[1 + b\left(Stk_{eff} - a\right)^{1} - c\left(Stk_{eff} - a\right)^{2} + d\left(Stk_{eff} - a\right)^{3}\right]^{1} \qquad 2.2$$

where, a = 0.125, b = 1.25, c = -0.014, d = 0.0000508

$$Stk_{eff} = \frac{\rho_p d_p^2 V_p}{9\mu_g d_c}\psi \qquad 2.3$$

Here, subscripts p, g, and c stand for particle, gas and cylinder, respectively, while ρ, μ, d and V indicate density, viscosity, diameter and velocity, respectively. Ψ is the non-Stokes drag correction factor. For the above correlating expression for particle impaction on cylinders in cross-flow, Baxter (Baxter 2000) presented two sets of modified coefficients, one for impaction with thermophoresis (a = 0.1425, b = 1.28, c = 0.00215, d = 0.00587) and another for impaction without thermophoresis (a = 0.1238, b = 1.34, c = -0.034, d = 0.0289). Figure 6 shows graphical representation of Baxter's modified correlation for impaction without thermophoresis.

Following impaction, particle capture is a process dependent on physical properties of the impacting particle and target particle or surface. In most cases these physical properties are functions of chemical composition of the particle or surface.

However, it is a very complex situation due to widely varying chemical compositions of particle or surface in solid fuel combustion applications. Therefore, particle capture has been approached as physical phenomenon without any chemistry associated with it. The particle capture process involves numerous collision scenarios:

1. Solid particle on solid surface
2. Solid particle on solid particle
3. Solid particle on particle-laden surface
4. Solid particle on liquid film-covered surface
5. Liquid droplet on solid surface, etc.

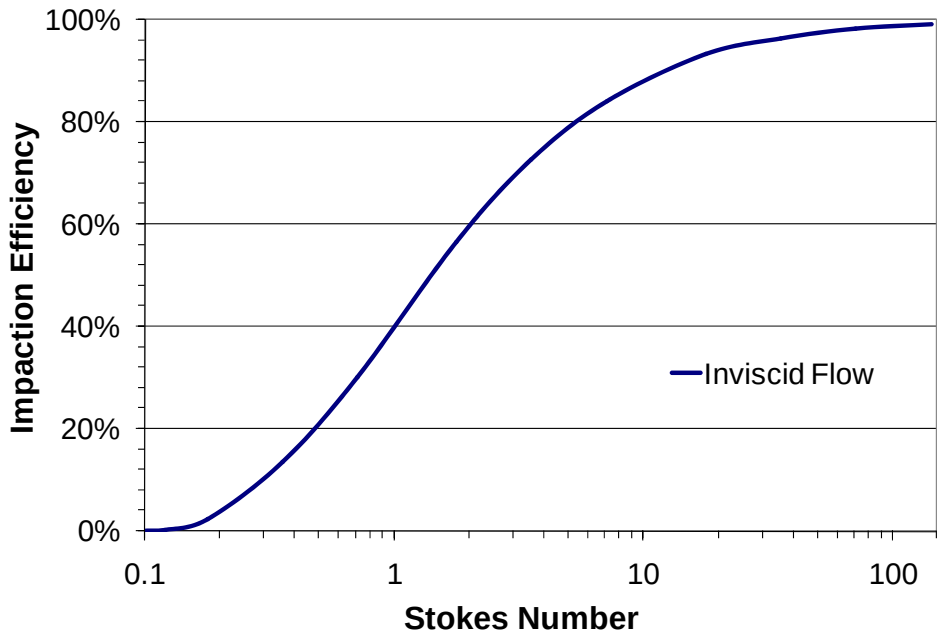

Figure 6: Impaction efficiency variation with Stokes number

Wall et al (Wall 1989; Wall 1990) described an approach based on kinetic energy loss for particles impacting surfaces. With their experimental work, they showed that, at

low particle velocities (<20 m/s), the coefficient of restitution (the ratio of rebound to impact velocity) was sensitive to target material, decreasing with impact velocity; while for higher particle velocities, the coefficient of restitution was insensitive to the target material. It was also confirmed that plastic deformation was a significant component of kinetic energy loss at all impact velocities investigated in the experiments. A measure of kinetic energy loss responsible for particle capture, termed as critical velocity of a particle, indicates an impact velocity below which the particle will always be captured. This has been an important parameter in several investigations regarding particle capture. Several researchers (Andres 1995; Konstandopoulos 1997; Thornton 1998) have presented such critical velocity expression as a function of particle properties (diameter, mass, yield stress) and coefficient of restitution. However, this expression also involved a parameter *w*, Dupre surface energy, which along with coefficient of restitution, is unknown a priori. Though several of the above researchers have gathered data on some specific particle-substrate combinations, it does not represent a general result that could be applied to most combustion applications. Thus, for any particular particle/substrate set-up, experiments are necessary to accurately estimate the coefficient of restitution and other dependent parameters. As a simplified approach, Lee and Lockwood (Lee 1999) used the Urbain viscosity model in their ash deposition model to estimate particle viscosity, arbitrarily chosen to be 10^5, and compared it with a 'critical velocity' to calculate sticking probability. According to their set up, for particle viscosities less than the critical value, the sticking probability was one, while the viscosities higher than the critical value, sticking probability was the ratio of critical viscosity to the actual viscosity. Though useful in some cases, this simplified approach implements an inflexible criterion

(i.e. based only on particle viscosity and not particle dynamics), which keeps it from being able to be applied in every location of furnace facilities.

In the particle capture process, the next level of detail comes in the form of oblique impacts and particle collisions with surfaces layered with either liquid film or fine particulate. Brach and Dunn (Brach 1992; Brach 1998) presented a simple algebraic, rigid body impact models using coefficients of restitution and coefficient of friction. Their analysis of oblique collisions considers effects of rolling, sliding and rotation and revealed that there were no observable significant differences in restitution coefficients for normal and oblique collisions. This could be the basis for several researchers continuing impaction investigations with the assumption of normal collision. For particle impactions on a surface with a liquid layer, Davis et al (Davis 2002) discussed the influence of viscous dissipation in the thin fluid layer on particle sticking probabilities for low impact velocities. They found that above a critical impact velocity, the lubrication forces in the thin layer cause elastic deformation and rebound of the spherical particles. Such interesting results are of great value for investigating ash deposition process in furnace section or secondary superheater sections of a boiler where temperatures are high enough to leave surfaces with a thin molten layer of ash. Kantak and Davis (Kantak 2004) followed this investigation and extended it for several types of particle materials and incorporated angular impacts in to their earlier research work. While this work reiterated some of their previous results, it also showed that critical approach velocity for rebound increases with increasing deviation of impact angle from a normal collision. Thus, in general, particle impaction on a surface with a liquid layer proceeds with higher capture efficiency as opposed to the impaction on rigid surface for similar particle sizes

and velocities. Similar trends were seen by van Beek et al (van Beek 2006) in their investigation of rebound characteristics for 50-micron particles impacting a powdery deposit. A fine particulate layer on a surface, analogous to a liquid film in earlier case, is shown to dissipate the kinetic energy of an impacting particle through numerous inelastic collisions between bed particles. These two processes are very important since, in the early phases of ash deposition, large particle deposition is preceded by vapor condensation and fine particle deposition through thermophoresis and/or eddy impaction on superheater surfaces, thus creating higher potential for subsequent larger ash particle deposition.

2.6 Original contribution

Current understanding of the deposition issues in coal and biomass combustion in various operating conditions comes from limited experimental data under specific conditions. The processes that lead to the most recent interest in these fuels involve various aspects of sustainable energy development (renewable fuels, mercury emissions, CO_2 sequestration, etc.). This research work focuses on collecting experimental data on ash deposition potential on selected coal and biomass fuels under well-characterized conditions and supplementing these with fundamental investigations of particle deposition behavior on non-industrial conditions. This combination of data helps define accurate and relevant models useful for predicting and understanding ash deposition.

Experimental data will be obtained to validate the predictive models for individual deposition mechanisms, specifically impaction and condensation. Existing ash deposition models predict inertial impaction based on potential flow fields. However, simulations using real flow characteristics may give more accurate description of the

impaction process. Therefore, the experimental data along with individual-mechanism deposition models (impaction and capture) will strengthen the existing overall ash deposition model.

3 Objectives

The objectives of this research are (a) to collect quantitative and qualitative ash deposition and corrosion initiation data for a variety of fuels under a variety of commercially significant conditions and under idealized conditions in developing fundamental correlations, and (b) to develop models that predict the rates and mechanisms of deposition validated by the data. The fuels selected for investigation focus on traditional coal and biomass fuels and on fuels considered for developing new combustion processes. Fundamental experimental work applicable to combustion, gasification, oxyfuel firing, and other reaction conditions provide the basis for most of this work. Specifically, this investigation will include deposition during: 1) Combustion of biomass with fuel additives, 2) Co-firing of coal with straw, 3) Combustion of coal under thermally treated conditions, and 4) Combustion of coal in oxyfuel conditions.

Table 1 shows the summary of ash deposition tests arranged for investigation of each of the above mentioned combustion scenario.

Table 1: Fuel matrix

Topic	No of fuels	No of Conditions	Repeats	Total Tests
Additives effect on biomass ash deposition	12	12 pure fuels	2	24
Coal biomass Co-firing	3	3 pure fuels + 4 blends	2	14
Effect of thermal treatment	3	3 pure fuels x 2 conditions	2	12
Oxyfuel Combustion	2	2 pure fuel x 4 conditions	2	16
Total				66

The core experimental contribution of this work consists of quantitative and qualitative data on the following deposition mechanisms: 1) Inertial impaction, 2) Salt condensation, and 3) Eddy impaction. The following models will predict the data collected from the above fuels and mechanisms to validate the rates and mechanistic details.

1. Fluent simulation of ash particle inertial impaction in real flow and its comparison to impaction using potential flow characteristics.
2. A Visual C++ computer code that predicts capture/rebound potential of impacting ash particles on 2 different surface types (smooth and rigid, smooth with fine particulate layer).
3. Fluent simulation of fine (submicron) ash particle impaction due to turbulent eddies.
4. A systematic prediction of ash accumulation rate based on all of the above mechanisms.

The chemical reaction kinetics in ash deposits, while important, is not included in the scope of this work. All work will be based on laboratory samples and not field samples.

4 Equipment and Method

4.1 Multifuel flow reactor

The recently rebuilt multifuel flow reactor (MFR) provides the experimental capacity to investigate the overall ash deposition rate investigation (see Figure 7). The MFR consists of eight refractory-lined, circular metal sections connected co-axially. All sections except one (Section 3) are 27.5 cm tall and have an inside diameter of 12.7 cm and outside diameter of 36.5 cm. The reactor sections are fitted with flanges and gaskets so that they could be bolted together to reduce leakage of air into the reactor. Section 1 has two windows for visual flame inspection. Section 7 (see Figure 8(a)) contains a portal for inserting the sampling probe. Section 3 (see Figure 8(b)) is 14.5 cm tall and has four opposed methane injectors to facilitate preheating of the reactor. All sections except Section 3 contain multiple thermocouple access ports. Through these ports, thermocouples placed flush with the inside refractory measure wall temperature profiles along the reactor. Thermocouple positions are adjustable for measurements of gas as well as wall temperatures.

A choked-flow orifice measures air and natural gas flow. Natural gas flow rates were calibrated with a certified natural gas flow meter (Courtesy Questar Gas, Provo, UT). Pure oxygen flow is calibrated against a calibrated air flow meter and corrected for molecular weight.

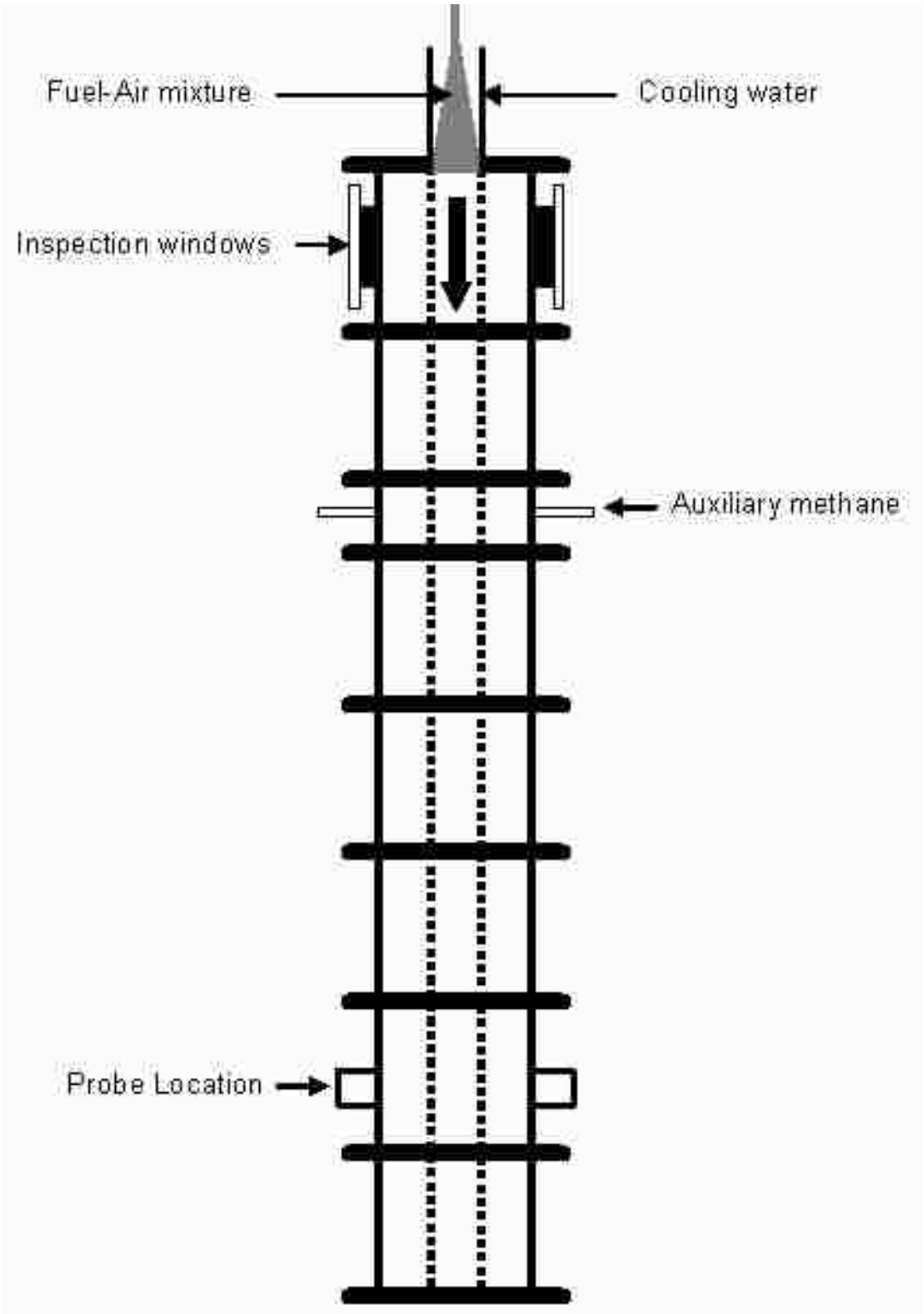

Figure 7: Multifuel flow reactor (MFR)

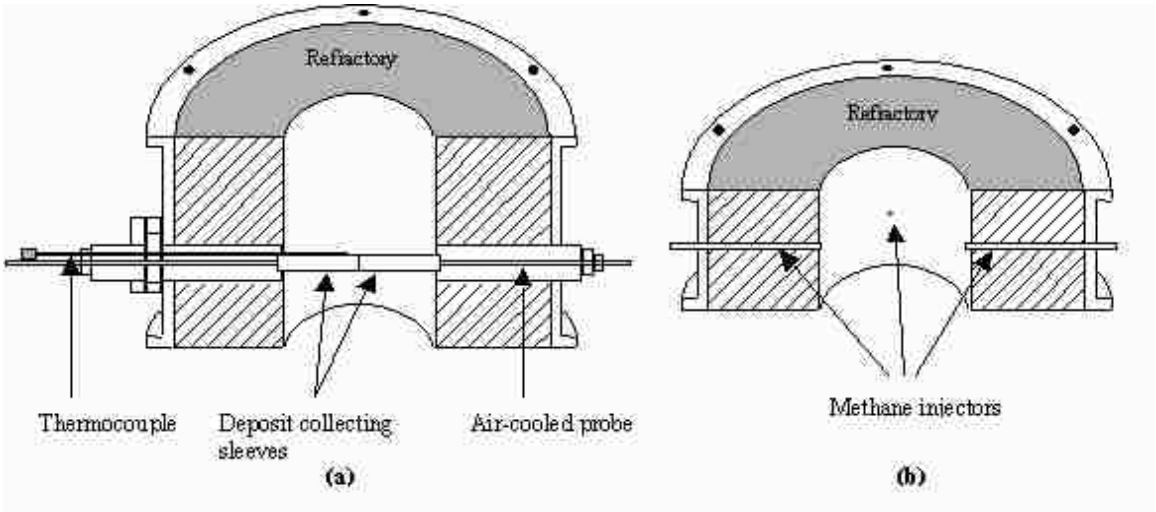

Figure 8: Special sections: (a) Sampling section, (b) Auxiliary methane section

A single-augur Acrison Gravimetric Feeder (Acrison Model 406-BDFM) feeds solid fuel to the reactor at a nearly constant rate. An Acrison MD-II feedback controller monitors and controls the solid fuel feed rate. The solid fuel feeds into a funnel (see Figure 9) made of aluminum, permanently attached to the feeder. Seals on the funnel prevent any unmetered air from entering the reactor. After passing through this funnel, a Fox Valve eductor (1/2" 300-SCE-CS) entrains the fuel in the primary air. A diverging cone section transports the biomass/gas mixture to the top of the reactor. A single flow-straightener breaks up aggregated fuel particles prior to injection into the burner.

An in-line pressure adjustment valve between the top of the aluminum cone and the bypassed primary airline provides consistent feed rates. The pressure adjustment valve reduces pressure fluctuations and allows the solid fuel to fall freely through the tube below the aluminum cone. The valve balances the pressure inside the hopper and pressure inside the aluminum cone, reducing interference of air flow with solid fuel feeding.

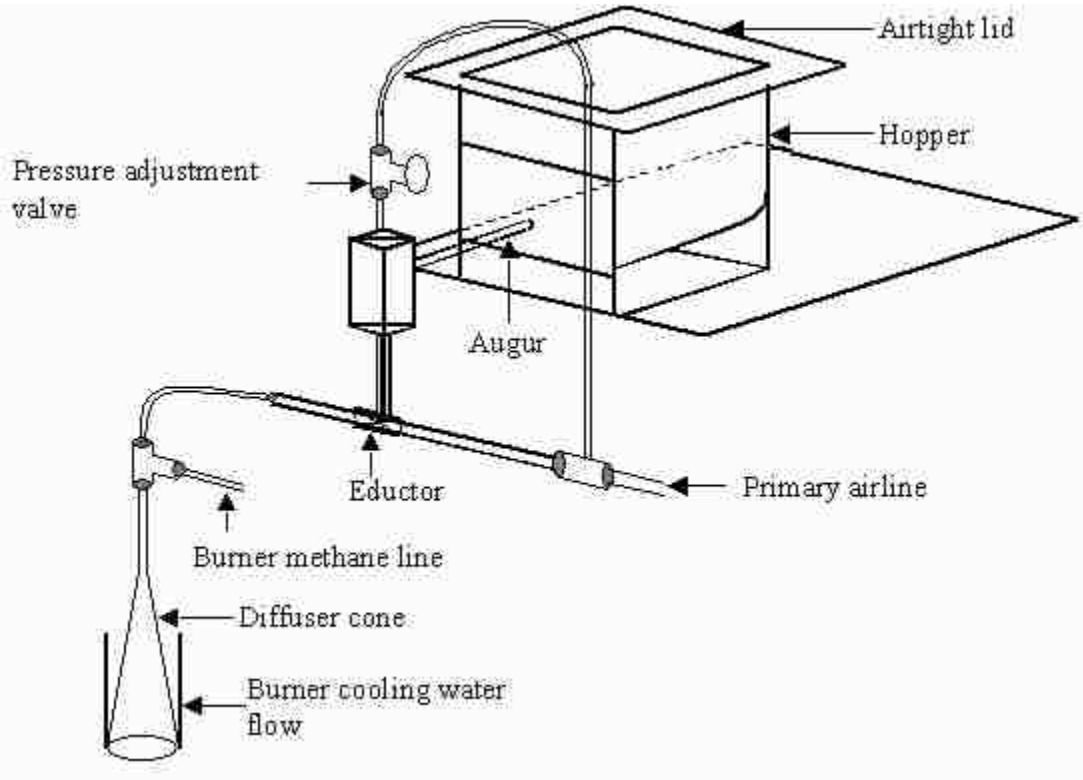

Figure 9: Feeder assembly with pressure adjustment

The feeding system allows a fuel-air mixture to enter the combustion zone through a water-cooled brass fixture that acts as a burner, flow straightener and flame holder (see Figure 10). The honeycomb fixture resembles a similar system previously used for coal (Adair 1998) except that the hole size is larger (5.8 mm diameter) to accommodate the wide range of solid fuel particle sizes. The design supports a premixed flame for long periods of time (essentially indefinitely) at flame temperatures. Burner cooling helps prevent upstream flame propagation, commonly called “flash-back,” and consists of water passing through horizontal passages drilled across the burner between

the rows of axial/vertical holes. An O-ring between the burner and the diffusion cone prevents premixed fuel from bypassing the burner.

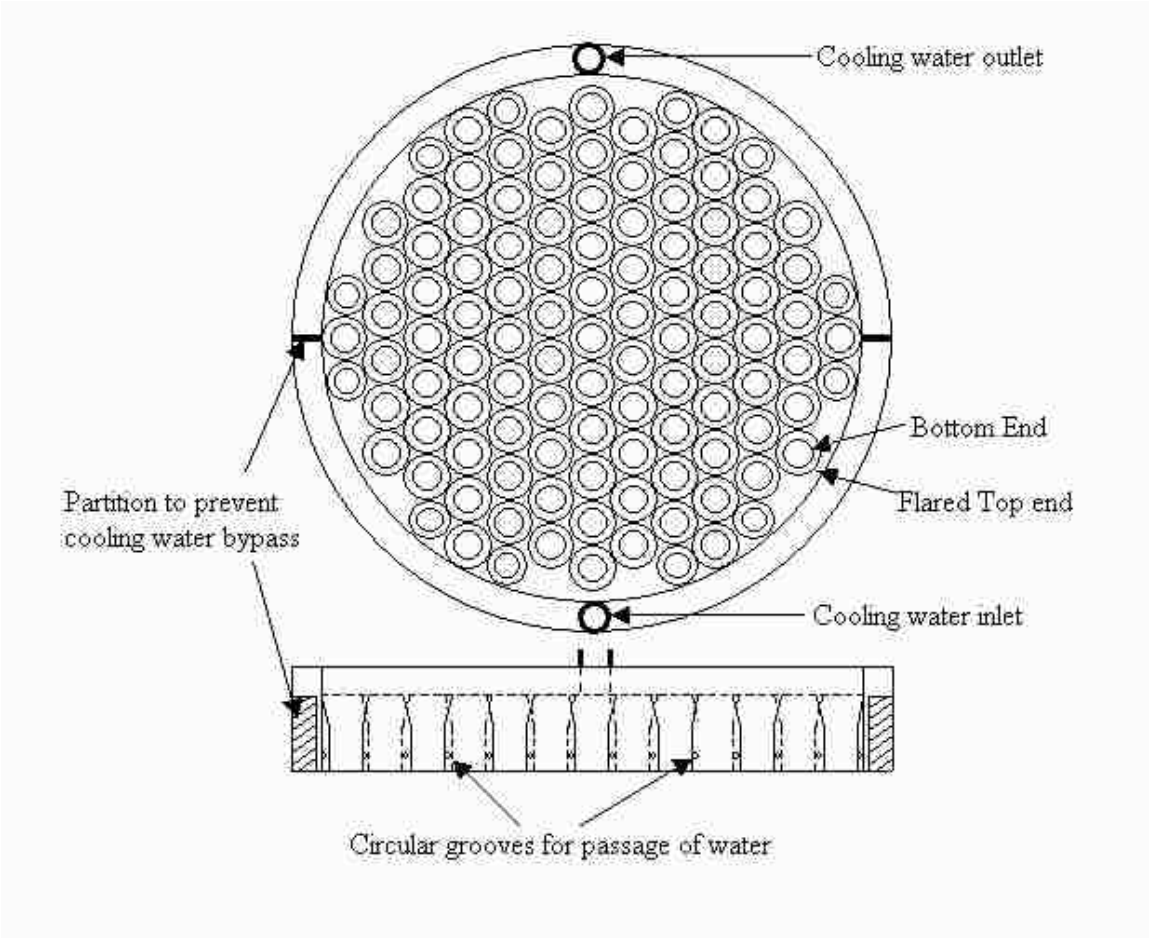

Figure 10: Water-cooled Honeycomb Burner design

The efficient burner assembly creates a well-mixed combustion environment for coal/biomass to produce ash particles that are collected by specially designed collection probes. First, a temperature-regulated probe placed in cross flow relative to the gases and particles and scaled with respect to Stokes number collects deposits that reveal both rate and mechanistic information (see Figure 11). A 0.127 cm (1/2 inch) diameter by 12 cm long sleeve collects ash deposits. The sleeve consists of two 6 cm long sections. The two

sleeve sections connect by male and female ends to ensure thermal contact and minimize axial temperature gradients. A groove milled into the first, permanently mounted sleeve section contains a thermocouple that measures probe surface temperature. The second sleeve section detaches from the probe. Its weight change determines quantitative deposition rates, after which it is cast in epoxy and used in sacrificial scanning-electron-microscope-based deposit chemistry analyses. Ash deposited on the fixed half of the sleeve provides a gravimetric and chemical analysis sample. The sleeve mounts on a 0.953 mm diameter air-cooled probe that traverses the entire reactor diameter. Total length from the burner to the probe is variable up to slightly over 2 m, but typically measures 1.93 m.

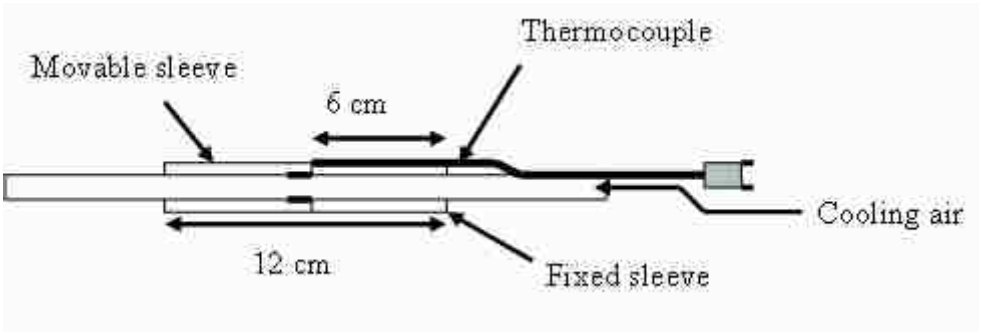

Figure 11: Ash deposit collection probe

A second actively cooled, rapid quench, isokinetic probe collects fly ash from the MFR (see Figure 12, not to scale). In an isokinetic probe, first, the sample inlet is designed such that the acute angle between innermost tube and slanted ring connecting innermost tube and outermost tube measures 30 degrees or less, and second, the vacuum pump at probe outlet is adjusted such that the gas flux through the probe inlet remains same as the gas flux through the reactor. Sampling occurs near the location of deposit accumulation.

Fly ash size distributions and other physical and chemical properties come from these samples.

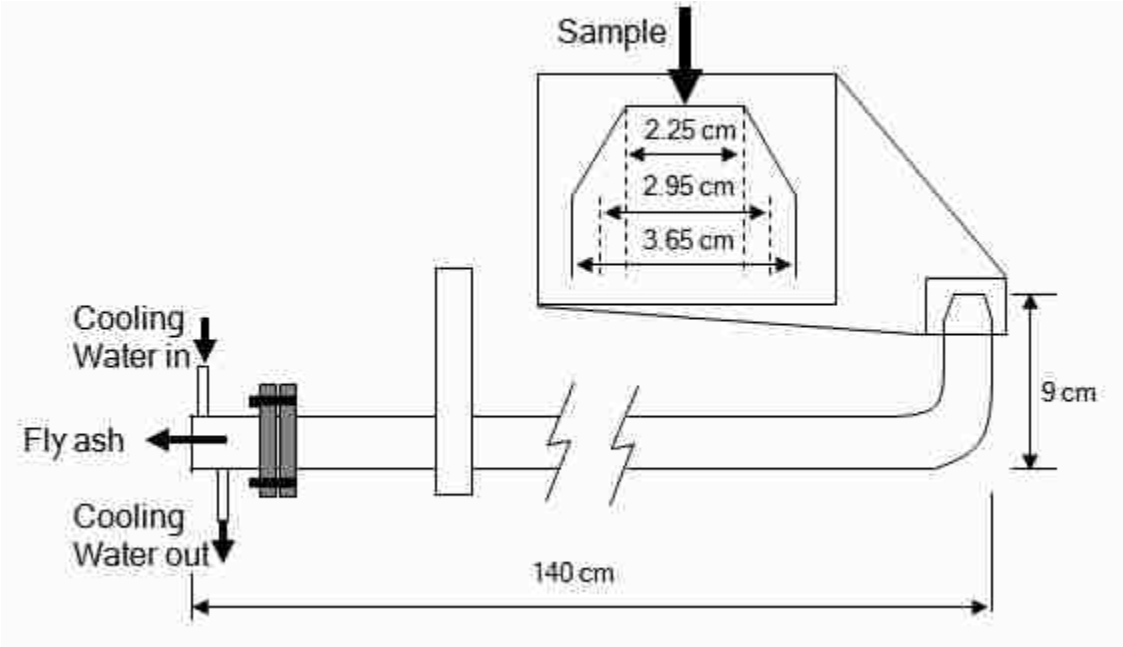

Figure 12: Fly ash collection probe

4.2 Entrained flow reactor

The schematic of the entrained-flow reactor designed and built previously by Hong Lu (Lu 2006) appears in Figure 13. The experimental setup consists of six parts: a particle feeding system, a secondary gas preheater, an entrained-flow reactor body, a sample collection and separation system, an imaging system, and a temperature control system. A syringe feeder ('Fuel Feeder' in Figure 13) regulates fuel feed rate, with fuel particles entering the reactor through the feed probe. The preheater heats secondary gas to 1400 K as it flows into the top of the reactor. The fuel particles mix with preheated secondary air to undergo combustion, producing fine ash particles. The distance between

the feed probe and the collection probe and the entraining air flow fix particle residence time in the reactor. Separate valves and choked-flow orifices control and meter primary gas, secondary gas, and quench gas flow rates. The details of the preheater and feeding systems are described in Hong Lu's PhD dissertation (Lu 2006).

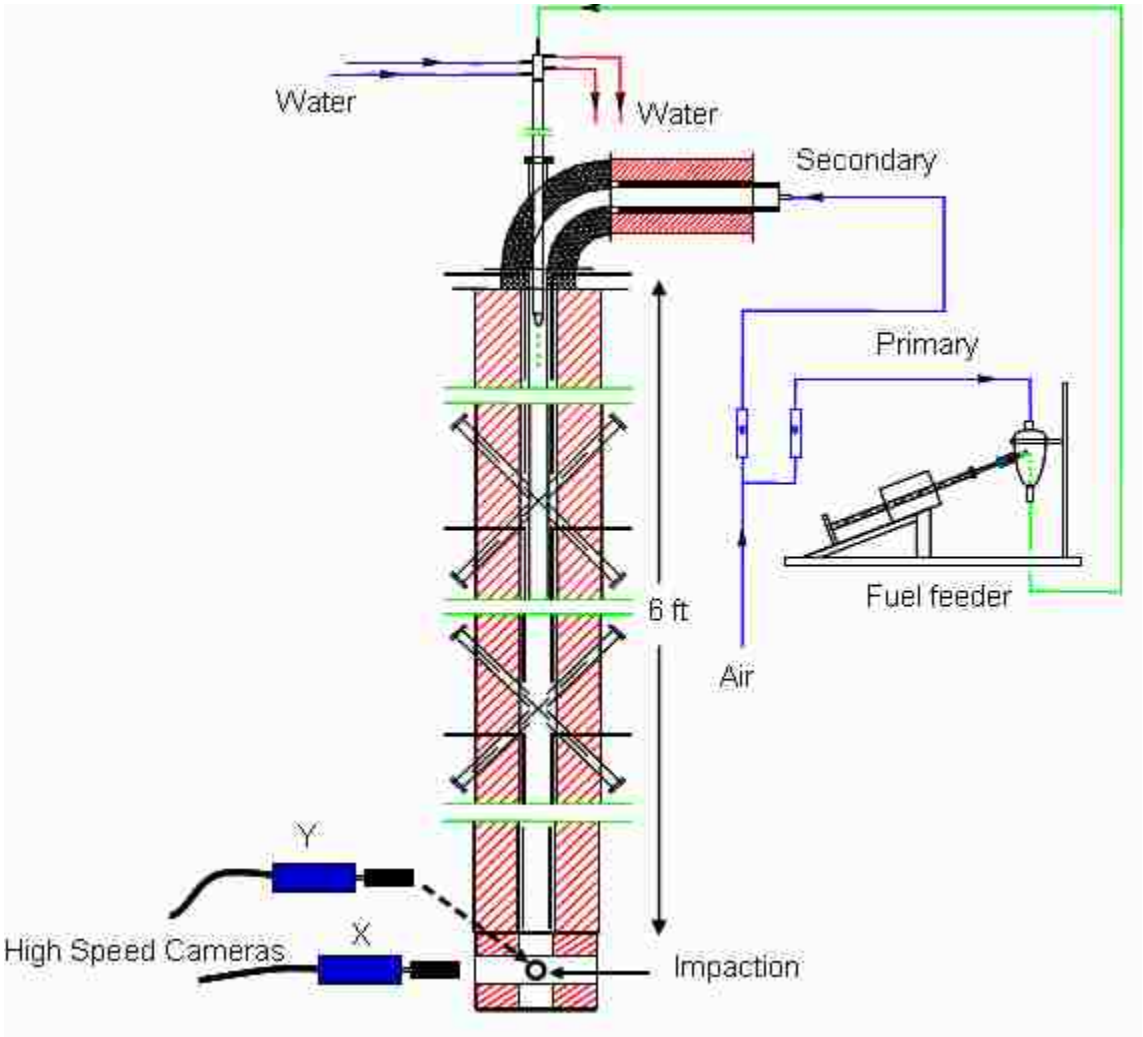

Figure 13: Entrained Flow Reactor

Recrystallized SiC tubes with 60 mm OD and 50 mm ID line the reactor main body (see Figure 14). The reactor is 1.8 m long, providing a residence time of up to 3

seconds. The reactor insulation includes one layer of alumina fiber board and two layers of high-temperature blankets. Molybdenum disilicide Kanthal Super heating elements are placed between the reactor tube and the inner alumina fiber board; which control the reactor temperature. The design calls for a maximum outer surface temperature of 50 ^{o}C. The entrained-flow reactor attains wall temperatures up to 1600 K and a particle heating rate of 10^{3}~10^{4} K/s. SCR temperature controllers in each of four sections of the reactor control the wall temperature profile.

Figure 14: Windows section showing inner reactor tube with optical access; before applying insulation material

Windows at three levels along the reactor body provide optical access, allowing three orthogonal measurements of particle surface temperature and particle shape with CCD/CMOS cameras. These windows divide the reactor into four sections. Each of the windows provides optical access for image acquisition from three orthogonal directions, as shown in Figure 14. Quartz window glass seals the outside end of each view port

supported by a SiC plate. Each window section includes six view tubes and a short collar tube. The imaging system includes two cameras, two image acquisition boards, camera control and image processing software, and a high-performance computer. The imaging system can record up to two-minute videos with full resolution (1036x1024), and longer record time can be obtained at reduced resolution. The camera uses a SONY ICX285AQ CCD sensor with micro lenses, which is more sensitive in the near infrared (NIR) range than a traditional CCD sensor. The electrical shutter speed is as short as 62 μs. Detailed components specifications of the imaging system appear in Table 2.

Table 2: Components and specifications of imaging system.

Camera	SVS-285CSL, 10 bit, shutter speed, frame rate
CCD sensor	Sony ICX285AQ, Cell size 6.45x6.45 μm, (1036x1024)
Lens model	Computar MLH-10X
Image acquisition board	Epix Inc. PIXCI D2X
Camera control software	XCAP2.0
Computer configuration	XEON CPU 3.06 G Hz, 3.5G RAM

The two cameras are pre-focused on the center of reactor through the window ports in the bottom section, at 90^{o} with each other. The recorded videos undergo particle velocity analysis (explained later) and temperature analysis (also explained later) to yield a particle impact and rebound velocity and impaction surface temperature. The reactor heating system consists of an electrically controlled heater assembly. The reactor wall temperatures in each of four sections behave independently. Each section has 4 U-shaped 90^{o}-bent Kanthal Super heating elements and the power output can be adjusted by the transformer and SCR controllers to regulate temperature. Two three-phase SCR controllers and two three-phase transformers control the 12 heating elements in the top

three sections of the reactor according to the set points using three fuzzy logic controllers. Each of the 6 heating elements is star-connected with the three-phase transformer. The bottom section is controlled by a single-phase SCR controller a single-phase transformer and an additional fuzzy logic controller with the 4 heating elements connected in series. Detailed specifications of each component of the temperature control system are listed in Table 3.

Table 3: Components and specifications of reactor heating system

Temperature controller	FuzyPro 1/16 DIN
SCR controller	Halmar Electronics Inc., 3P-4860-CL-D Single phase: AVATAR B2P -24-60, SCR71Z-230
Transformer	Matra Electric Inc. Model 90165346K, 480-70Y/40.4 Single phase: Olsun Electrics Corp. H-115 208-50/60

4.3 Fuel selection and preparation

This research work consists of several fuel suites associated with various combustion conditions: (1) Oxyfuel combustion, (2) Combustion of thermally pretreated coal, (3) Cofiring biomass with coal, and (4) Combustion of biomass with fuel additives.

4.3.1 Oxyfuel combustion

Oxyfuel combustion tests were performed with three coals; Illinois #6 and Powder River Basin (Caballo) (see Table 4). Traditional oxidizer, air, is replaced by a mixture of pure oxygen (99.5%) in Argon and pure CO_2 (99.99%) in Argon. Each of these coals is fired with air for reference test and then under oxyfuel conditions for three different O_2-CO_2 ratios (25-75%, 30-70%, and 35-75% by volume). All tests are repeated once. Thus the test matrix for the oxyfuel project includes 24 tests.

Table 4: Fuel and Ash Composition for Oxyfuel Combustion Tests

Fuel (maf)	Illinois #6	PRB (Caballo)
C	81.88	68.84
H	4.37	5.77
N	1.27	1.11
S	4.64	0.27
O	7.84	24.01
Total	100	100
Ash % (mf)	9.31	7.87
Moisture % (ar)	14.22	12.93
HV, Btu/lb (maf)	14226	12511
SiO_2	49.81	30.02
Al_2O_3	17.65	15.61
Fe_2O_3	18.99	5.88
CaO	5.55	21.33
MgO	1.22	4
Na_2O	1.89	4.61
K_2O	2.18	0.81
TiO_2	0.92	1.22
MnO_2	0.05	0.05
P_2O_5	0.19	0.91
SrO	0.06	0.42
BaO	0.08	0.56
SO_3	1.41	14.58
Total	100	100

4.3.2 Coal combustion after mercury pretreatment

The fuel suite for this part of the project includes two Powder River Basin coals (Caballo and Corederro) and Beulah Lignite (see

Table **5**). These coals are thermally pretreated for removing mercury by evaporation. Corederro is treated in lab at BYU while Caballo and Lignite were treated outside BYU by Alliant Energy Group. Each coal undergoes combustion test in untreated

as well as treated form. Each combustion test is repeated once creating a test matrix of 12 tests.

Table 5: Fuel and Ash Composition of PRB and Lignite Coals

Fuel (maf)	Caballo		Corederro		Lignite	
	Untreated	Treated	Untreated	Treated	Untreated	Treated
C	68.84	72.54	71.45	73.26	69.22	70.64
H	5.77	5.22	6.02	4.82	6.02	4.96
N	1.11	1.15	1.1	1.15	0.97	1.04
S	0.27	0.42	0.17	0.18	1.93	1.8
O	24.01	20.68	21.26	20.59	21.87	21.56
Total	100	100	100	100	100	100
Ash % (mf)	7.87	6.91	7.12	7.85	12.98	11.83
Moist. % (ar)	12.93	3.82	13.64	3.42	14.05	3.97
HV, MJ/kg (maf)	29.04	27.31	29.89	28.14	28.28	25.36
SiO_2	30.02	30.02	28.7	28.7	18.4	18.4
Al_2O_3	15.61	15.61	15.5	15.5	10.22	10.22
Fe_2O_3	5.88	5.88	10.2	10.2	8	8
CaO	21.33	21.33	15.1	15.1	24.72	24.72
MgO	4	4	3.6	3.6	7.48	7.48
Na_2O	4.61	4.61	1.5	1.5	7.76	7.76
K_2O	0.81	0.81	0.8	0.8	0.94	0.94
TiO_2	1.22	1.22	1.2	1.2	0.48	0.48
MnO_2	0.05	0.05	NA	NA	0.14	0.14
P_2O_5	0.91	0.91	1.2	1.2	0.48	0.48
SrO	0.42	0.42	NA	NA	1.12	1.12
BaO	0.56	0.56	NA	NA	0.84	0.84
SO_3	14.58	14.58	22	22	17.55	17.55
Total	100	100	100	100	100	100

4.3.3 Coal biomass co-firing

The fuel suite for co-firing tests consists of two coals, Illinois #6 and Blind Canyon, and a biomass fuel, straw (see Table 6). The fuels are chosen according to the

extent of their usage in industrial boilers in the United States of America. Each fuel is fired alone for reference tests and then each coal is mixed in two ratios (70-30% and 30-70% by mass) with straw, and all tests are repeated once. Thus the test matrix has total of 14 tests.

Table 6: Fuel analysis for co-firing tests

Fuel (maf)	**Straw**	**Illinois #6**	**Blind Canyon**
C	44.39	81.88	80.69
H	5.71	4.37	5.76
N	0.91	1.27	1.57
S	0.12	4.64	0.37
O	48.87	7.84	15.77
Total	100	100	100
Ash % (mf)	8.14	9.31	4.71
Moisture % (ar)	6.76	14.22	4.63
HV, Btu/lb (maf)	6868	14226	14613
SiO_2	57.35	49.81	45.9
Al_2O_3	1.46	17.65	16.6
Fe_2O_3	1.35	18.99	10
CaO	5.1	5.55	9.9
MgO	2.16	1.22	1.5
Na_2O	2.75	1.89	3.6
K_2O	24.11	2.18	1.2
TiO_2	0.11	0.92	1.2
MnO_2	NA	0.05	NA
P_2O_5	2.58	0.19	0.3
SrO	NA	0.06	NA
BaO	NA	0.08	NA
SO_3	3.04	1.41	9.8
Total	100	100	100

4.3.4 Combustion of biomass with fuel additives

This fuel suite consists of 12 biomass fuels prepared by mixing different biomass fuels and various chemical additives (see Table 7). These fuels were processed and prepared in final form by one of our industrial partners, Techwise (now Dong Energy), Denmark. The test matrix consists of 24 tests (2 x 12 fuels).

Table 7: Fuel analysis of biomass with fuel additives

Fuel(maf)	R1	R2	R3	R4	R5	R6	R7	R8	R9	R10	R11	R12
C	43.03	43.97	44.98	46.62	43.90	46.15	45.02	45.99	44.98	43.06	39.50	42.12
H	5.75	5.62	5.85	5.88	5.71	5.86	5.88	5.90	5.63	5.68	5.18	5.23
N	0.81	0.52	0.72	0.54	0.66	0.65	1.39	1.86	2.24	2.12	1.37	2.32
S	0.12	0.41	0.15	0.09	0.08	0.08	0.08	0.14	0.15	0.13	0.10	0.14
O	50.29	49.48	48.29	46.87	49.65	47.26	47.62	46.11	47.00	49.01	53.84	50.19
Total	100	100	100	100	100	100	100	100	100	100	100	100
Ash(mf)	8.19	7.89	8.61	7.50	7.66	7.69	8.90	9.68	10.71	11.54	9.36	9.17
Moist(ar)	6.57	6.88	6.25	6.20	6.38	6.02	5.78	6.18	6.66	6.30	8.32	9.98
HV(maf) MJ/kg	15.61	15.21	15.21	14.51	14.41	15.61	15.81	16.01	14.91	14.81	15.91	14.81
SiO_2	45.5	50.7	39.4	26.6	22.5	20.5	19	18	17.7	22.5	24	23.2
Al_2O_3	8.1	7.9	0.5	0.3	26	0.3	1.2	1.2	1.3	1.4	1.6	1.7
Fe_2O_3	1	0.9	0.8	0.6	0.5	0.4	1.4	1.4	1.5	1.7	1.8	2
CaO	8	7.3	20.6	32	4.5	29.2	27.7	27	25.3	25	24.9	23
MgO	1.6	1.5	1.4	1	0.9	0.8	2.2	2.7	2.8	2.5	2.8	3.6
Na_2O	0.3	0.3	0.7	0.2	0.8	0.8	1.5	1.4	1.4	1.6	1.6	1.3
K_2O	19.1	17.5	17.8	11.4	11.2	10.5	12	13.7	16.4	13.5	14.2	20
SO_3	3.5	3.2	3.3	2.1	2.1	2	3.1	3.6	3.9	3.6	3.7	4.8
P_2O_5	2.8	2.5	2.4	1.7	1.4	1.3	6.4	6.6	6.7	7.6	8.1	8.8
CO_2, H_2O	4.9	2.8	0	21.1	16.7	19.8	14.6	14	13.2	11.5	10.5	9.3

Table 7 continued

Fuel(maf)	R1	R2	R3	R4	R5	R6	R7	R8	R9	R10	R11	R12
Cl	4.9	4.4	4.4	2.9	2.6	2.4	1.7	1.6	1.6	1.9	2	2
Other	0.3	1.2	8.7	0.2	10.9	12	9.1	8.7	8.2	7.2	4.8	0.4
Total	100	100	100	100	100	100	100	100	100	100	100	100

4.4 Experimental procedure

This section presents the procedures followed for reactor operation and sample collection and preparation. The reactor operation includes a description of start up, warm up, and the steps necessary to achieve a stable flame after switching to solid fuel. Following this will be a detailed discussion of the deposit collection and sample preparation procedures.

4.4.1 Multifuel flow reactor

Fuel feed rates vary with fuel type and other conditions but commonly are about 10 kW based on the higher heating value of the solid fuels. The solid fuel feed rate varies from about 0.4 to 1.5 kg/hr (0.9-3.3 lb/hr), depending on fuel density.

The reactor is always preheated with natural gas. Typically, the reactor wall temperatures rise to about 1000 ^{o}C over a period of about 2 hours. Natural gas flows through both the burner and four injection locations in Section 3 during preheating, but combustion air flows only through the burner. Following an initial heating period, the solid fuel feeder replaces the natural gas feed to the injectors in Section 3. The deposit sample probe is inserted after the solid fuel feeding rate and reactor temperature profiles stabilize, typically after 60 minutes. Some solid fuels, including many biomass fuels, require continued use of natural gas and/or oxygen enrichment in the burner to provide a self-supporting flame for long-term tests. The hopper on the solid fuel feeder is filled to

80% of its total capacity prior to performing an experimental test. After filling the hopper and before switching to solid fuel combustion, the density of the fuel in the hopper is entered in the controller and controller is set to the gravimetric mode. Based on the amount of fuel in the hopper, the full range of augur speeds is used to determine the intermediate and maximum feed rates. The fuel feed rate is set, using a feeder controller panel, according to the specific stoichiometric requirements. The typical feed rates are between 0.5 – 1.5 kg/hr. However, the feed rate range varies from coal to biomass fuels due to difference in stoichiometry of coal and biomass combustion.

After switching to solid fuel, the fuel flow rates are adjusted to achieve 3.5-4.5 % oxygen (dry basis) in the exhaust, which is measured by a HORIBA PG-250 gas analyzer. Table 8 gives the information regarding analysis method of each of the species measured in this investigation, as well as the range and the accuracy for each analyzer. Table 9 shows the interfering species for the Horiba analyzer. The natural gas feed is not completely turned off after switching over to solid fuel combustion. The relatively low heating values of many fuels, particularly biofuels, provide insufficient feedback to the burner to maintain a self-supporting, steady flame. This is mainly due to high moisture content of the biofuels. Therefore, the biofuel flame is augmented by sufficient natural gas for a stationary flame that is attached to the burner. As much as 50% of the total heat is supplied by natural gas. Natural gas supplemental feeding requirement is significantly less for coal than for biofuels. It is important to have an attached flame to produce similar particle residence times and temperature histories. The reactor is slightly pressurized to keep unmetered oxygen from leaking into the reactor. The digital fan speed controller and the differential pressure gauge (indicates difference between the reactor pressure and

atmospheric pressure) control the reactor pressure accurately. The reactor reaches steady-state temperatures throughout prior to starting the deposition test, which generally requires 1 hour for each deposition test and sample collection. For multiple deposition tests, time required is directly proportional to number of tests, without any unexpected disturbances.

Table 8: Species measurement methods

Measurement	Technique	Range	Accuracy
CO2 (vol%)	ND-IR	0-18	+/- 0.5%
CO (ppm)	ND-IR	0-5000	+/- 0.5%
O2 (vol%)	galvanic cell	0-25	+/- 0.5%
NO (ppm)	Chemiluminescence	0-500	+/- 0.5%

Table 9: Horiba gas interference table (Horiba Inc.)

Measured Component	Interference Gas					
	H_2O (5°C Saturation)	NO (1000 ppm)	C_3H_8 (1000 ppm)	SO_2 (1000 ppm)	CO_2 (20%)	CO (5000 ppm)
NO	+/- 2%FS	-	+/- 2%FS	+/- 2%FS	+/- 2%FS	+/- 2%FS
CO (<200 ppm)	+/-2%FS	+/-2%FS	+/-2%FS	+/-2%FS	+/-2%FS	-
CO (>200 ppm)	+/-1%FS	+/-1%FS	+/-1%FS	+/-1%FS	+/-1%FS	-
CO_2	+/-2%FS	+/-2%FS	+/-2%FS	+/-2%FS	-	+/-2%FS
O_2	+/-2%FS	+/-2%FS	+/-2%FS	+/-2%FS	+/-2%FS	+/-2%FS

4.4.2 Sample collection procedure

Biofuel samples from both pure fuels and fuel blends in the MFR help determine the effect of fuel mixing on deposition and corrosion initiation. The procedure for deposit

collection involves probe insertion and positioning, deposit growth, and deposit extraction.

When the reactor temperature reaches steady state under solid-fuel-fired conditions, the deposit probe cooling air is turned on and the probe is inserted into the reactor through the sample port in the sampling section. Once in place, the machined 2 inch (10.48 cm) pipe cap is screwed into the sample port, sealing the gap between the opening in the pipe cap and the probe. Since the deposit probe traversed the reactor diameter, similar arrangements are made for the sample port on the other side to prevent leakage of air into the reactor. The deposit probe is adjusted to position each of the sleeves on the probe such that each covers half of the gas flow diameter.

Deposits begin to form on the sleeves as soon as the probe is inserted in the reactor. After insertion, the probe surface temperature increases to a controllable temperature ranging from 400 to 650 °C over a period of 20-30 seconds. After this initial jump in the temperature, the probe surface temperature decreases slowly (at constant cooling air flow) because of the insulating characteristic of the growing deposit. However, while the probe surface temperature decreases, the insulating nature of the deposit also results in an increase in the deposit surface temperature. In addition, the probe coolant temperature tends to decrease slightly as the deposit thickness increases. Alternative testing procedures allow for a constant probe surface temperature by adjusting the cooling air flow rate during the test. This results in an even more rapid increase of deposit surface temperature. This process is explained with a temperature plot in the preliminary test results section of the next chapter. Deposits grow for arbitrary times on the probe, with 30 minutes being typical for comparative tests.

After ash deposit collection, the deposit ash collection probe is removed and the probe location is closed. The reactor reaches steady state after minor disturbance due to deposit probe removal process. At steady state, the fly ash collection probe is inserted through the same sample location as is used for the deposition probe. Venturi air and cooling water provide the air sample flow and cooling required for the probe. Isokinetic sampling is established by adjusting the venture air so that the flux of sampling gases through the probe is same as that of combustion gases flowing through an area equal to the probe inside area. In other words, the velocity of sampling gases is unchanged while leaving the reactor and entering the probe. The fly ash collection period varies from 15 minutes to 30 minutes depending on fuel ash content. Fly ash collection involves air filter equipment with a filter paper in line to capture fine ash particles. This arrangement successfully captures particles of size 5 micron and above.

4.4.3 Sample preparation for SEM analysis

Deposit sample analyses included quantitative composition, imaging, composition maps, and morphological information, the last three obtained mainly from scanning electron microscopes (SEM) or microprobes. Composition information is generally obtained using energy-dispersive spectroscopy (EDS) in combination with these scopes. These analyses are based on x-ray energy. Quantitative X-ray analysis requires a flat and level sample surface. Since the deposit samples are only lightly bonded to the tube, the movable sleeve is cast in a low-viscosity epoxy (EPOES resin - Struers No. M1201025 and EPOAR hardener – Struers No. M1201026). The mold used in this process is made of 1/8 inch thick aluminum sheet cut and welded to form a shape as indicated in Figure 15. Prior to setting the deposit coated sleeve into the mold, the mold is lined with high-

temperature, high-vacuum grease as a releasing agent. The epoxy enters the mold slowly over a period of 3 – 4 minutes, to avoid any disturbance to the sample.

After the epoxy cures for approximately 12-16 hours, samples are removed from the molds and labeled with a permanent marker. The samples are then cut on a band saw perpendicular to the surface to provide a cross-section of the deposit as shown in Figure 15.

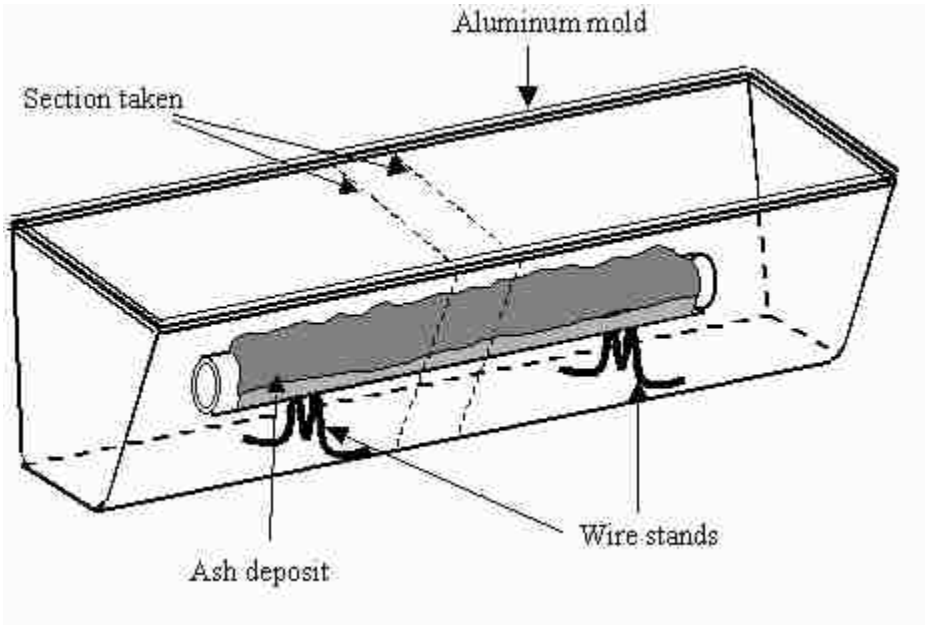

Figure 15: Schematic of sample preparation and sample section

The samples have average thicknesses of 1.0-1.5 cm. The samples are then polished to a 1-micron finish with successively finer sand paper and diamond paste. Polishing oil is used instead of water to minimize loss of alkali salts or other water-soluble compounds by dissolution in water. The samples are then cleaned by wiping the oil with tissue paper followed by impingement of high pressure air to remove the oil from

epoxy cracks, if any. Finally, the samples are coated with a thin layer (~ 1 Ångström) of carbon in a vacuum evaporator to make the surface conductive.

Any of several available scanning electron microscopes perform the analyses, with the JEOL 840A located in Brigham Young University's Electron Microscopy Laboratory being the most commonly used instrument for this investigation. The SEM is equipped with a Link Tetra retractable backscattered electron detector, a Pentafet light element detector, and a Link ISIS X-ray analyzer. The light element detector is equipped with a MOXTEK ultrathin window, which allows the detection of elements heavier than boron. The SEM is also equipped with a Link LEMAS stage automation system which, when connected to the link ISIS system, provides for computer control of the x and y location of the sample stage. The Link ISIS X-ray analysis system allows the user to collect and store backscattered electron images (BSEs) and automatically scan the image to identify inorganic material based on brightness. The brightness depends on the X-ray signal, which in turn is a function of density or atomic weight of elements present in the sample. Figure 16 shows an example of the SEM image data obtained from the equipment JEOL 840 A. The speed mapping feature of X-ray analysis produces individual X-ray maps of each element found over the scanned image area. The elements of interests are first selected on the X-ray spectrum according to the respective peaks. In each of the X-ray maps in Figure 16, the presence of an element over that area scales with brightness. If the elements produce very weak signals (are present in very low concentrations), it is possible that background noise may dominate the X-ray map.

In Figure 16, starting with the iron map, the bright area shows the part of metal sleeve containing mainly iron. The top edge of the bright area in the map represents the

outside surface of probe on which deposit accumulates. The potassium and chlorine maps indicate fairly uniform layers of potassium and chlorine located on the iron surface, consistent with the presence of potassium chloride. In addition, the bright areas associated in potassium and silicon maps, show presence of potassium silicate and similar association between calcium and silicon map show presence of calcium silicate. In the sulfur map, no bright areas appear, indicating no sulfur presence, which is consistent with the fact that biomass, in this case straw, usually contains very little sulfur. Similar SEM image analyses from all tests provide similar semi-quantitative and qualitative information.

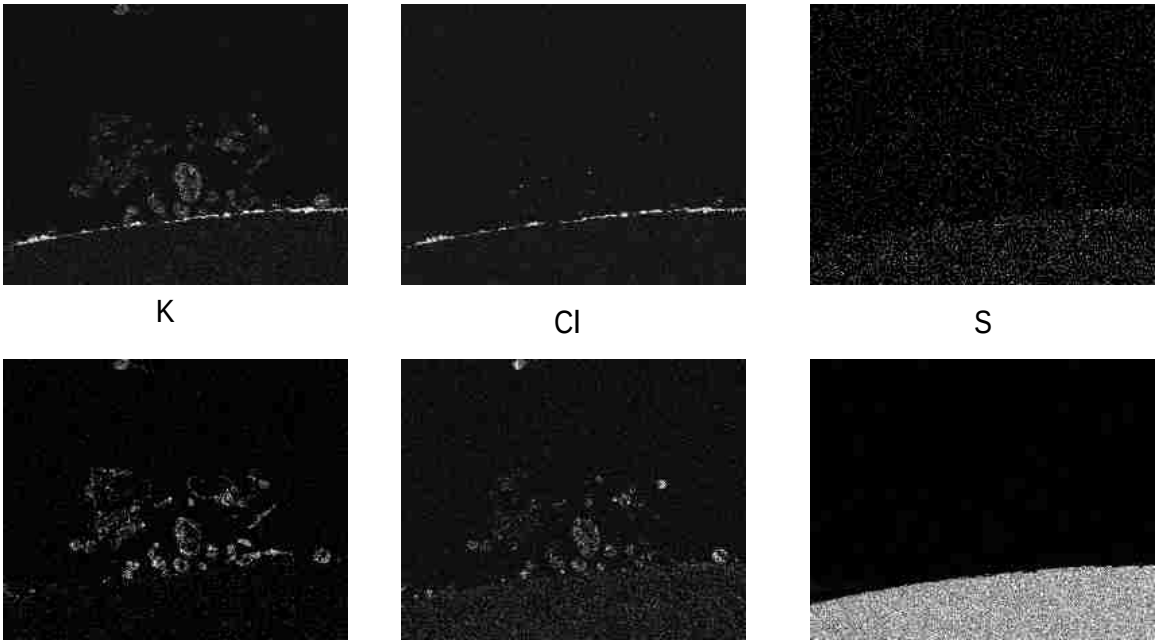

Figure 16: SEM X-ray map of pure Straw ash deposit (150X)

4.4.4 Particle impaction test procedure

To capture well-defined and isolated particle impaction videos, the reactor fuel feed rate ranged from 10 to 20 g/hr. Fuel was entrained in the primary air. During reactor

start-up, the reactor electrical power, gas feed rates, and cooling water subsystems come on line according to a written operating procedure (see Appendix A). Cooling water valves adjust water flow to a reasonable value to keep the feed probe cool. The SCR power controllers for three sections (top, middle, and bottom) control the reactor and secondary air preheater temperature rise and ultimate control at 1200 ^{o}C. Generally, it takes about 2-3 hours to achieve the set temperatures at a rate of 5-7 ^{o}C/min. By using a clamp ammeter, the current level in each heater cable remains below 160 A to prevent damage to heating elements. A total of nine thermocouples measure reactor wall temperatures and the preheater temperature. An orifice plate arrangement measures primary and secondary gas flows. The primary and secondary gas flow rates depend on the residence time of interest. The fuel-feeding process requires filling a syringe with desired fuel particles and replacing it in the feeding assembly. A computer connected to the motor controls the fuel feed rate. Periodic checks for feeding assembly are required to detect any possible blockages in feed line.

After fuel particles undergo combustion through most of the reactor length, ash particles continue through the bottom section flowing across a simulated deposit probe (similar to one used in Multifuel flow reactor) before entering the vacuum operated exhaust vent. The cameras placed at 90^{o} capture video of particle flow across the simulated deposit probe (see Figure 17). Nominal capture time varies between 7-10 seconds. Camera software saves video in a frame-by-frame format, which assists in calculating particle velocities (see Figure 18).

Camera settings, such as focal distance, exposure time and shutter speed, were kept the same during image capture of the measuring tape and impacting particles. A

sequence of particle impaction images with the measuring tape image indicate the distance traveled by the particle based on the length of the particle streak in each image (see Figure 18). This method provides incident and rebound particle velocities.

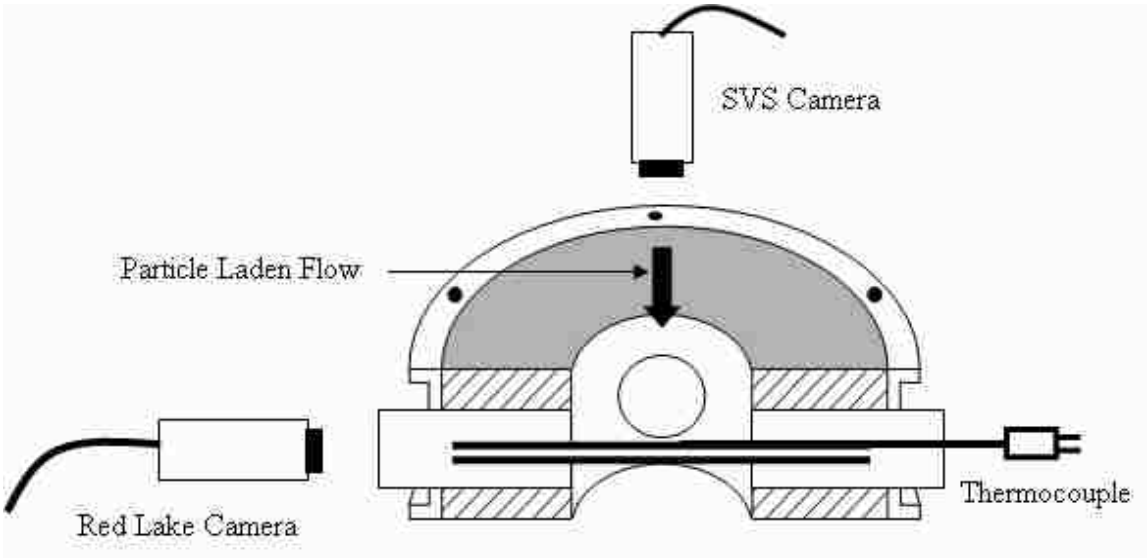

Figure 17: Particle impaction imaging set up

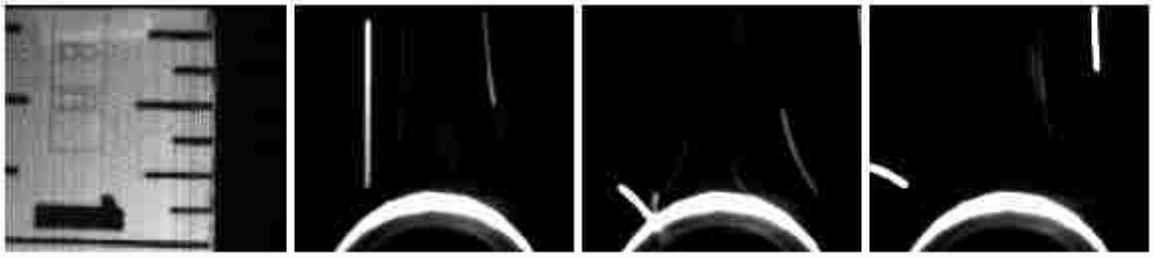

Figure 18: Images showing impaction and rebound of glass particles off the impaction surface

4.4.5 Condensation test procedure

Sodium chloride (NaCl) vapor condensation in pulverized-coal or biomass-fired boilers represents one of the most prominent and troublesome condensation mechanisms.

The entrained flow reactor accurately simulates the temperatures and environments in which this happens while isolating this mechanism, which contributes relatively minor amounts of total deposit mass, from the more dominant impaction mechanisms. Coal or biomass fuels from the fuel matrix were not used as NaCl source, to avoid interference from the other mechanisms, like inertial impaction, thermophoresis, eddy impaction, with vapor condensation. Also, the operating reactor wall temperature (1200 ^{o}C) is not sufficient for converting solid NaCl to vapor phase (T_{boil} = 1465 ^{o}C). Therefore, liquid methanol dissolved NaCl in various amounts and the solution formed the fuel, producing a range of fuel chlorine fractions comparable to those in coal and biomass fuels and at flame temperatures high enough to ensure complete vaporization (see Figure 19). Table 10 shows NaCl solubility in methanol.

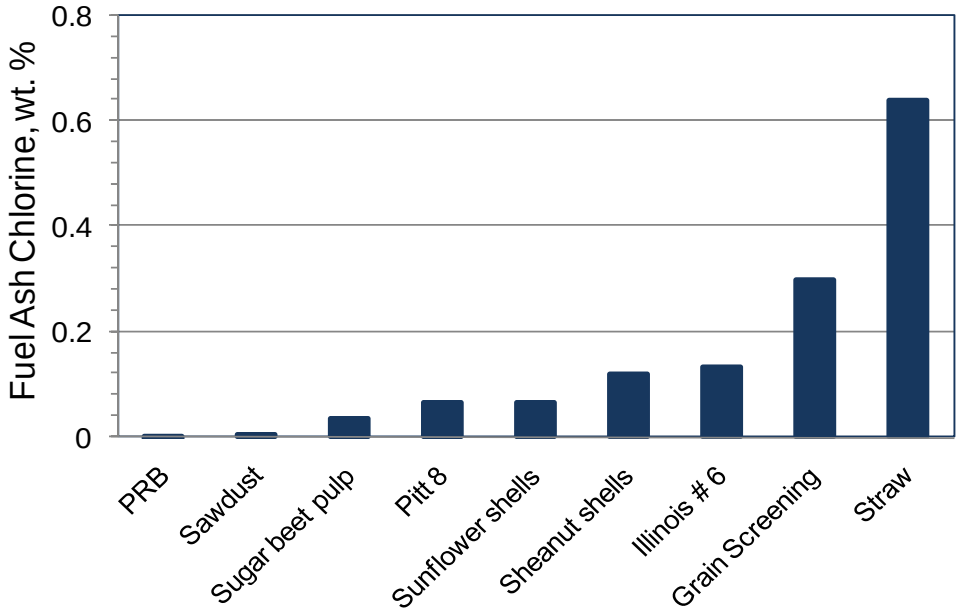

Figure 19: Fuel chlorine variation in coal and biomass fuels

Table 10: NaCl solubility in Methanol

Temperature , K	NaCl solubility in Methanol, gm NaCl/100 gm solution
298.15	1.375
303.15	1.360
313.15	1.310
323.15	1.235
333.15	1.220

Table 11 presents methanol-NaCl mixture fractions. These mixture fractions replicates gas phase NaCl mole fractions in coal/biomass combustion products over a wide range of fuel chlorine fractions. The same amount of methanol (19.65 gm) is used in each case with varying NaCl amount. The solution of NaCl in methanol readily ignites as it enters the reactor, vaporizing all of the NaCl in the gas phase. Some biomass fuel samples contain over 2% chlorine, but these are extreme cases of which none were found in the suite of fuels examined here. The range of chlorine concentrations simulated here is much higher than those found in US and most international coals of commercial significance.

Table 11: Test matrix for condensation experiments

Coal/Biomass Combustion		Methanol-Air combustion		
Cl % in solid fuel	Gas phase NaCl mole fraction	Methanol, gm	NaCl, gm	Gas Phase NaCl mole fraction
0.0005	0.0000003	19.65	0.00008	0.0000003
0.05%	0.0000348	19.65	0.011	0.0000355
0.10%	0.0000696	19.65	0.022	0.0000710
0.20%	0.0001392	19.65	0.043	0.0001387
0.30%	0.0002088	19.65	0.065	0.0002096
0.40%	0.0002784	19.65	0.086	0.0002774
0.50%	0.0003480	19.65	0.108	0.0003483
0.60%	0.0004176	19.65	0.13	0.0004192
0.70%	0.0004872	19.65	0.151	0.0004869
0.80%	0.0005567	19.65	0.173	0.0005578
0.90%	0.0006263	19.65	0.194	0.0006254
1.00%	0.0006958	19.65	0.216	0.0006963

A minor perturbation of the feeder mechanism used in the particle impaction experiment also fed the NaCl-methanol solution. Instead of a plastic syringe used for the particle feeding, a glass syringe was used with a layer of insulation material around the syringe to prevent the solution from getting warm. The feeder motor speed controls the methanol-NaCl solution feeding period to approximately 5 minutes. At the start of each experiment, a clean, weighed, thermocouple-instrumented, stainless steel tube (1/2" OD) placed in cross flow at sampling location forms the deposition target. The tube rises to a constant surface temperature, typically 530-540 ^{o}C, before starting the solution feed system. The air flow rates maintain a stoichiometric ratio of 1. After these preliminary steps, the feeder activates, marking the beginning of the experiment. After 5 minutes, the feeder stops, marking the end of the experiment. After cooling, the deposition target weight and the deposit weight (as determined by difference) are determined with a Scientech SM-50 analytical balance, which has accuracy of 0.01 mg. The difference between tube weight before and after the test is noted as NaCl amount condensed over 5 minutes. Further calculations convert this data in NaCl flux from gas phase to tube surface. Four replicated experiments for each NaCl-methanol mixture provide data needed for statistical analysis of the results.

4.4.6 Particle impaction on particulate layer

The experiments for particle impaction on particulate layers also used the entrained flow reactor. The test coupons from condensation experiments provided impaction targets. Here, the condensed layer is assumed to be made of multiple layers of fine particles. Test coupons from condensation tests with simulated 0.1, 0.2, 0.4, 0.6, 0.8, and 1.0 % fuel chlorine were used for these experiments. The particle sizes and incident

velocities were the same as those in the experiments for particle impaction on rigid surfaces, as discussed earlier. These experiments are performed to obtain particle rebound velocity data only, and not the mass accumulation data. During each test, the particle impaction is captured and then compared to the images of the tape measure to calculate rebound velocities.

5 Results and Discussions

This section presents the results from ash deposition research work in several parts. Each part includes numerical results, graphical and/or pictorial data and subsequent discussions with explanation for the behaviors observed.

5.1 Ash deposition model

The general ash deposition model described in literature review is investigated by selecting significant contributors to ash deposition process: inertial impaction, condensation. With this primary assumption, the general ash deposition model has a form as follows:

$$\frac{dm}{dt} = I \cdot G + C \qquad 5.1$$

Ash deposit from the other three mechanisms, thermophoresis, eddy impaction and chemical reaction, generally contributes little mass compared to total deposition rate, dm/dt and, in any case, is not treated in this discussion.

Inertial impaction occurs when particle inertia toward the target surface is greater than aerodynamic forces trying to make the particle move along streamlines. Among all particles that impact the surface, some bounce off the surface while the remaining particles stick to the surface. The capture efficiency, *G*, represents the fraction of particles that impact the surface and actually stick. Capture efficiencies are highly dependent on the physical properties and characteristics of the ash. Capture efficiencies are anticipated

to vary significantly between the fuels tested. The inertial impaction mechanism can be modeled by Equation 5.2. The term $\dot{m}_i$ represents the rate of mass deposition on a tube surface by inertial impaction. The first term on the right side ($\dot{m}_f X_a / A_r$) is the ash flux (g/cm^2-s) within the reactor. This term when multiplied with the probe's projected area (A_p) produces the total amount of ash that could impact a tube. This is then multiplied by the fraction which actually impacts the tube, η – impaction efficiency, and the fraction that sticks to the tube, G – capture efficiency.

$$\dot{m}_i = \frac{\dot{m}_f X_a}{A_r} A_p \, \eta \, G \qquad 5.2$$

Where:

$\dot{m}_f$ = mass flow rate of the fuel (kg/hr)

X_a = mass fraction of ash in the fuel

A_p = projected area of cylindrical deposit collection probe (cm^2)

η = the impaction efficiency

G = the capture efficiency

A_r = reactor cross section (cm^2)

The absolute magnitude of the deposited mass depends not only on the deposition characteristics of the ash but also on the probe area and fuel flow rate. To account for these operationally dependent variables, the data appear in terms of collection efficiency (ζ) as shown in Equation 5.3.

$$\zeta = \frac{\dot{m}_i / A_p}{X_a \dot{m}_f / A_r} = \eta \, G \qquad 5.3$$

As the above analysis indicates, an accurate description of η and G results in prediction of accurate collection efficiency of any fuel given the physical and chemical properties. Therefore, the next two subsections discuss the models constructed to predict impaction efficiency and capture efficiency.

5.1.1 Impaction efficiency correlation

The impaction efficiency, η, depends on: particle velocity (V), particle density (ρ), particle diameter (d_p), fluid viscosity (μ_g), and the target's characteristic length (d_c). These variables form two dimensionless parameters, a modified Reynolds number and dimensionless length d_p/d_c, which in turn produce the Stokes number. This dimensionless parameter (Equation 5.4) correlates with impaction efficiency according to Equation 5.5.

$$Stk = \frac{\rho_p d_p^2 V_p}{9 \mu_g d_c} \qquad 5.4$$

$$\eta(Stk) = \left[1 + b(Stk - a)^1 - c(Stk - a)^2 + d(Stk - a)^3\right]^{-1} \qquad 5.5$$

Israel and Rosner (Israel 1983) reported values of the constants a, b, c, and d as 0.1238, 1.34, -0.034, and 0.0289, respectively, on the basis empirical correlations to modeled results. The model used traditional particle trajectories and a potential flow field around a cylinder in cross flow. Potential flow fields only qualitatively describe actual flows around cylinders. The current investigation explores the difference in predicted impaction efficiency when using more rigorous flow field simulations compared to the potential flow approximation and when compared to experimental data.

The present investigation simulates a portion of the MFR including the deposit sampling location using Fluent to provide a more rigorous flow field approximation. This

model simulates inert particle injection in a high-temperature, viscous-flow environment. Figure 20 shows the GAMBIT-generated grid for this problem using GAMBIT. It is a 24” long and 6” wide flow domain with a 0.5” cylindrical tube in cross flow simulating the ash deposit probe. The mesh indicates cell concentrations near reactor and probe surfaces, accounting for higher gradients (temperature and velocity) near the walls. The reactor lengths before and after the probe location ensure a fully developed flow entering and leaving the selected flow domain. This accounts for most windward-side disturbances in the flow introduced by the presence of the deposit probe in a fully developed gas flow.

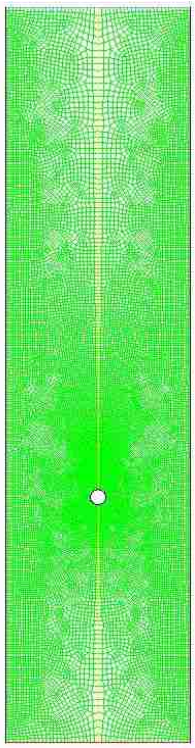

Figure 20: Grid structure for impaction model

Figure 21 shows a predicted steady-state temperature profile (rotated by 90 degrees during post-processing) of hot gases flowing across the deposit probe. The inlet

gas temperature is 1300 K. Reactor wall temperatures (1150 K) and deposit probe surface temperatures (800 K) remain constant, allowing for heat loss through reactor walls and also accounting for heat transfer to cooling fluid inside deposit probe. This and all other calculations represent a steady-state solution.

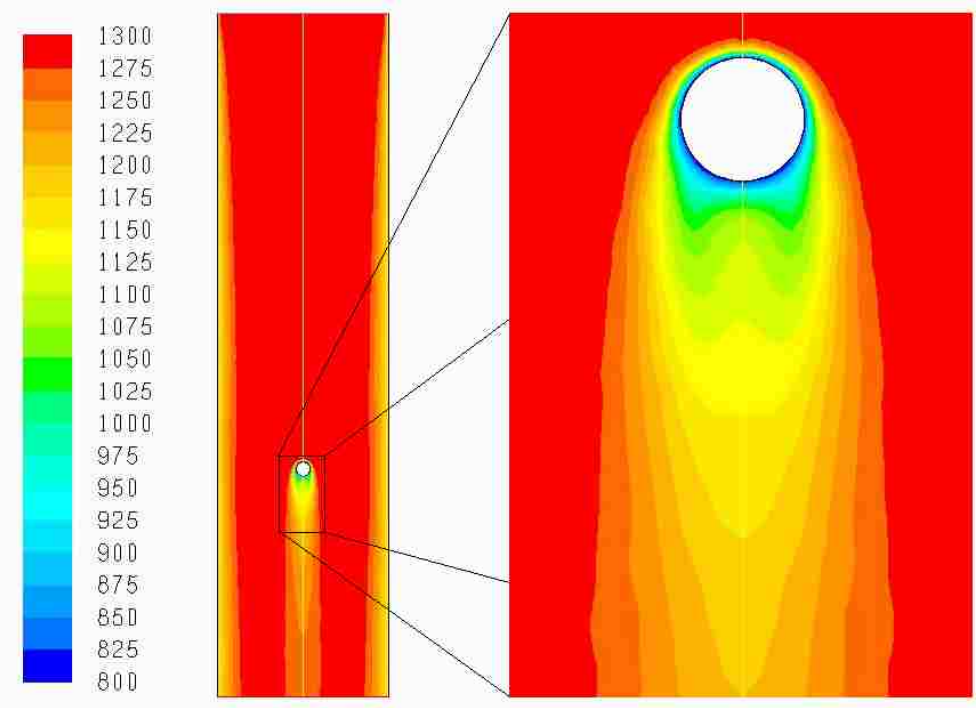

Figure 21: Temperature profile near ash deposit probe

While the average values of temperature (velocity, pressure, etc.) may be accurate averages, flows across right cylinders and most other blunt bodies essentially never reflect these averages. Even in steady-state flows, they are highly time-dependent, with eddies, temperature profiles, cooling rates, etc. oscillating from side to side in a well-documented recurring pattern. The velocity patterns at isothermal condition form what are often called a vortex street (see Figure 22). Thus, these average values are highly non-representative of actual behavior on the leeward side of the probe. However, nearly all of

the behavior important to this investigation occurs on the windward side of the probe, were average values are quite representative of actual behavior.

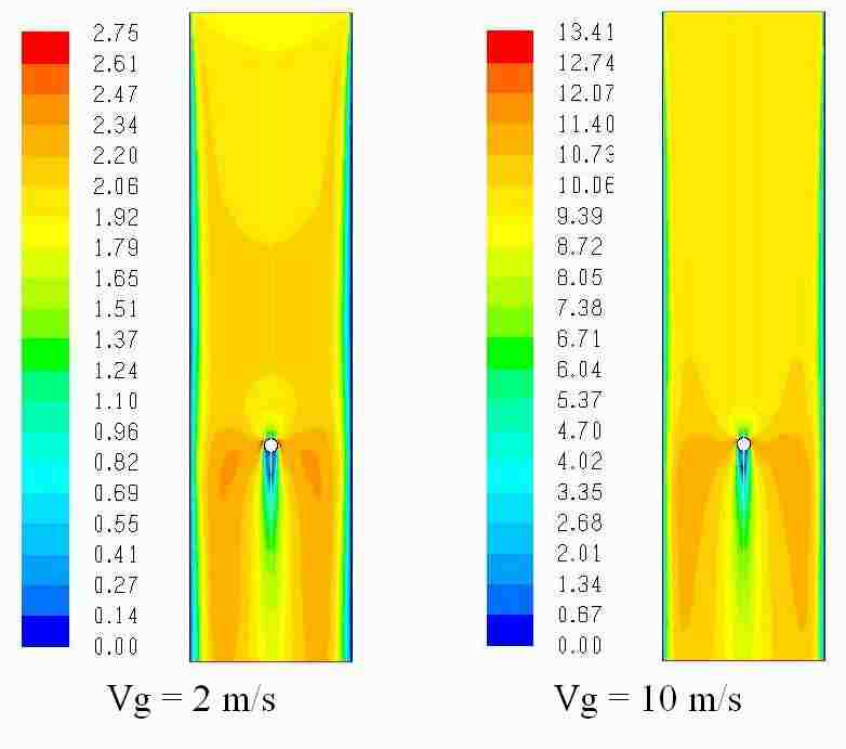

Figure 22: Gas velocity profile around ash deposit probe

A geometric definition for the impaction efficiency, such as is shown in Figure 23, forms an efficient and instructive framework for this discussion. Impaction efficiency is estimated from the ratio of x, the distance between the symmetric farthest particle streaks making contact with cylinder, to D_c, the cylinder diameter.

$$\eta = \frac{x}{D_c} \qquad 5.6$$

This definition of impaction efficiency is especially useful in analyzing variation in impaction efficiency due to upstream pressure deviations from the potential flow

solution causing changes in streamline patterns of the gas flow. The calculations lend themselves to easy calculation of impaction efficiency by this definition, and the remaining discussion focuses on such results.

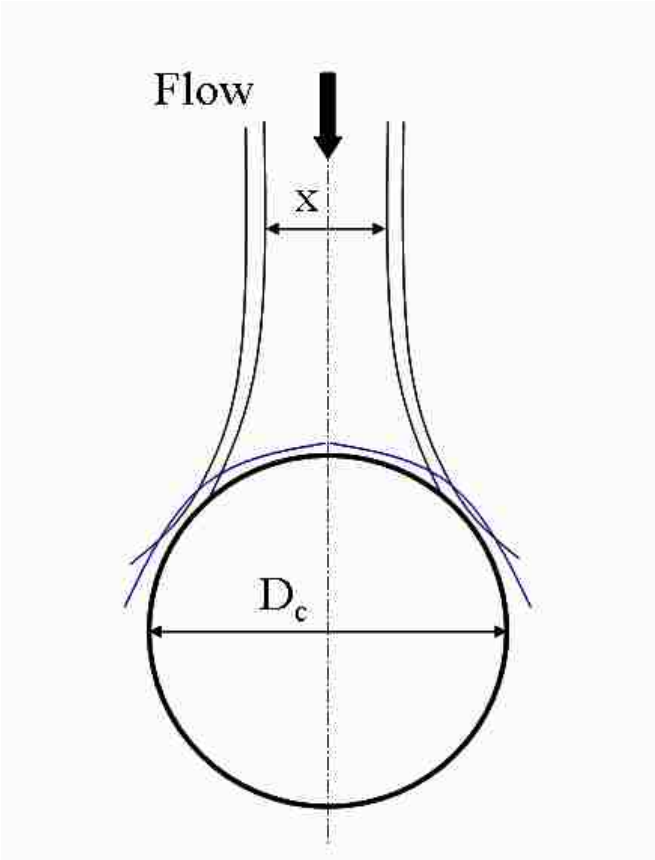

Figure 23: Particle impaction efficiency calculation

Figure 24 illustrates impaction of 20 micron particles at two different gas velocities, 2 m/s and 10 m/s. The lines represent particle streaks, not the gas streamlines. At low velocity, the particles tend to follow along the gas streamlines; at high velocities, particles approach the target surface with higher momentum, break away from gas streamlines and impact the surface. For example, for impaction at low velocity, only two particles streaks, spaced adjacent to the centerline on either side, successfully impact the

tube surface. For high velocity, the number of particle streaks contacting the probe surface is 12. This number, along with particle spacing at injection surface, returns the value of x in the impaction efficiency equation. This method produces the predicted impaction efficiency for each case of this model.

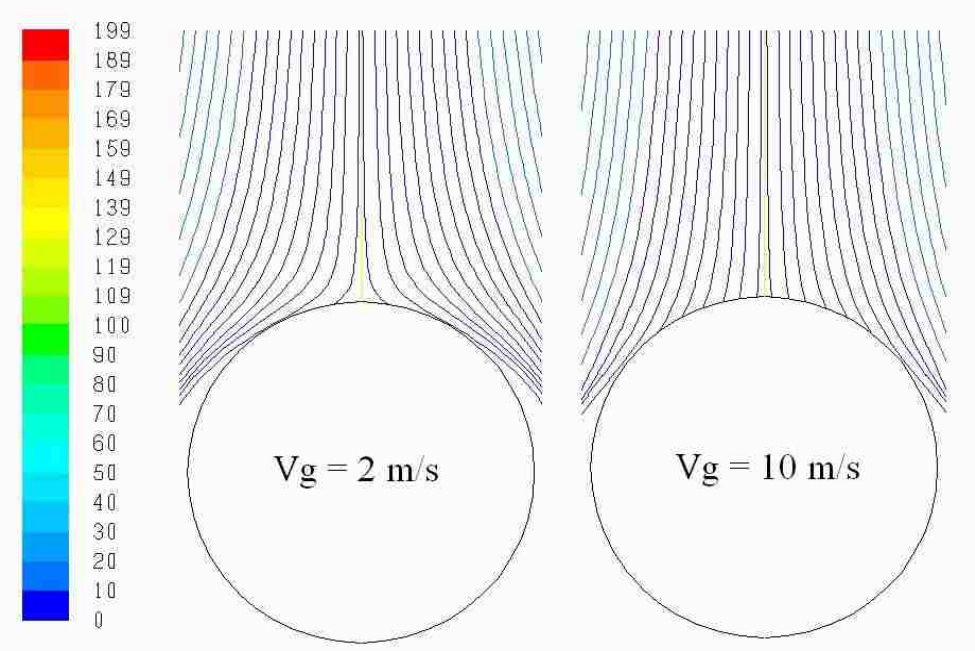

Figure 24: Particle impaction on deposit probe at two velocities

Thus, impaction efficiencies range over velocities and particle diameters to produce a Stokes number range of 0.1-150. This specific range of Stokes numbers corresponds to a span of η from near 0 to essentially 100%. These data form a correlation for $\eta = f(\mathrm{Stk})$, which assumes the form shown in 5.5 with the coefficients listed in Table 12. The coefficients for inviscid flow come from the original work of Israel and Rosner, which appears along with the new correlation in Figure 25, and uses a potential flow field to determine particle impaction efficiencies in an otherwise similar manner.

Table 12: Coefficients for impaction efficiency correlations

	a	b	c	d
Inviscid Flow	0.1238	0.134	-0.034	0.0289
Viscous Flow	0.1101	2.0762	-0.2553	-0.0224

The strong dependence of Stokes number on particle size ($Stk \alpha d_p^2$) resulting in small impaction efficiencies associated with small particle sizes (see Figure 25). Small particles have less momentum and are unable to separate from gas streamlines. Therefore, the impaction efficiency drops as Stokes number decreases. On the other hand, larger Stokes numbers (larger particle sizes, high velocities, or high densities) imply greater momentum, which allows particles to break away from streamlines and successfully penetrate boundary layers to impact the target surface.

As shown in Figure 25, impaction efficiencies for viscous flow are lower (by 15-40%) than those for inviscid flow. This decrease in impaction efficiency results from the pressure and velocity behaviors upstream of the target cylinder. In the case of inviscid flow, since the working fluid (air in this case) does not offer any resistance to shear stress, it follows a smooth streamlined pattern very close to the cylinder surface. However, in applications involving viscous (real) flows, working fluids always offer some resistance to shear stress. This results in slower fluid velocities over a larger area upstream of the probe compared to the inviscid calculations. Due to fluid viscosity decreasing velocity, pressure increases well upstream of the flow and is propagated backwards along axis of the flow geometry. This pressure zone along the axis alters the gas streamline patterns by pushing them away from the symmetry axis. Subsequently, particles influenced by this flow are pushed away not only from the axis, but also from

the target cylinder. Figure 26 illustrates the differences in the gas stream lines for a viscous and inviscid flow that are identical in all other aspects. The figure illustrates flow streamlines past a deposit probe in inviscid (left side, flow from right to left) and viscous flow (right side, flow from left to right). The streamlines plots are presented such that axes from both plots are collinear. The back-to-back upstream gas streamlines show the differences in distance between respective streamlines in the two flow patterns.

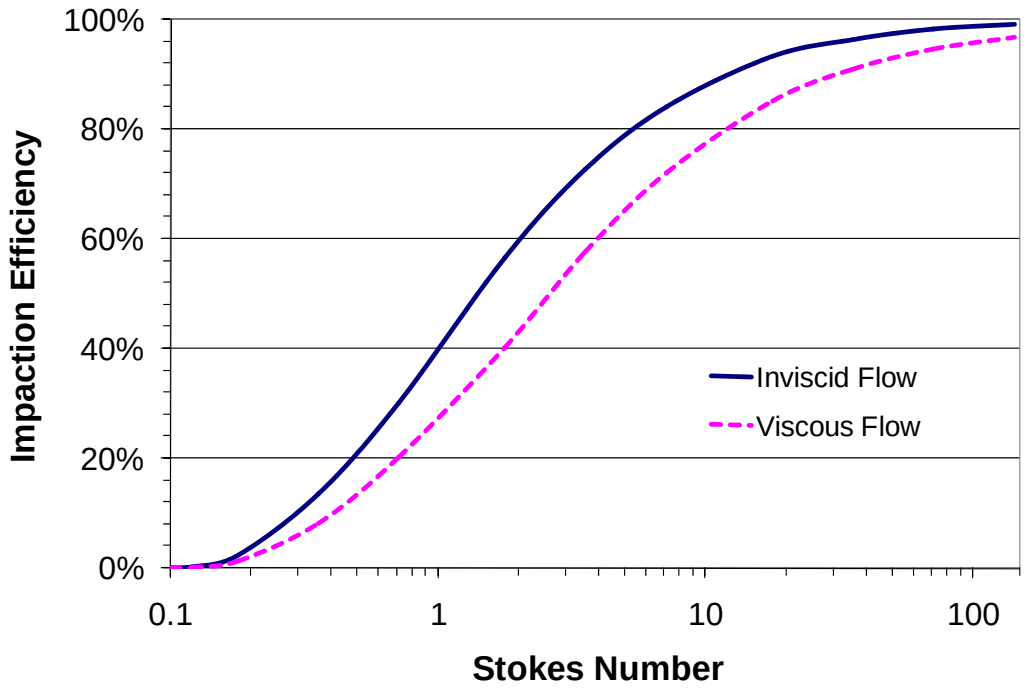

Figure 25: Impaction efficiency comparison for inviscid and viscous flows

The plot indicates that, as y goes from 0 to the probe radius, the viscous flow streamlines are more widely spaced (indicate lower velocity) than the inviscid flow streamlines. As y increases beyond probe radius, the viscous flow streamlines are more narrowly spaced (higher velocity) compared to the inviscid simulation following law of mass conservation.

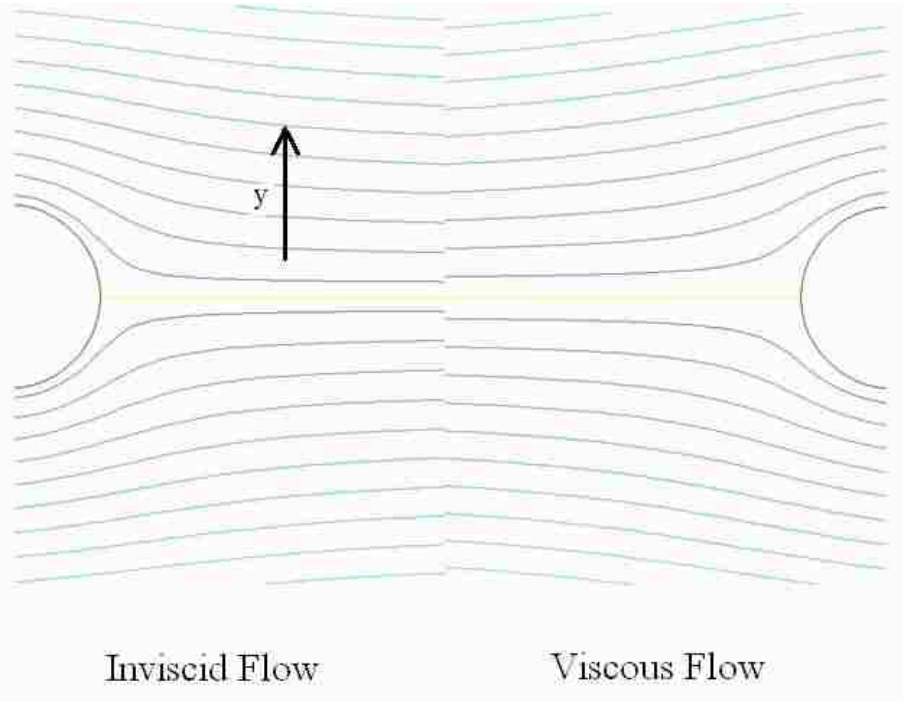

Figure 26: Upstream gas streamlines for inviscid (left) and viscous flow under otherwise identical conditions

The significant point is that the change from inviscid flow to viscid flow substantially changes the bulk flow gas streamlines, not just the boundary layer velocity profiles. Thus, in comparison to inviscid flow, in viscous flow, particles move away from the centerline farther from the axis, which decreases the probability of them impacting the target. This explains the drop in η by up to 40% as viscous effects are added to the flow dynamics. This difference appears most dramatically at intermediate Stokes numbers, however, according to Figure 25, the impaction efficiencies from both correlations converge to same values (0% and 100%) at Stokes number extremes of low and high values, respectively. As particles sizes decrease (Stk ~ 0.1), their behaviors are increasingly dominated by the gas. In both inviscid and viscid flows, they follow gas streamlines and flow past the cylinder without making contact. Thus, η approaches zero

in both cases. Similarly, for large particles (Stk >150), gas velocities minimally influence particle behavior. Regardless of flow type – inviscid or viscous – the large particles penetrate boundary layers and impact the target surface to a similar extent.

The results of an experiment designed to obtain impaction data over a wide range of Stokes number to validate these theoretical results appear in Figure 27. Combinations of particle size, particle velocity and target cylinder size constitute a test matrix for these experiments which covered Stokes number range from 0.1 to 150. The error bars on the data points (inside the circles as data points) represent 95% confidence intervals. The theory follows the experimental trend and successfully predicts impaction efficiencies within 10% of the experimental data.

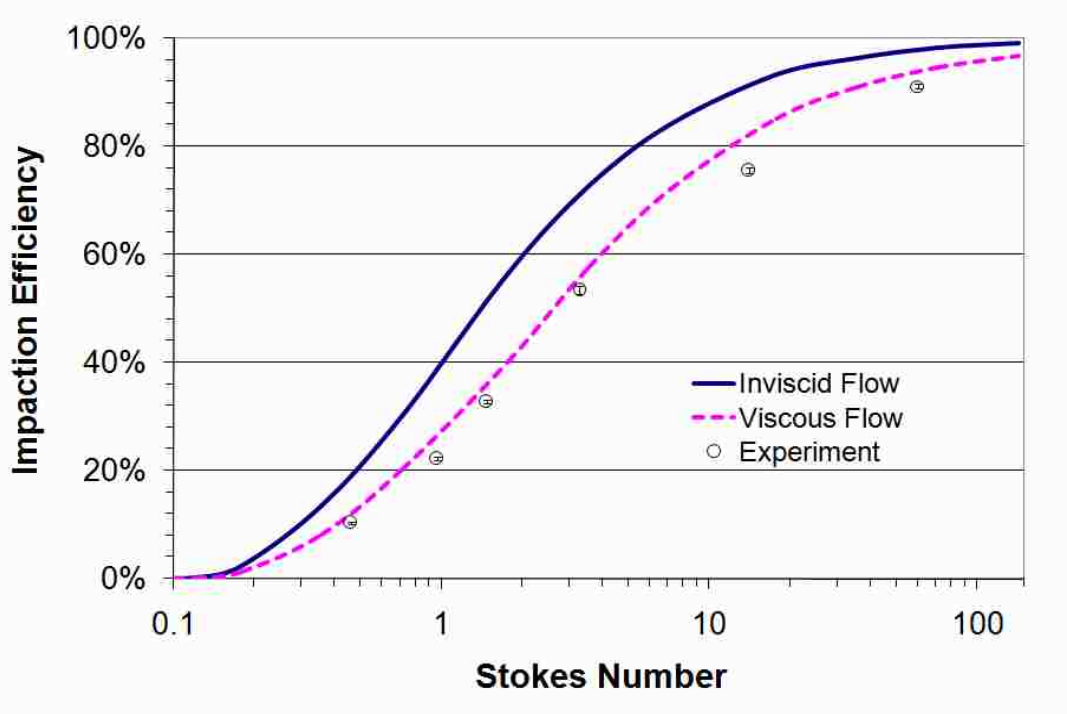

Figure 27: Impaction efficiency model validation

Although the new correlation of theoretical results agrees much better with the data than the traditional (inviscid) results, the data remain consistently lower than the theoretical predictions. This may arise from the most dominant experimental error – particles that rebound from the probe rather than sticking to it – always biasing the experimental results to lower numbers. There are no significant offsetting random errors that bias the results to larger numbers. While the data and theory demonstrate close agreement, agreement is not within the experimental error as estimated by traditional 95% error bars. However, this error estimate does not account for the bias explained above. We believe the theoretical results are the most reliable and have developed the correlation based on them, though the experimental results confirm a substantial improvement compared to the traditional correlation.

5.1.2 Capture efficiency analysis

The second part of the inertial impaction mechanism is particle capture efficiency. This is partly dependent on ash chemistry and partly dependent on the particle geometry and target surface characteristics. In this section, the discussion includes impaction and capture of spherical particles on various surfaces. This discussion presents results from a model constructed in the C++ programming language and experiments designed to validate different cases.

Case 1: Particle impaction and capture on rigid surface

This case involves impaction of solid spherical particles on a rigid surface such as a smooth metal wall of frozen slag surface. This case is generally seen in early stages of a boiler operation and/or in relatively cooler (<800 ^{o}C) sections of a boiler. During impaction/collision, the particles lose part of their kinetic energy. If the surface is

perfectly rigid, this energy loss depends on particle mass, velocity and chemical composition or ability to deform inelastically. The chemical composition of a particle determines its material properties such as elasticity, Young's modulus, and Poisson's ratio – the properties required for estimation of kinetic energy loss on impact. For diverse ash composition among fuels, it is a difficult task to estimate an accurate particle composition and estimate dependent particle properties. Therefore, materials with repeatable and known composition and that are similar to ash, (for example, mullite) are used for this model calculations.

A critical velocity model provides the basis for estimating kinetic energy loss. Here, critical velocity is a threshold particle velocity below which the particle, when it impacts a surface, does not rebound and is captured by the surface. Following is the analysis of the model. Critical particle velocity, V_{cr}, is

$$V_{cr} = \left(\frac{2B}{d_p} \right)^{\frac{10}{7}} \tag{5.7}$$

where,

$$B = 0.51 \left[\frac{5\pi^2 (k_1 + k_2)}{4\rho_p^{3/2}} \right]^{2/5} \tag{5.8}$$

$$k_1 = \frac{1-\nu_s^2}{\pi E_s},\ k_2 = \frac{1-\nu_p^2}{\pi E_p} \tag{5.9}$$

In the above set of equations, d = diameter, ρ = density, ν = Poisson's ratio and E = Young's modulus. The suffixes, s and p, represent surface and particle, respectively. The Poisson's ratio and Young's modulus of mullite ($3Al_2O_3$ $2SiO_2$) are used in this analysis. The objective of this analysis is to estimate a rebound velocity of a particle after impact

and this is accomplished by setting a kinetic energy balance over the particle during impaction and rebound. For this energy balance, kinetic energy lost during impact is approximated with kinetic energy of a particle with velocity, V_{cr}. This parameter correlates the kinetic energy absorbed when a particle impacts a surface and is captured. Therefore,

Incident kinetic energy, $KE_i = \frac{1}{2} m_p V_{p,i}^2$ 5.10

Kinetic energy lost during impact, $KE_{loss} = \frac{1}{2} m_p V_{cr}^2$ 5.11

According to kinetic energy balance,

$$KE_r = KE_i - KE_{loss} = \frac{1}{2} m_p V_{p,r}^2 \quad 5.12$$

Rebound velocity of impacting particle, $V_{p,r}$ is,

$$V_{p,r} = \sqrt{\frac{2KE_r}{m_p}} \quad 5.13$$

Thus, the C++ program (see Appendix B) produces particle rebound velocity of different particle sizes, which determines the coefficient of restitution, e, as the ratio of the rebound velocity component normal to the surface to incident same incident velocity component. Also, a set of experiments under controlled conditions provides rebound velocity data for the same particle size range (see Figure 28). In general, rebound velocities are approximately 10% lower than the corresponding incident velocities, resulting in a coefficient of restitution of ~ 0.9. Smaller particles (40 microns) lose less kinetic energy than the larger particles (200 microns). This model assumes that all particles are perfectly spherical in shape, therefore, two particles contact at a single point,

as does a particle with the surface. This assumption implies a negligible frictional or deformation loss on impaction. However, the spherical particle assumption is more accurate for smaller particles, as larger particles may lose their spherical shape and involve flat edges and faces. These edges and faces, when making contact with another particle or surface, increase frictional losses and result in lower rebound momentum and lower rebound velocity. Since the model does not consider this effect, a small deviation exists between the model and experimental data for larger particles (see Figure 28). However, the model follows the trend indicated by experimental data and predicts rebound velocities within 8-10% of experimental data.

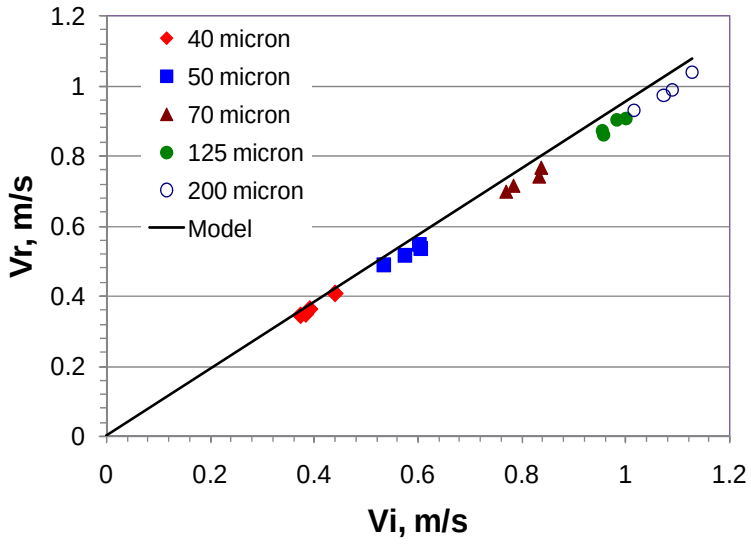

Figure 28: Parity diagram of rebound velocity measurements and estimation by model

Case 2: Particle impaction and capture on a surface with particulate layer

One of the most common instances of particle impaction in combustion applications falls in this category. Here, particles impact on a surface containing one or

more layers of previously deposited particles. The particle impaction and rebound mechanics are similar to those in Case 1, with an additional step that accounts for inter-particle collisions within the particulate layer. In this case, particles are loosely connected to each other and inter-particle collisions are assumed to be perfectly elastic collisions. Figure 29 shows the momentum transfer from an incident particle to a particle in the top layer (from position 1 to 2), through the particulate layer downward to the surface and from the surface upward to the original particle in the top layer (paths marked by the arrows), and finally back to the original incident particle (from position 2 to 3).

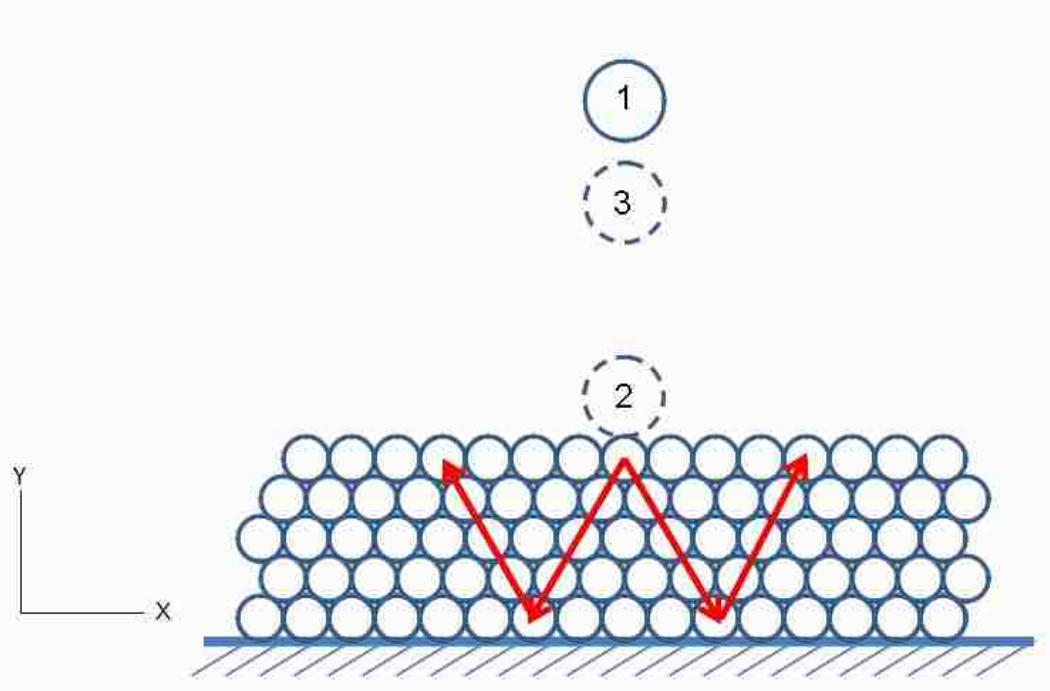

Figure 29: Momentum transfer during particle impaction on a surface with particulate layer

In this analysis, a trapezoidal portion (2-dimensional) of the particulate layer marked by the arrows is considered the impaction zone. This means, the transfer of

momentum is considered only to and from the particles present within this zone. In case of oblique impacts, only vertical components of velocities are considered while horizontal components are neglected. Our calculations show that momentum transfer to the particles outside this zone is negligible in comparison to that between the particles within the zone. This case of the model performs a momentum balance on each particle-particle and particle-surface collision and produces downward and upward velocities for each particle as impaction occurs. Such inter-particle collisions may cause changes in momentum from an incident particle resulting in lower rebound energy. This analysis considers the momentum exchange in a vertical monolayer, i.e. momentum transfer in z-direction, perpendicular to the picture plane, is not considered.

Figure 30 demonstrates this effect as rebound velocities decrease with increasing number of particulate layers and decreasing particle size. The particulate layer for impaction includes 20 micron particles. Since the collisions are always head-on for this model, for single particulate layer, the model returns the same results as in Case 1. However, an additional layer of particles is sufficient to cause a significant decrease in the rebound particle momentum. In Figure 30, all particles lose their momentum completely as the number of particulate layers reaches 4 or more. This illustrates a particle capture mechanism in absence of a particle deformation (e.g. molten ash). These model predictions become less valid as the size of the particles in the particulate layer increases, especially, if the particles are bigger than the incident particle. In such a case, particles in the layer may not be simply loosely connected and may involve complexities such as deposit strength due to sintering and other agglomeration effects. These details are not handled in this model.

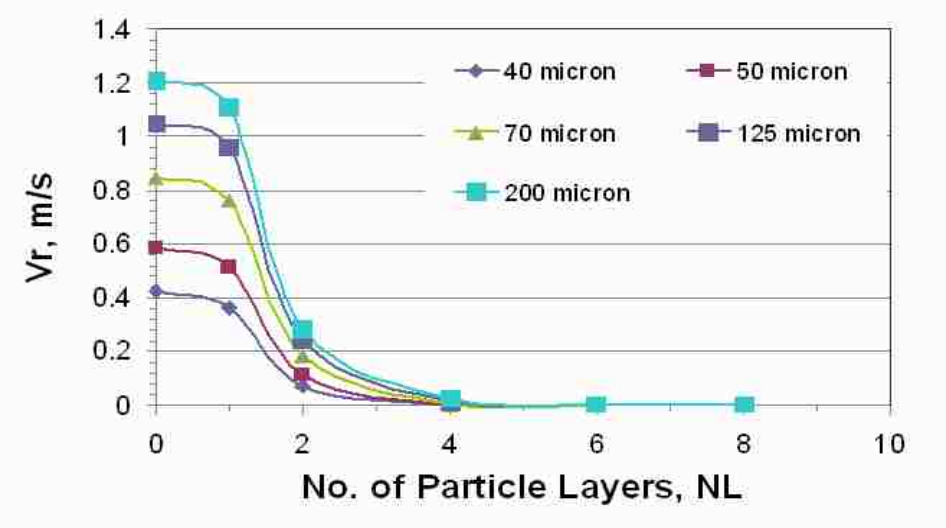

Figure 30: Rebound energy dissipation with increasing number of particulate layers

The experimental results for particle rebound velocity after impact on particulate layers appear in Figure 31. This plot illustrates rebound velocity as a function of incident velocity for various loadings of sodium chloride. The NaCl loadings indicate the fuel chlorine (wt.%) during the condensation tests. The probe surface and much of the thermal boundary layer are cooler than the NaCl fusion temperature, so the condensate forms small particles in the boundary layer and deposits as a film of typically submicron particles (Baxter 2004). The fine particulate loading is achieved by sodium chloride vapor condensation during the condensation experiments. For light loading of NaCl vapors, the impaction process is comparable to the impaction according to Case 1, except that the coefficient of restitution ranges from 0.5 to 0.9. This results from such a light loading that the particulate layer on the surface consists of a single layer, a discontinuous particulate layer, or such an easily disrupted layer that the impacting particle interacts mainly with the surface. This results in rebound of heavier particles without any significant loss in momentum ($e \sim 0.9$), however, light particles lose a significant fraction

of their momentum (e ~ 0.5). As NaCl loading increases, even heavier particles are affected by the momentum dissipation due to increased number of particulate layers on the surface. Some of the lighter particles carry relatively less momentum and get captured by the surface, while for heavier particles, the rebound velocity decreases significantly (e ~ 0.3).

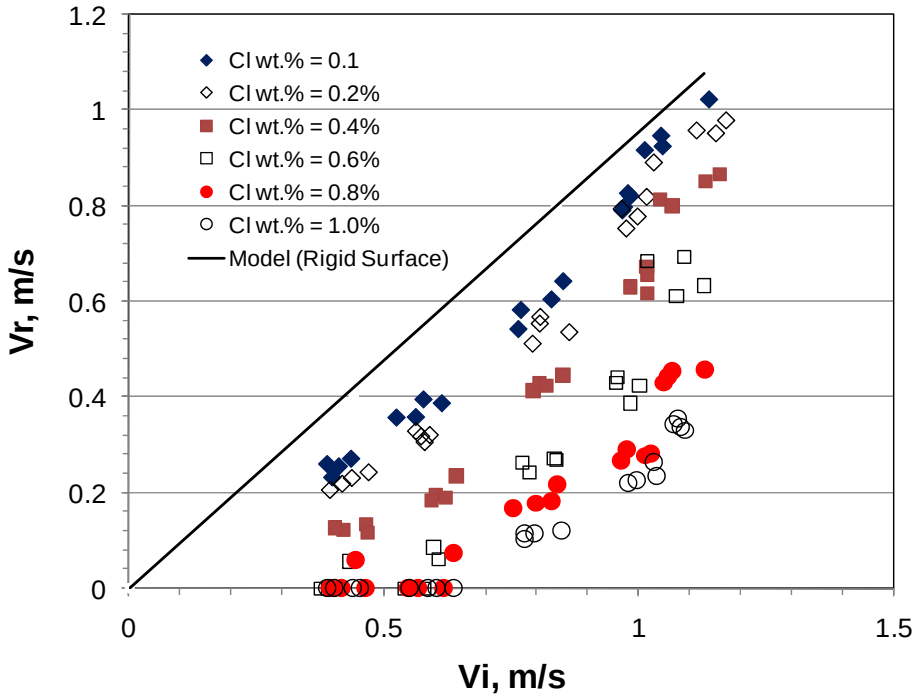

Figure 31: Rebound velocity estimation by experiments for impaction on a surface with particulate layer

The model results (see Figure 32) show similar trends and behavior as that of experimental data presented in Figure 31. The 1 layer graph, represents impaction on surface with light loading (X_NaCl = 0.1-0.2%), while 2, 4 and 6 layer graphs describe heavy loading effect. In reality, if the size of the particles in the particulate layer changes from 20 micron, it may change the number of layers with respect to various NaCl

loadings, but the trend and behavior would remain similar, and Figure 32 is one of such several representative trends.

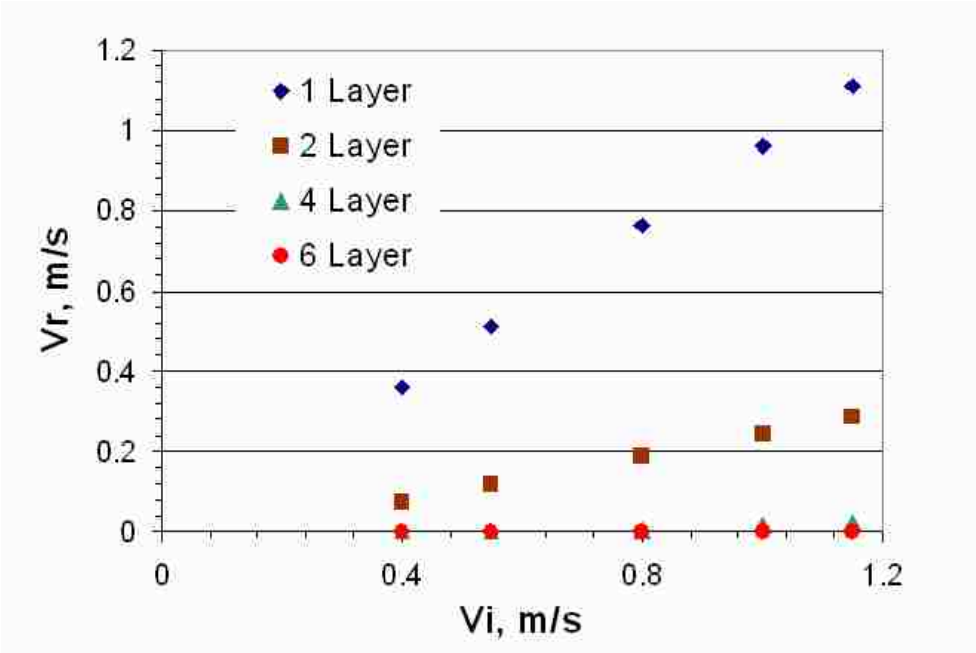

Figure 32: Rebound velocity estimation by the model for impaction on a surface with particulate layer

5.1.3 Vapor condensation analysis

This subsection presents analysis of alkali chloride vapor condensation on relatively cooler heat transfer surfaces. This analysis is an important aspect of the ash deposition model because condensation enhances ash deposition and it also assists corrosion by initiating the process. Figure 33 shows the wide variation in chlorine content of different coal and biomass fuels. Some coals (e.g. PRB) and biomass fuels (e.g. sawdust) contain negligible amounts of chlorine while straw, grain screenings and Illinois#6 coal are among high-chlorine containing fuels. Some biomass fuels with intermediate chlorine content (e.g. sugar beet pulp and sunflower shells) may have had

higher chlorine content initially. However, leaching processes during fuel preparation could extract some of the chloride salts.

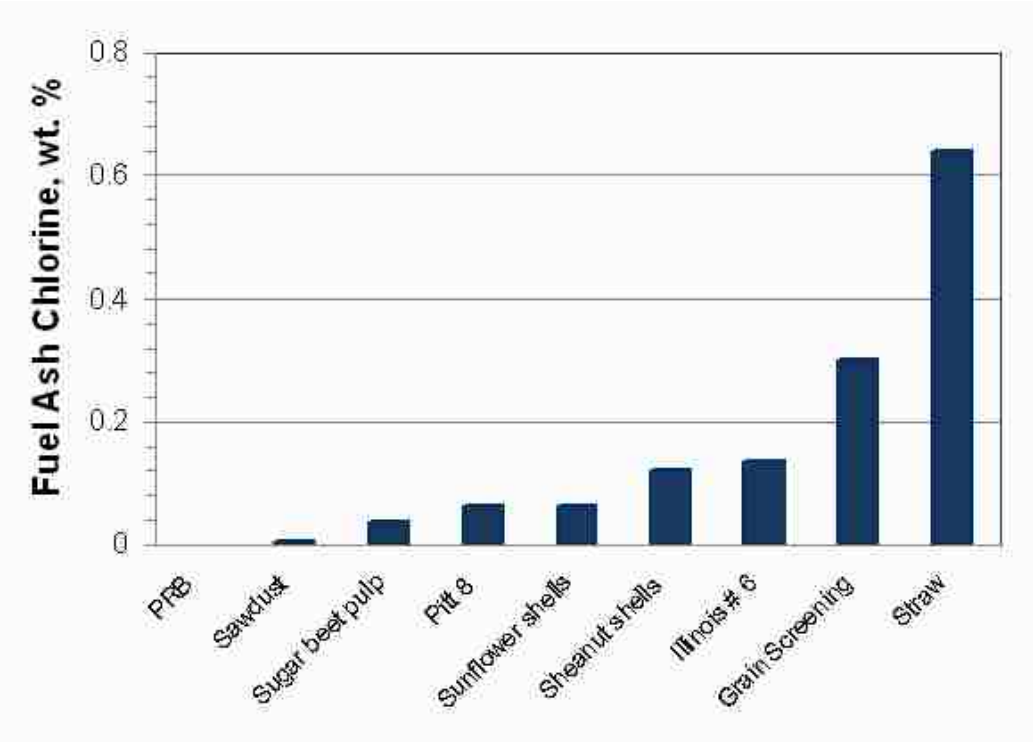

Figure 33: Chlorine variation in coal and biomass fuels

In general, such a variation in chlorine content results in a wide range of condensation rates, which normally depend on gas temperatures and gas-phase alkali chloride concentrations. The following discussion describes these experiments experimentally and theoretically. The model involves a mass transfer process governed by the phase change of NaCl from vapor to liquid/solid, and is described as follows:

$$\text{NaCl flux, } N_{NaCl} = \theta_m k_m c\left(\frac{x_s - x_b}{1 - x_b}\right) = k_m c \ln\left(1 + \frac{x_s - x_b}{1 - x_s}\right), \text{ gm/m}^2\text{-s} \qquad 5.14$$

where, θ_m = blowing factor, c = total concentration, x_s = surface NaCl concentration, x_b = bulk NaCl concentration, and k_m = mass transfer coefficient (See Appendix C for detailed derivation). The mass transfer coefficient is obtained from following correlation:

$$Sh_m = \frac{k_m L}{D_{AB}} = 0.3 + \frac{0.62 \mathrm{Re}^{1/2} Sc^{1/3}}{[1+(0.4/Sc)^{2/3}]^{1/4}} \left[1+\left(\frac{\mathrm{Re}}{282000}\right)^{5/8}\right]^{4/5} \qquad 5.15$$

The results from the model and experiments appear in the form of NaCl flux from gas to surface as a function of gas-phase NaCl concentration (see Figure 34). The error bars on experimental data are one standard deviation.

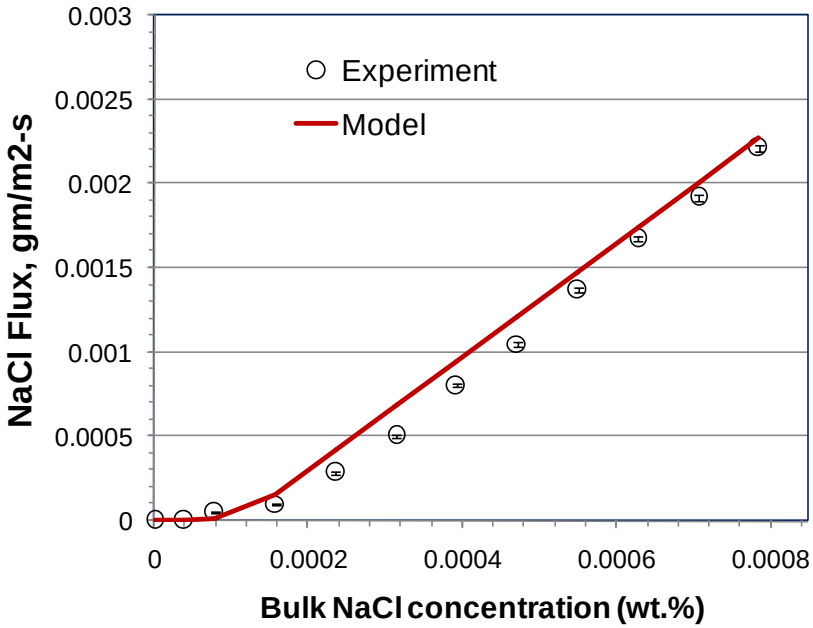

Figure 34: NaCl flux variation with bulk NaCl concentration

After an initial curve, the experimental data follows a straight line. The initial curve arises from the surface temperature variation with location from leading edge to trailing edge. For a specific surface temperature, the profile is always a straight line and it

intersects the abscissa at the NaCl saturation concentration associated with that temperature. A range of temperatures, instead of a single temperature, keeps the straight line part of the profile unchanged, but instead of intersecting the abscissa at the vapor saturation concentration, the profile follows a curved path as it approaches zero. To account for this effect in the model, the temperatures at different peripheral probe locations are measured with a thermocouple (see Figure 35).

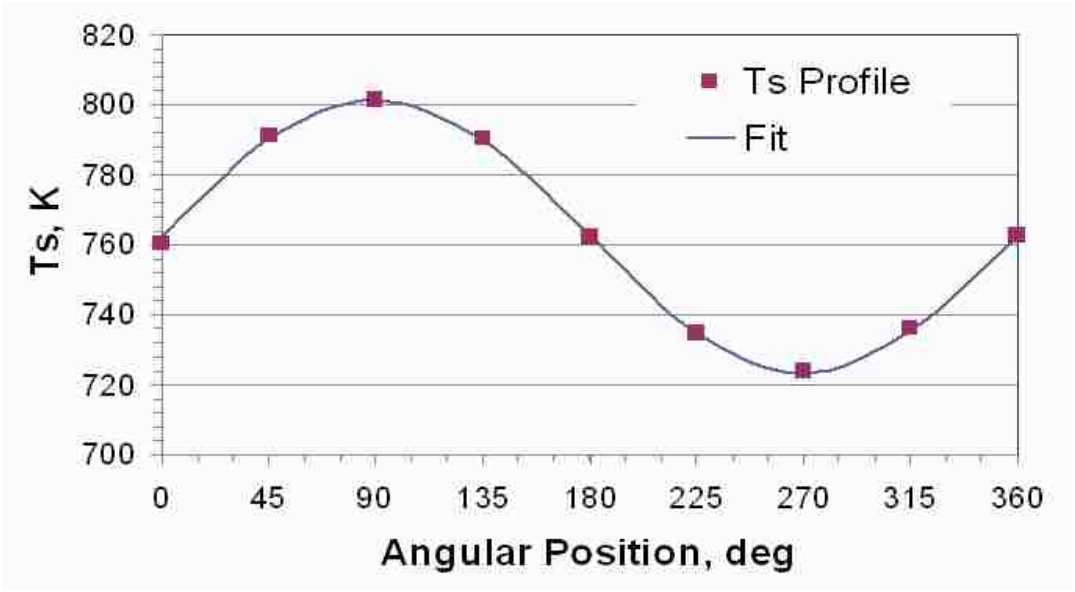

Figure 35: Surface temperature profile for condensation model

The experimental data are fit to a sinusoidal profile described as follows:

$T_s(\theta) = T_0 + T_1 \sin\theta$, where T_0 = 762.62 K, and T_1 = 39.03 K 5.16

The results of the model appear in Figure 34. The model follows the trend predicts NaCl flux within 15% of experimental data. It is apparent that for most of the

fuels with moderate chlorine content, the condensation occurs at a fairly linear rate; however, for fuel with low chlorine content, it varies exponentially.

5.1.4 Eddy impaction analysis

In this analysis, the effect of turbulent eddies on particle impaction is investigated by using Fluent. GAMBIT was used to construct a grid for the complete MFR. Only submicron particles with velocity ranges from 2.5 m/s to 100 m/s enter into the calculations. The parameter set covers a Stokes number range from 10^{-5} – 0.1, although Stokes number is, by itself, insufficient to characterize this deposition mechanism. The k-ω (2 equations) model describes turbulence. Particles flow in a group with the random walk model. Impaction efficiency computations involve the ratio of the number of particles trapped by a target cylinder to the total number of particles (500). Twenty replicated calculations provide an average value for impaction efficiency. Figure 36 shows impaction efficiencies of submicron particles as a function of Stokes number, with turbulent intensity ranging from 3 to 6 %. The figure shows only model results and its trends obtained by curve fitting. The figure does not show any experimental data for eddy impaction efficiencies. Data for every particle size follows a trend that is similar to the initial curve in the inertial impaction efficiency plot (Figure 27). However, instead of approaching zero as Stk decreases, all of these profiles approach a constant value of eddy impaction efficiency. This suggests that as particles get smaller, a limiting value of eddy impaction efficiency is achieved, approximately 1%.

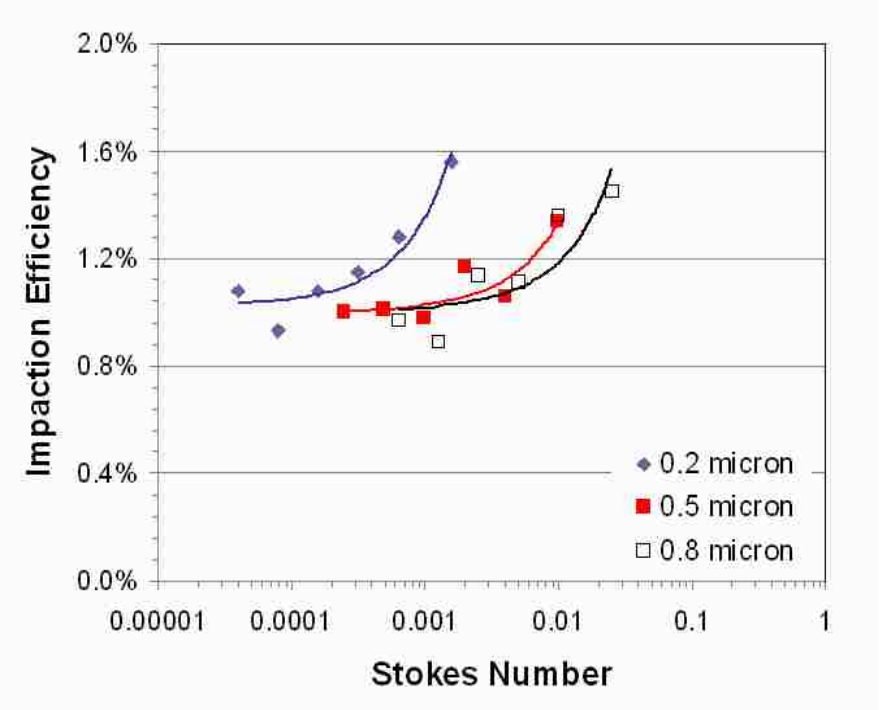

Figure 36: Eddy impaction efficiency for 0.2, 0.5 and 0.8 micron particles

This limiting value for efficiency reflects the limitations of the random walk particle model more than the physics of eddy impaction. In this model, statistical but arbitrary particle velocity changes simulate the impact of turbulence on particles. In reality, particles are entrained in gas eddies with velocities that vary from the mean. Small particles, in particular, rapidly assume that local gas velocity. In the context of most combustion systems, any particle less than about 5 micron is small in the sense of this behavior. A more rigorous eddy impaction model would not produce this limiting impaction efficiency.

The variation of eddy impaction with a bulk-flow Stokes number (based on bulk gas/particle velocity) does not relate fundamentally to eddy impaction efficiency rates in any case. In eddy impaction, particles are at the boundary layer edge and only impact

under influence of the turbulent fluctuations. The correlation seen above arises because turbulent intensity correlates with bulk velocity, but the fundamental relationship involves velocity fluctuations, not bulk flow velocities. As velocity fluctuations increase, deposition rates increase, consistent with the predictions. However, the random walk model incorrectly predicts an asymptotic value of this deposition rate and the quantitative relationship between particle deposition and velocity fluctuation also may be computed incorrectly. Furthermore, experimental verification of this mechanism and rate will be critical in establishing confidence in the models. This work is proceeding in the same graduate research group but with a different student.

5.2 Coal/biomass combustion and deposition results

The first part of results includes the preliminary tests performed for setting up the test matrices and/or computer model runs. It also presents the additional results from the supplementary processes such as thermal treatment, particle screening, etc.

5.2.1 Preliminary test results

As described in the experimental set-up, the experimental tests are designed to simulate superheater sections in pulverized coal/biomass-fired boilers. The conditions representing such simulation include near-wall gas temperatures of approximately 1000 ^{o}C (corresponding wall temperatures of ~ 850 ^{o}C), heat transfer surface temperatures of 500-550 ^{o}C, residence time of about 1-1.5 s, and with 3-4% O_2 in exhaust gas stream. With these conditions as reference, the following plots show the MFR performance with respect to various parameters under investigation. Figure 37 shows a typical near-wall measured gas temperature and radiation-corrected gas temperature profile during ash deposition tests for a PRB (Caballo) coal in the MFR. The corrections

are estimated by performing a heat transfer analysis between the thermocouple bead and the surrounding hot gas and reactor wall (see Appendix D). Both profiles show a trend for flame development that peaks just above the middle of the reactor, with a slow decrease due to reactor heat loss. Overall, the corrected gas temperature profile confirms that the set of operating parameters maintains reactor temperatures at or above 1000 ^{o}C.

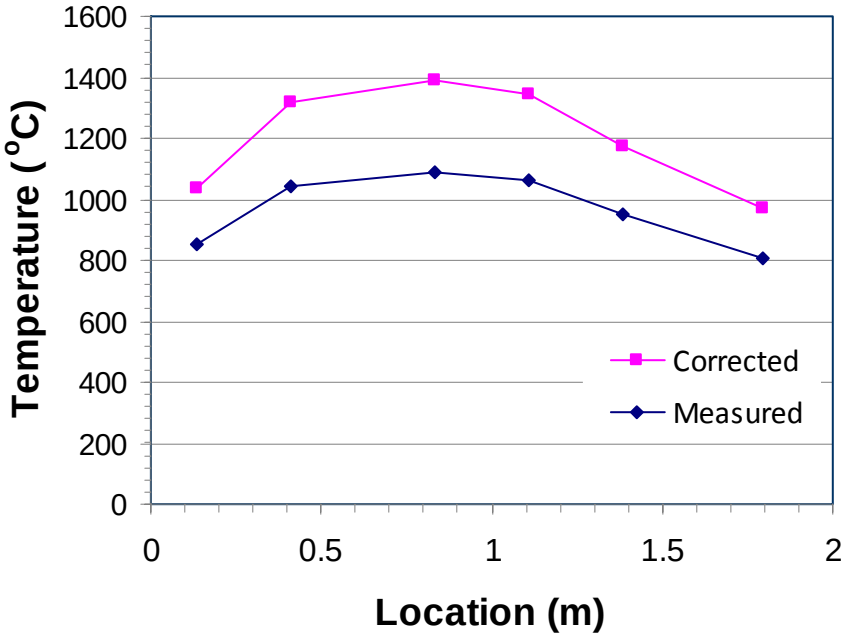

Figure 37: Thermocouple correction for MFR temperature profiles

Deposit surface temperature represents an additional important parameter apart from flow and stoichiometric parameters. The stainless-steel, air-cooled probe used in this investigation includes an assembly for continuous surface temperature recording. Figure 38 illustrates deposit probe surface temperature as a function time for three different cases: 1) straw firing with constant air cooling rate, 2) coal firing with constant air cooling rate, and 3) coal firing with varying air cooling rate. In the first and second

cases, as ash particles start depositing on the probe surface, the surface temperature decreases since cooling air flow is kept constant and the ash layer represents increased resistance to heat transfer. As shown in the fuel analyses tables, straw and Illinois#6 have very similar ash content; however, higher alkali chlorides in straw ash increase its deposition potential, which allows ash deposit thickness to grow faster in the case of straw than that in case of Illinois#6. As seen in the third case, the surface temperature remains constant by slowly decreasing the cooling air flow as the ash deposit thickness grows on top of the surface. In large-scale boilers, steam flow rates do not vary on a tube-by-tube basis, but soot blowers (external compressed steam cleaning lances) periodically remove deposits from different locations in the convection pass. Thus, overall steam temperature does not rise and flow rate does not change, but local steam temperature and tube temperature do change with time. Thus, Figure 38 illustrates how ash deposition adversely impacts overall boiler operation and efficiency.

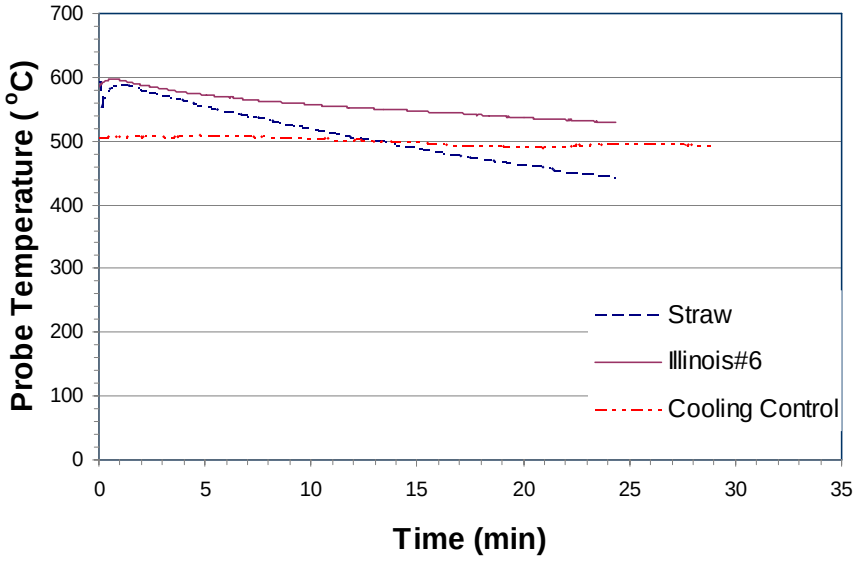

Figure 38: Surface temperature variation with ash deposit growth and air cooling

Exit gas oxygen and other major species concentrations remain constant by adjusting combustion conditions. They match those observed in large-scale combustion facilities. Figure 39 shows typical gas concentrations of O_2, CO_2, SO_X, NO_X and CO in a reactor exhaust stream during a coal combustion experiment. As mentioned earlier in the experimental procedure, O_2 concentrations are maintained at 3-4% vol. while other gas concentrations are at relatively steady values depending upon stoichiometry and fuel composition.

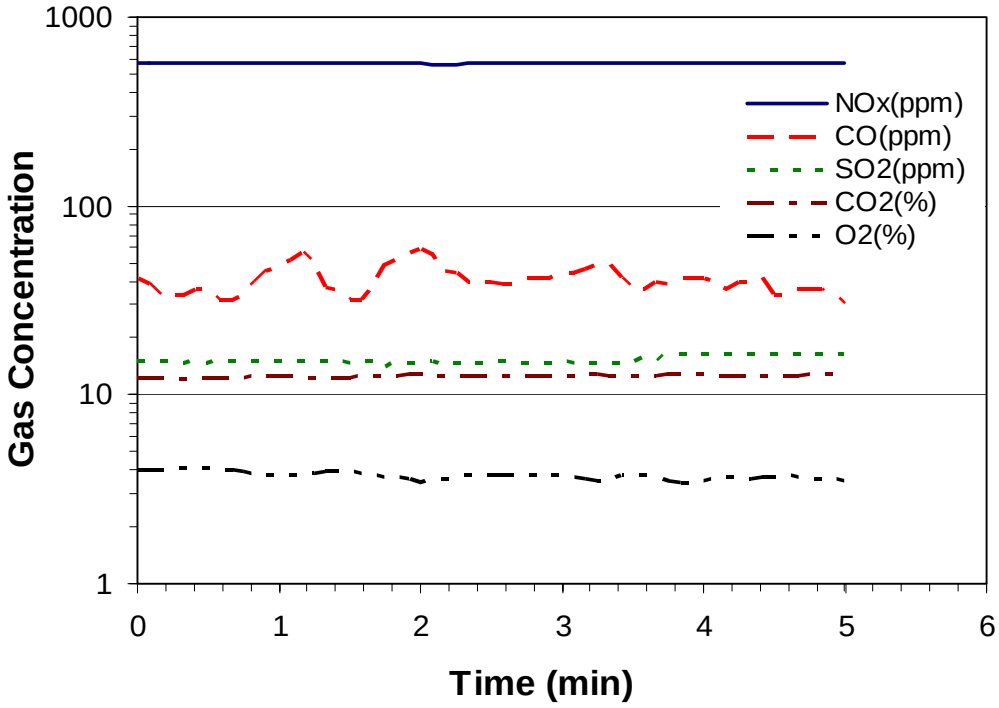

Figure 39: Typical exit gas concentrations for coal combustion tests

The Horiba PG-250 gas analyzer response time for CO is approximately 2 seconds longer than other gases; therefore, transient pockets of fuel-rich and fuel-lean zones passing across the sampling probe cause the fluctuations in the CO data that are

more apparent than those in other gas concentrations. Nevertheless, the CO concentration remains below an acceptable value of 100 ppm for significant part of the test period. NO_X concentrations seem fairly high (~500 ppm) compared to typical values in large scale boilers, but that is attributed to the fact that this reactor is not equipped with any kind of NO_X reducing techniques, such as low-NO_X burner or staging, etc for these experiments. SO_2 concentrations vary according to fuel type, coal or biomass, ranging from ~ 100 ppm for high-sulfur coals to < 10 ppm for biomass fuels. Accounting for these variations with respect to fuel type, typical concentration profiles for all combustion experiments in the MFR are similar to one shown in Figure 39. Thus, these important parameters are maintained closely to the parameters in many large-scale combustion facilities to perform the experiments and obtain ash deposition results in the form of ash collection efficiency, described earlier in literature review, which is a convenient measure to compare several fuels with varying ash content and composition. Figure 40 shows ash collection efficiency of several biomass fuels with widely varying ash content and ash composition. As the bar chart suggests, high-ash fuels like straw and grain screenings tend to have higher deposition potential than the saw dust with low ash content. Fuels like sugar beet pulp, sunflower shells, and shea nut shells have lower ash collection efficiencies than do straw or grain screenings despite having similar ash content. The different ash compositions of these fuels lead to this result. For example, straw has higher alkali and chloride contents than sugar beet pulp, and the presence of alkali chlorides enhance ash deposition potential of a fuel.

This set of preliminary results is an illustration of analyses performed on the outcome of various different combustion scenarios that are investigated in this project.

The main analysis is focused on ash deposition trends, however, in cases like oxyfuel combustion and/or combustion of thermally treated fuels. Temperature and NO_X behavior trends are also discussed but not analyzed. The following sections present in-depth discussions of such results from different combustion scenarios.

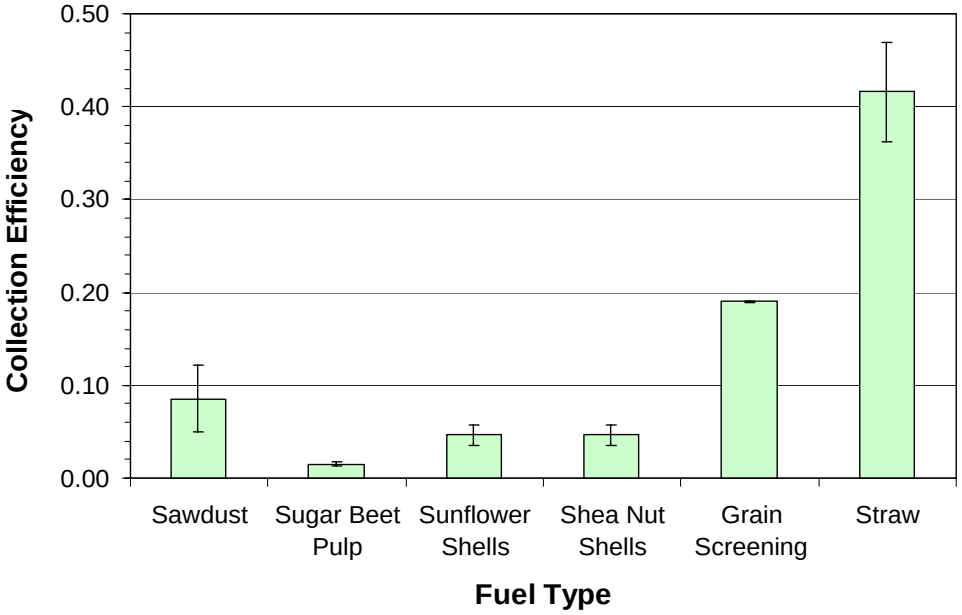

Figure 40: Ash collection efficiency of various fuels

5.2.2 Oxyfuel combustion

Oxyfuel combustion is one of the combustion techniques utilized for improving furnace efficiency and aiding CO_2 capture. The significant changes in an oxyfuel combustion environment compared to traditional combustion involve combustion gas composition. As opposed to traditional combustion, oxyfuel combustion involves less N_2 with corresponding increases in nearly all other gaseous species. Figure 41 and Figure 42 compare temperature profiles between traditional combustion and oxyfuel combustion with different O_2-CO_2 mixture ratios (25-75%wt., 30-70%wt., and 35-65%wt.) with

Illinois #6 and PRB coals, respectively. Temperature profiles for traditional combustion (air) and oxyfuel (25-75%wt.) are very similar due to fairly similar oxygen content in the oxidizer stream in both cases (Air-23%wt., Oxyfuel-25%wt.). The temperatures at the top of the reactor differ significantly from traditional (air) and oxyfuel (25-75%wt.) to oxyfuel (30-70%wt.) and oxyfuel (35-65%wt.). This observation supports the hypothesis that an oxyfuel environment accelerates ignition of coal particles. This phenomenon is a result of higher O_2/CO_2 volumetric ratio, increasing oxygen availability with less diluent (CO_2). As oxygen content increases, with the same stoichiometry, the peak flame temperatures increase as seen for the cases oxyfuel (30-70%wt.) and oxyfuel (35-65%wt.). Higher oxygen content and lower diluent (CO_2) compared to traditional combustion case (N_2) contribute to this rise in temperature. An opposite trend is observed at other end of the reactor, where temperatures for higher oxyfuel mixture ratios are lower than those for oxyfuel (25-75%wt.) and traditional combustion with air. Apart from the earlier heat release and higher temperature gradient between gas and reactor wall, CO_2 radiates more intensely than N_2 and adds to the rate of heat loss to the reactor walls. An earlier heat release in oxyfuel conditions also contributes to a greater heat loss resulting in lower reactor exit gas temperatures.

Oxyfuel combustion environments produce differences in combustion characteristics such as temperature profiles, NO_X behavior, and gas species compositions. However, oxyfuel combustion did not produce a significant difference in ash deposition rates. Figure 43 shows collection efficiency comparison for Illinois#6 and PRB coals in two different combustion environments. The error bars are one standard deviation.

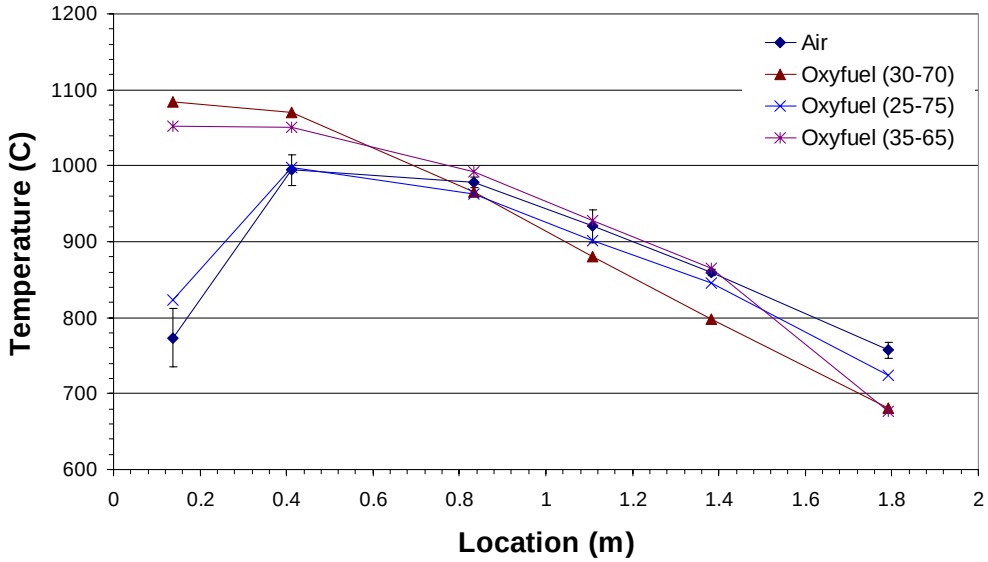

Figure 41: Temperature profile for Illinois#6 coal combustion

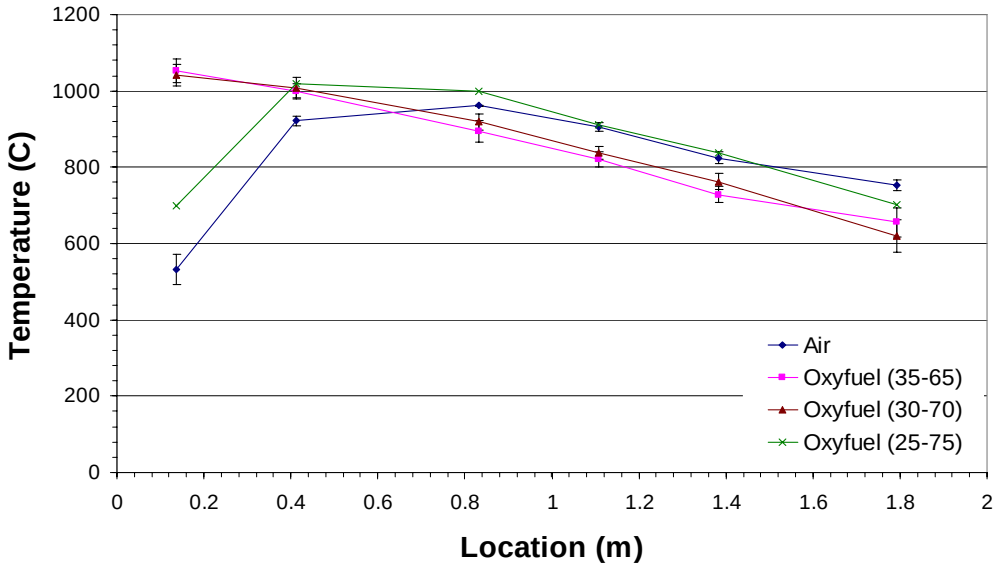

Figure 42: Temperature profile for PRB coal combustion

The collection efficiencies remain essentially unchanged. The experiments were conducted with an artificial recirculated gas however – one in which nitrogen was replaced by carbon dioxide but minor species compositions remained nearly unchanged. Specifically, sulfur dioxide concentrations did not change. This is a reasonable simulation

for oxyfuel systems in which gases for recirculation are extracted after the desulfurization unit. However, oxyfuel combustion installations in which recirculation gas is collected prior to desulfurization units would produce significantly higher sulfur dioxide concentrations in the furnace, which would lead to significant changes in ash sulfate content and possible changes in deposition rates.

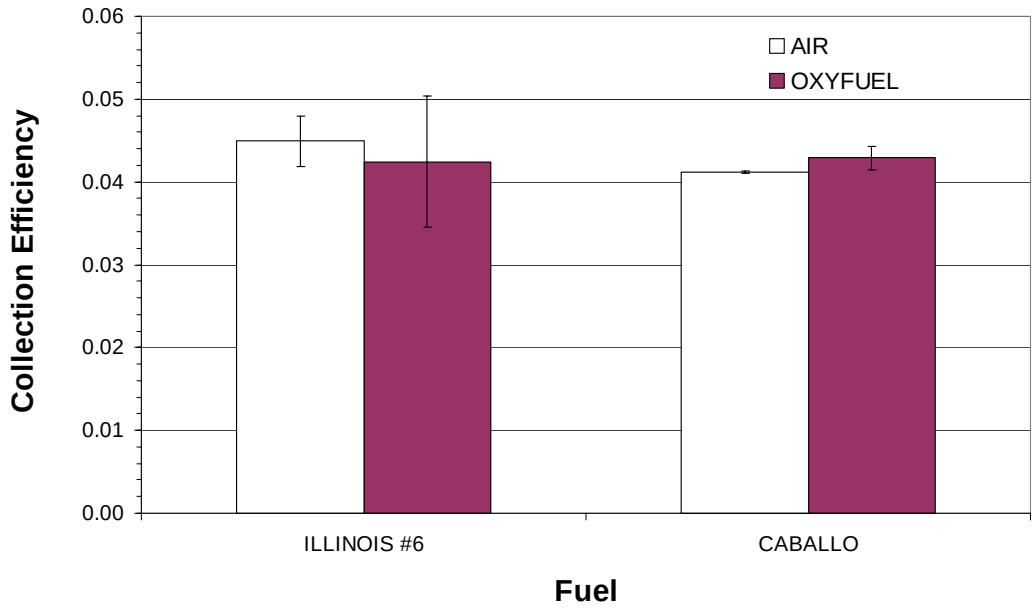

Figure 43: Ash collection efficiency comparison in air and oxyfuel combustion

5.2.3 Combustion of thermally treated pulverized coals

5.2.3.1 Coal treatment

Mercury emissions from coal-fired power plants represent a significant new environmental compliance issue. Most mercury control technologies involve post-combustion flue gas treatment. However, it is possible to vaporize mercury prior to combustion by warming the fuel to sub-reaction temperatures. Approximately 70% of the

mercury can be removed by this technique. The resulting coal is much drier and slightly chemically altered compared to the parent and typical coal. This section of the investigation focuses on pretreatment effects on ash deposition.

The coals were pretreated with two different methods. The first was a two-stage method that removes moisture at 150 ^{o}C (300 ^{o}F) followed by treating it at a higher temperature of 316 ^{o}C (600 ^{o}F) for mercury removal. The second method involves a single stage at 316 ^{o}C without the drying period. Figure 45 shows drying of PRB coal from Corderro mines followed by treatment at 316 ^{o}C. It appears to remove all the moisture (approximately 22%) and an additional 6% of the coal mass, the latter dominated by volatiles. Mercury content of coal is far too low to be detected by this type of gravimetric technique.

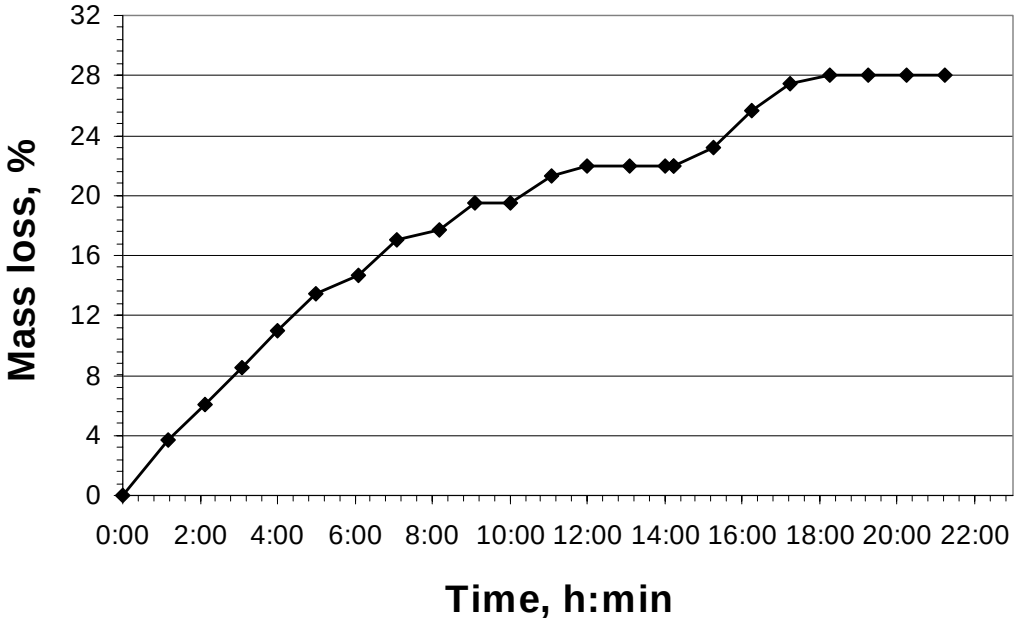

Figure 44: Drying and pretreatment of PRB (Cordero) Coal

Similar trends are seen in cases of PRB (Caballo) coals and lignites. In Figure 45, it is seen that even if the coal is treated directly at 600 ^{o}F without drying first and it is evident that direct treatment provides almost same mass loss as that in two-step treatment, but it only takes about one third of the time needed by the two-step treatment. Therefore, for further coal samples, the treatment was carried out without the preceding drying process, making the treatment less time-consuming.

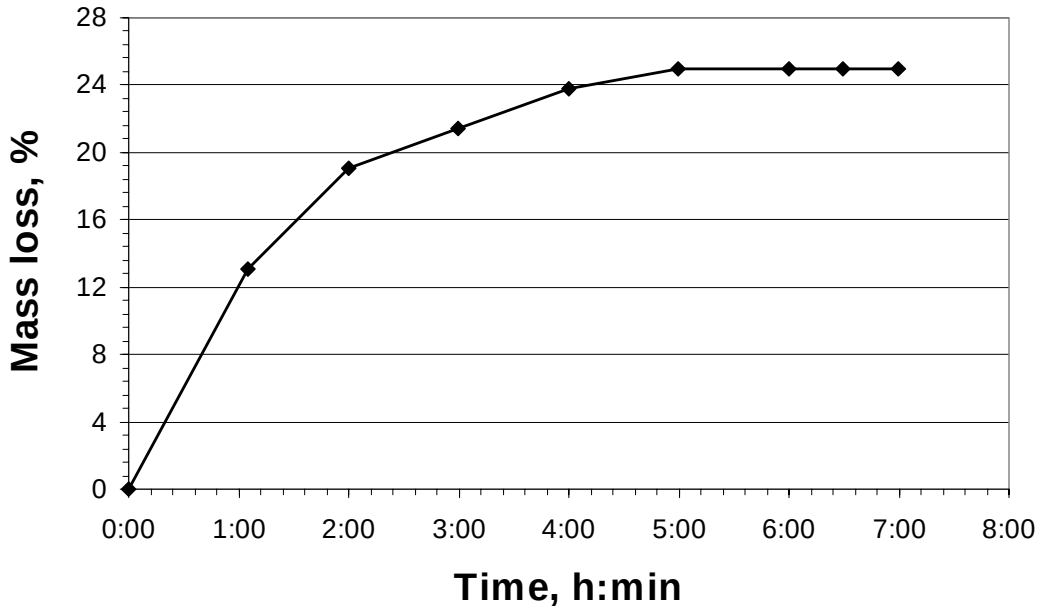

Figure 45: Direct treatment PRB (Cordero) coal for mercury removal

5.2.3.2 Temperature analysis

The near-wall gas temperature (thermocouple) histories for treated and untreated fuels appear in Figure 46, Figure 47, and Figure 48. These temperature profiles are averages of two separate temperature profiles obtained for each coal. The peak temperatures for treated fuels appear to shift downstream by compared to untreated fuels.

The shift is approximately 0.15 m for Caballo and Cordero coals, while for Lignite, it is ~ 0.4 m. The loss of volatiles due to treatment may delay the ignition of treated fuels. This shifts the peak gas temperature, which is closely related to the adiabatic flame temperature, to lower sections of the reactor. Also, loss of moisture during the treatment causes the treated fuels to have higher peak temperatures than untreated fuels.

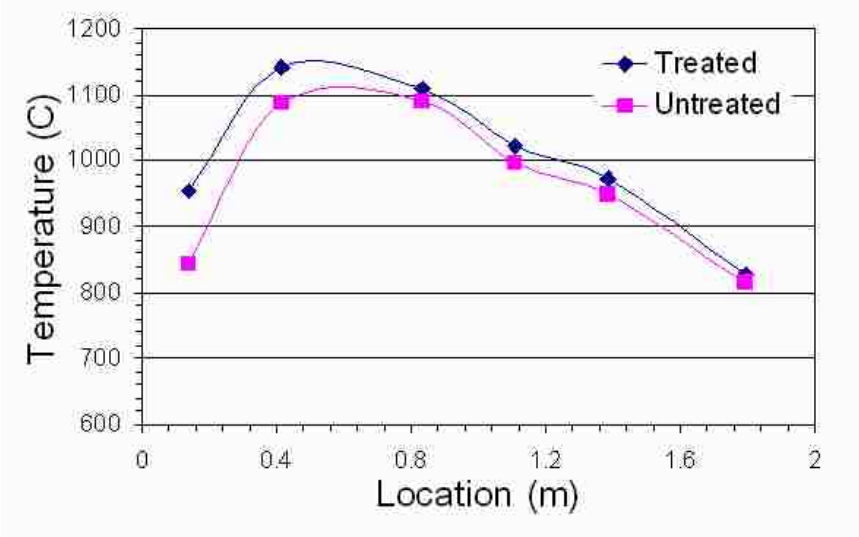

Figure 46: Temperature Profile for PRB (Caballo) coal

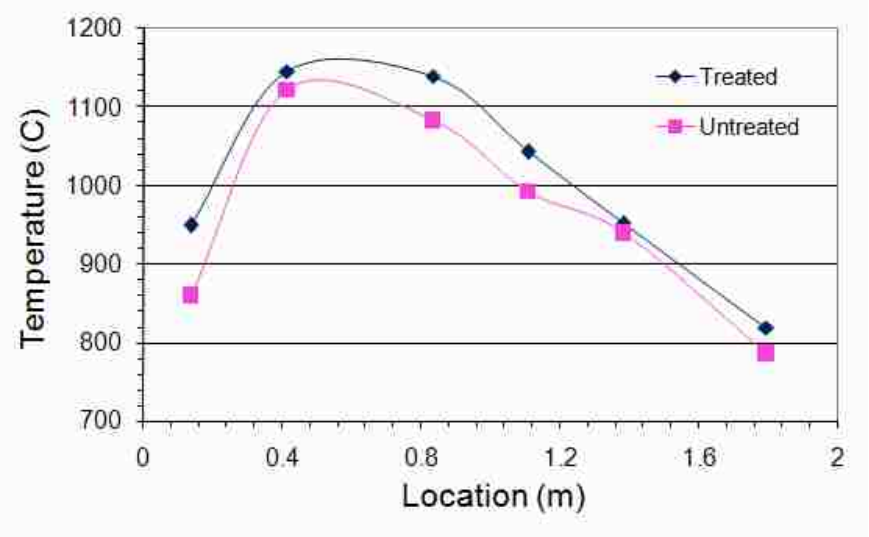

Figure 47: Temperature profile of PRB (Corderro) coal

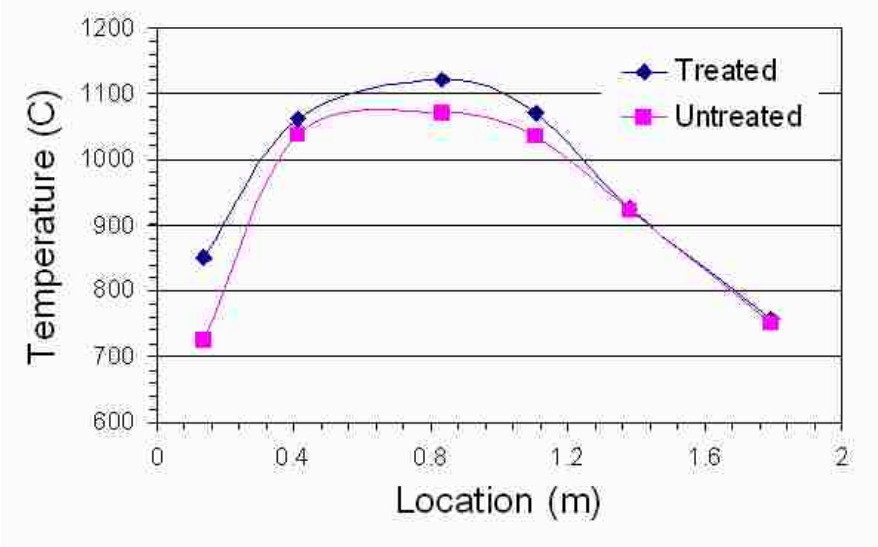

Figure 48: Temperature profile of Lignite coal

5.2.3.3 Ash deposition analysis

Ash deposits are collected on a deposit probe simulating the conditions in industrial boilers. The probe surface temperatures were maintained between 480-520 ^{o}C. Two deposition tests were run for each coal type. The ash deposition model described earlier in this section is used to analyze the data obtained from these tests.

Deposition behavior of the fuels under untreated and treated conditions is shown in Figure 49. The error bars represent one standard deviation. The deposition rate of treated PRB coals is slightly less than the untreated PRB coals, though the differences are marginally significant on a statistical basis. Lignites exhibit an obvious increase in collection efficiency of treated coal compared to untreated coal. In the previous subsection, the temperature profiles of treated and untreated lignite coals show that peak reactor wall temperatures for treated coal are attained at ~ 1 m from the burner, while that distance is approximately 0.4 m for the PRB coals. Thus, the hot ash particles produced from lignite coal combustion have lesser quenching time compared to that in case of the

PRB coal combustion. Therefore, more of the particles approaching deposit surface are in molten, sticky condition in lignite combustion case. This results in higher deposition potential for lignite ash compared to PRB coal ash.

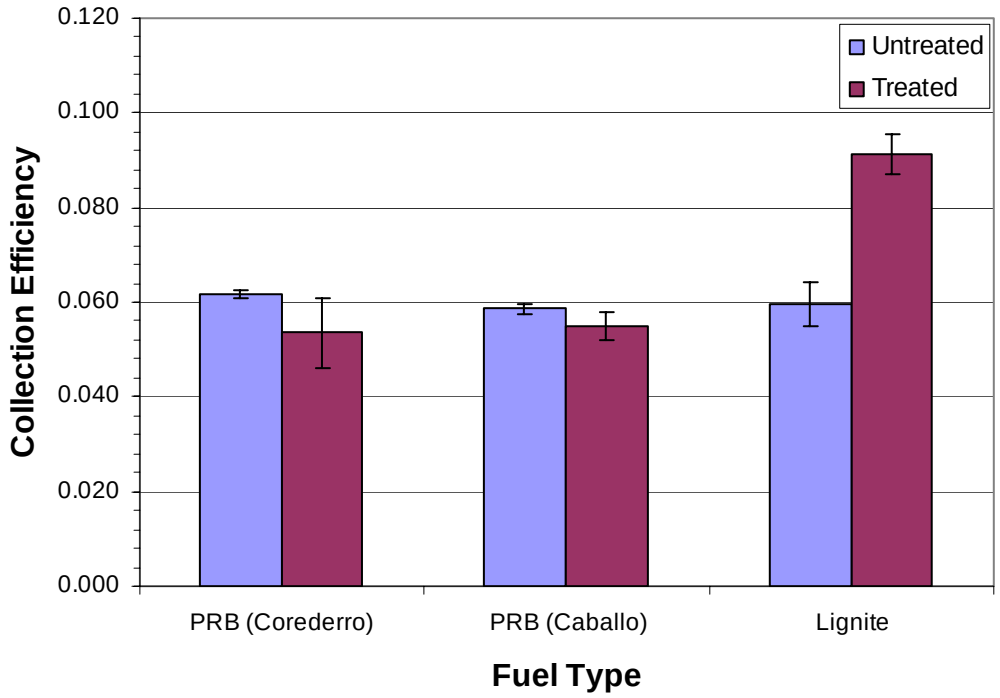

Figure 49: Ash deposition rates for untreated and treated fuels

5.2.4 Coal-straw cofiring

Cofiring techniques are widely used alternative for coal combustion to reduce emissions to an extent and also to reduce corrosion problems due to sulfur-chlorine chemistry. However, cofiring presents some challenges for ash deposition control as straw and coal have very different ash content and composition. This can be seen in the results obtained from cofiring tests. The errors bars in every plot are associated with one standard deviation. Figure 50 shows collection efficiencies for straw, Illinois#6 and Blind

Canyon when fired separately. As expected, Straw shows much higher collection efficiencies than two coals due to high potassium and sodium chloride content. Between two coals, Blind canyon has higher sodium and sulfur content than Illinois#6 which may result in deposition of sodium sulfate on the surface and enhance ash deposition.

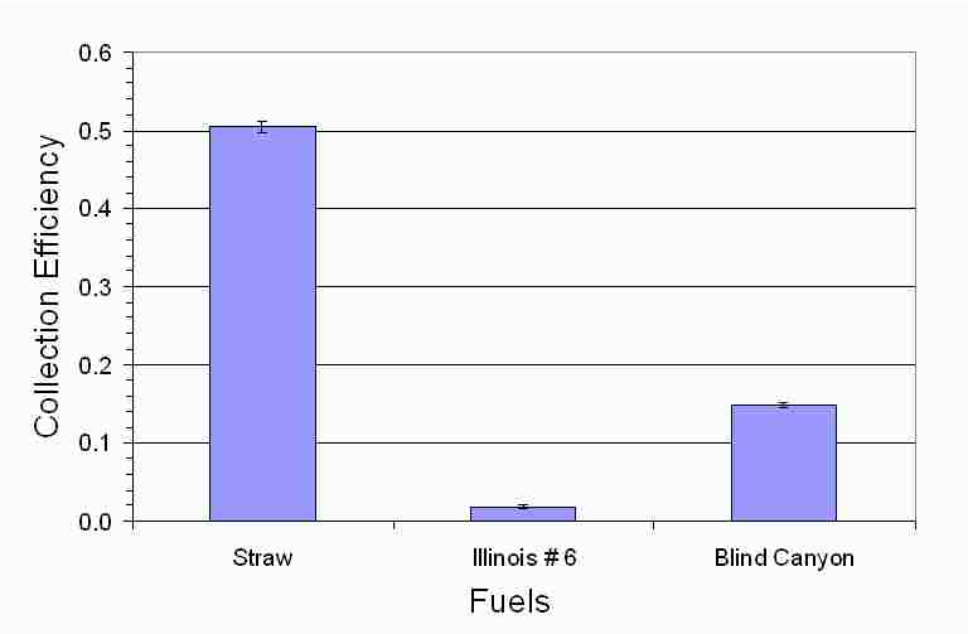

Figure 50: Collection efficiency of pure fuels

After mixing in two different ratios, 70-30% and 30-70%, the collection efficiencies for fuel blends are shown in Figure 51. In Figure 51, results from straw-Illinois#6 cofiring are shown where, from left to right, straw content goes from 100% to 0% and Illinois#6 goes from 0% to 100%. The trends shown by the experimental data are non-linear. This suggests that the collection efficiencies of fuel blends not only depend on the ash fraction but also on ash chemistry which results in lower collection efficiencies than those if it were controlled solely by ash mixture fractions of fuel blends alone. When

fitted to trend lines of exponential form, straw-Illinois#6 blends show very good agreement with the trend line form than straw-Blind Canyon blends.

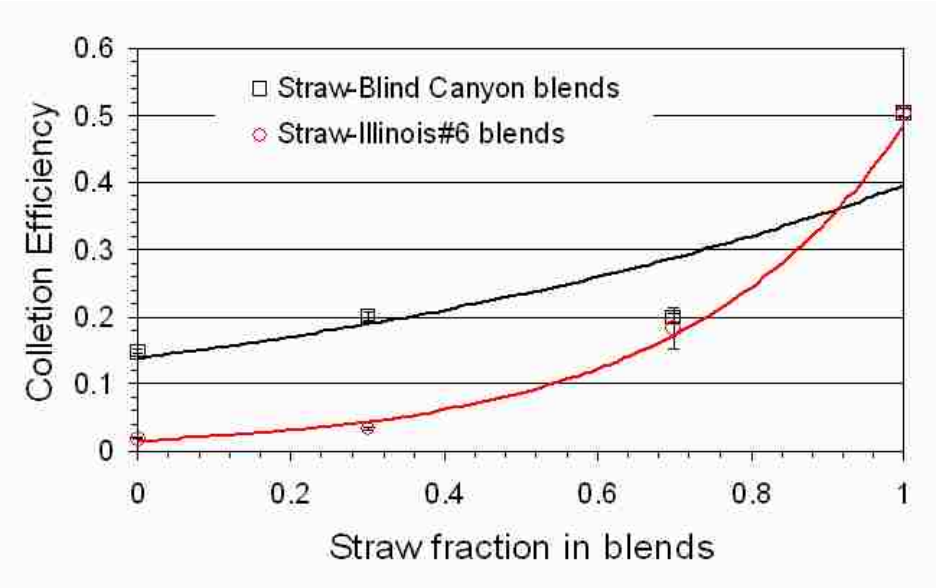

Figure 51: Effect of cofiring on ash collection efficiency

5.2.5 Combustion of biomass with additives

The R-series (Recipe) fuels are prepared by mixing one or two biomass fuels, an anti-slagging additive, a binding agent and a lubricant (see Table 13). Typical anti-slagging agents are aluminum hydroxide and limestone, while molasses is used as binding agent and rapeoil as lubricant. Addition of such substances can alter deposition behavior of these fuel ashes. In addition, the variety in ash content, results in varied ash particle size distributions for these fuels. Figure 52 presents fuel particle size distribution, while an estimated ash particle size distribution is shown in Figure 53. This estimation is based upon the assumption that each fuel particle produces a single ash particle.

Table 13: R-series fuels recipe information

Recipes	Biofuel 1	Biofuel 2	Anti-slagging Additive	Binding Agent	Lubricant
R1	100% Straw	--	1% $Al(OH)_3$	--	--
R2	100% Straw	--	2% Kaolinite	--	--
R3	100% Straw	--	1% CaO	3% Molasses	--
R4	33% Sawdust	67% Straw	5% Limestone	--	--
R5	33% Sawdust	67% Straw	5% $Al(OH)_3$	5% Molasses	--
R6	33% Sawdust	67% Straw	5% Limestone	5% Molasses	5% Rapeoil
R7	33% Sawdust	67% Grain Screenings	5% Limestone	5% Molasses	3% Rapeoil
R8	33% Sunflower Shells	67% Grain Screenings	5% Limestone	5% Molasses	2% Rapeoil
R9	33% Shea nut shells	67% Grain Screenings	5% Limestone	5% Molasses	2% Rapeoil
R10	100% Grain Screenings	--	5% Limestone	5% Molasses	2% Rapeoil
R11	33% Sawdust	67% Grain Screenings	5% Limestone	2% Molasses	2% Rapeoil
R12	33% Shea nut shells	67% Grain Screenings	5% Limestone	--	--

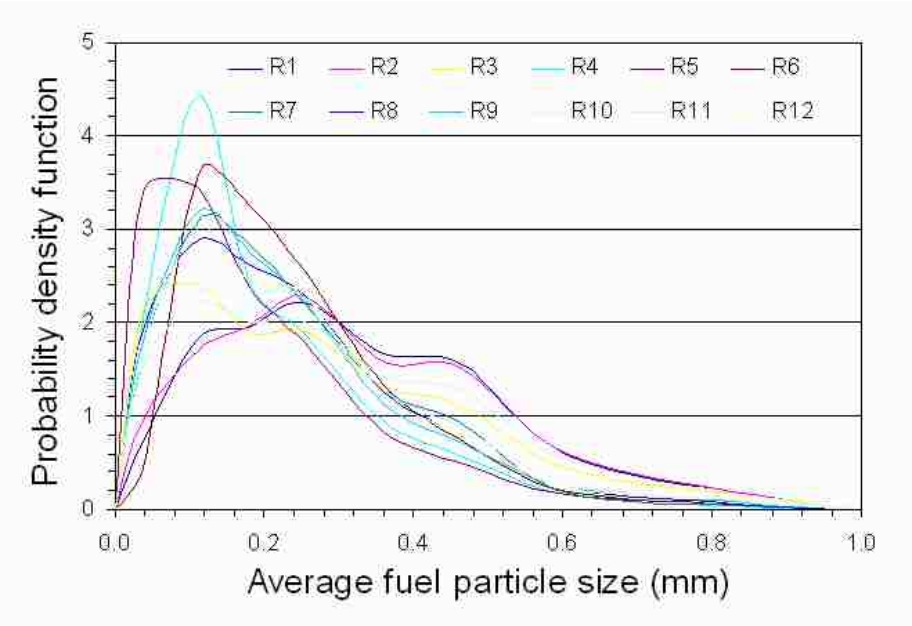

Figure 52: Fuel particle size distribution for R-series fuels

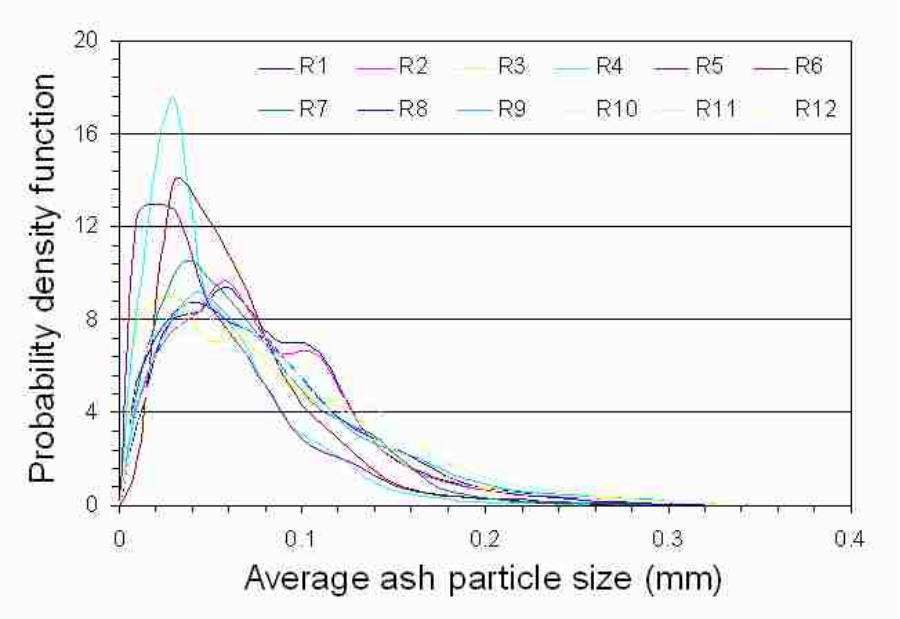

Figure 53: Ash particle size distribution for R-series fuels

The majority of fuel particles range from 50-500 microns, and produce ash particles ranging from 10-100 microns. However, the deposition behavior of the fuels does not correlate directly to ash content. Figure 54 shows behavior of collection efficiencies of recipe fuels measured from the experiments along with ash content of each fuel. Although ash content is fairly similar (8-9%) for all fuels, except for R8, R9 and R10 (>10%), collection efficiencies are different. A similar trend is seen for collection efficiency plots along with impaction efficiency (see Figure 55). For the first half of fuels (R1-R6), collection efficiency follows the impaction efficiency trend, while, for the rest of the fuels, it tends to follow an opposite trend. This can be explained by the fuel and ash composition and the role of additives. The first three fuels (R1-R3) are prepared with 100% straw and different anti-slagging additives. Straw has relatively higher silica, potassium and chlorine content than other biomass fuels. Higher silica content confirms higher levels of sintering during deposition while, higher potassium and chlorine indicate

deposition of chloride layer, enhancing early deposition rates. Here, collection efficiency decreases gradually from R1 to R3. This suggests that calcium oxide performs better as an anti-slagging additive than aluminum hydroxide or kaolinite. The other fuels (with an exception of R5) contain limestone as an anti-slagging agent due to which all fuel ashes show relatively higher amount of CaO, CO_2 and H_2O indicating higher levels of calcium and carbonates. In general, calcium carbonates contribute to brittleness of ash, making it easy to knock off and less sticky. Thus, the results indicate that limestone as an anti-slagging agent has a greater effect of decreasing collection efficiency than other agents such as aluminum hydroxide and kaolinite.

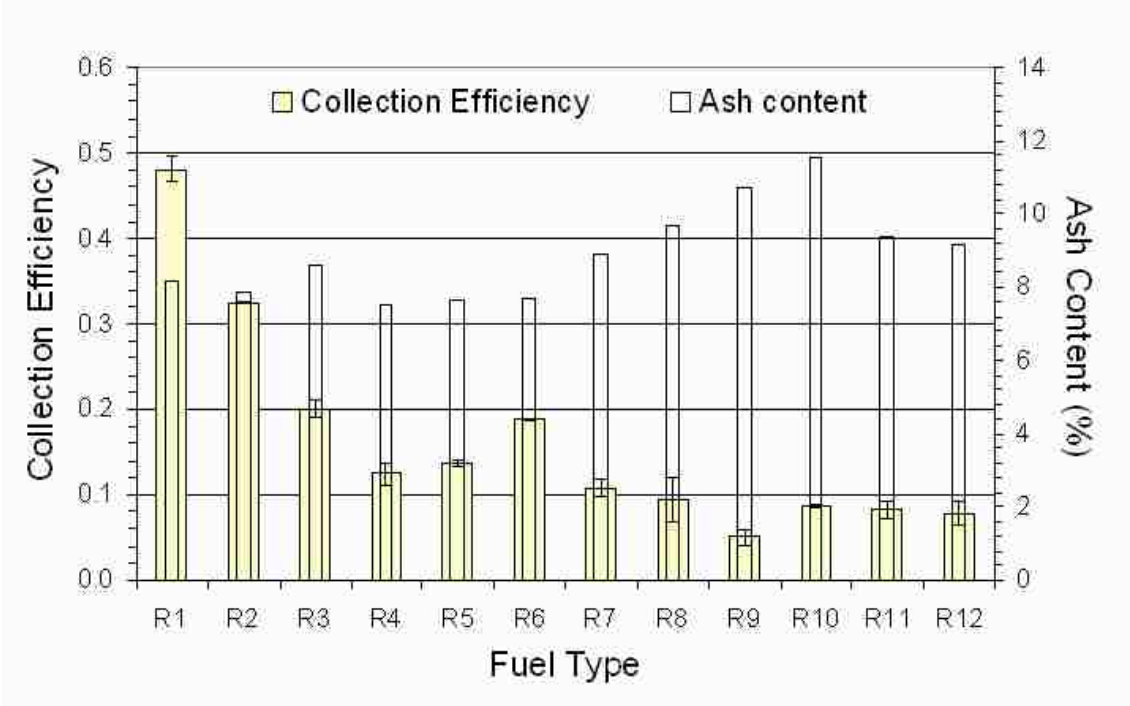

Figure 54: Collection efficiency and ash content of R-series fuels

The effect of adding molasses and/or rapeoil is apparent from comparison of R4 and R6. These two fuels have the same sawdust-straw combination and 5% limestone,

with only R6 having 5% molasses and 5% rapeoil. The difference in collection efficiencies of R4 and R6, which lies outside the limits of uncertainty, sufficiently indicate that addition of molasses and rapeoil increased R6's collection efficiency by approximately 40%. Recipes with grain screenings (R7-R12) have relatively lower collection efficiencies, despite being mixed with biomass fuels (sunflower shells, shea nut shells) containing higher ash than sawdust. This is attributed to lower collection efficiency of grain screenings than straw and overall less chlorine content of the fuels.

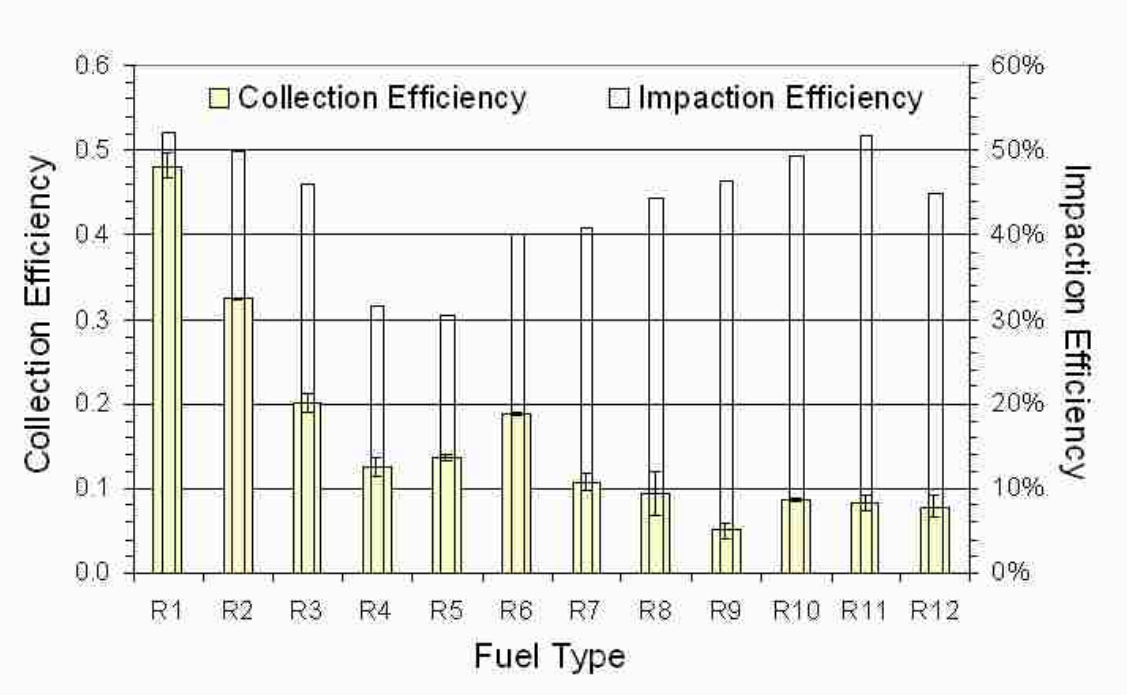

Figure 55: Collection and impaction efficiencies for R-series fuels

5.3 Ash deposition model validation

This section presents a complete ash deposition model that accounts for inertial impaction, condensation and eddy impaction. The various models described in earlier sections provide pieces of information, which is combined to predict overall ash

deposition rate for a fuel, coal/biomass. The ash deposition rate equation takes a form as shown below.

$$\frac{dm}{dt} = \dot{m}_{ash}\eta G + k_m cA \ln\left(1 + \frac{x_s - x_b}{1 - x_b}\right) + E \qquad 5.17$$

On the right hand side of above equation, the first term is associated with inertial impaction, second term accounts for condensation and third term accounts for turbulent eddy impaction. Ash flux is estimated from fuel feed rates, and concentrations, x_s and x_b, are obtained from chloride content of fuels.

Table 14 shows model predictions and experimental data for ash deposition rates from oxyfuel combustion tests. The model follows the experimental trend very well, however, overpredicts the deposition rate. This is partly due to the assumption that the bed particles are loosely connected. With this assumption, the impacting particle loses more momentum through bed particle displacement. In experiments, sintering forms bridges between particles. These bridges can be hard enough for rebounding particles with low momentum. Only particles with high momentum would be able to break these sintered particles, resulting in greater loss of momentum by the particle. Since the sintered bonds are strong, it is more likely that particles will bounce off. Thus, model captures some particles which may rebound after impact. Though very small, this effect is consistently seen in other deposition tests. In Figure 56, collection efficiencies predicted by new model are compared with the predictions from old model (Lokare 2003) and experimental data (Lokare 2003). The significant drop in predicted collection

efficiencies by the old model is attributed to improved impaction efficiency correlation in the new model.

Table 14: Model comparison with experimental data for oxyfuel combustion

Test	Ash deposition rate, gm/hr		Error
	Experiment	Model	
Illinois#6-Air	0.3992	0.4107	2.80%
Illinois#6-oxyfuel	0.3791	0.3874	2.14%
Caballo-Air	0.3499	0.3587	2.45%
Caballo-oxyfuel	0.3625	0.3722	2.61%

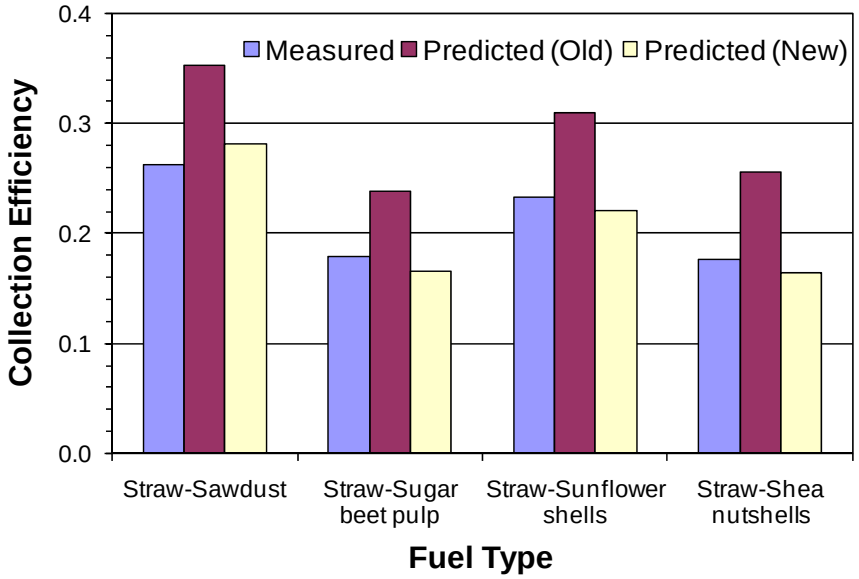

Figure 56: New model performance comparison with old model and experimental data

Figure 57 shows predicted and measured ash deposition rates for R-series combustion tests. For comparison, model prediction and measurement of ash deposition rate for straw is included since straw is a major fraction of many of these fuels. Thus for a fuel with no additives, the model predictions are in good agreement with experimental

data. For most of the recipe fuels, the difference in predicted and measured deposition rates is more significant than the difference between model and measurements for straw.

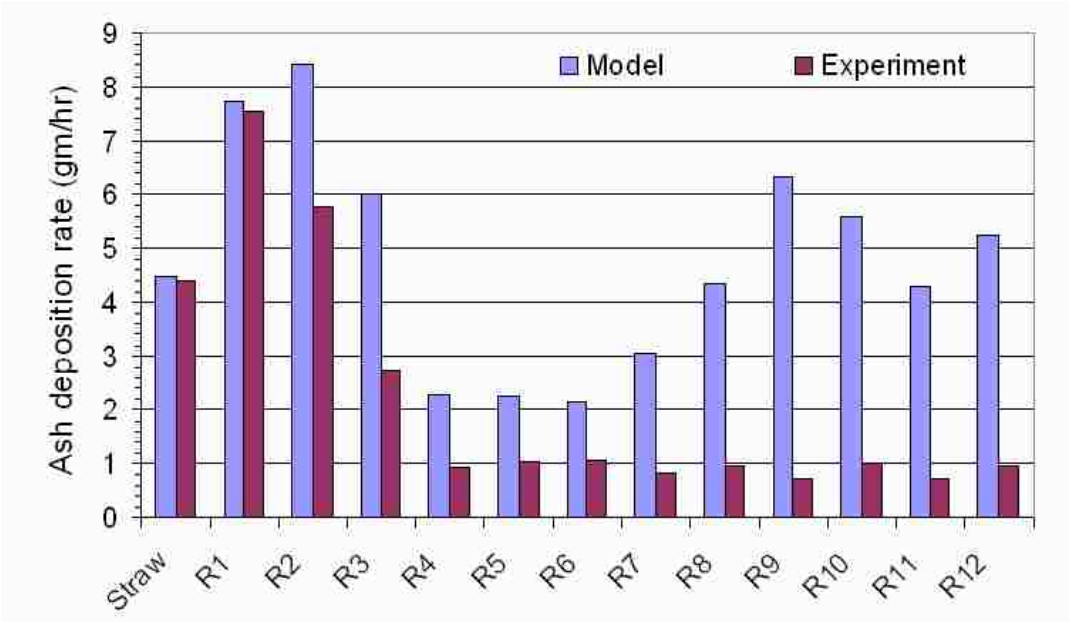

Figure 57: Ash deposition rates for R-series fuels: Model predictions and experimental data

Being the recipe fuels, each of these fuels have additives such as anti-slagging agents, binding agents, lubricants, etc. such materials may change ash chemistry to alter deposition behavior. For example, anti-slagging additives, as the name suggests, are added to decrease deposition potential of the fuels. This effect on the ash deposition rate is explained using composition of key compounds in ash (see Figure 58 and Figure 59). Chlorine is known to enhance ash deposition process by providing sticky, fine particulate layer by condensation. Higher chlorine contents lead to higher ash deposition. Figure 58 shows trend of chlorine content that is consistent with trend for ash deposition rate trend of each fuel. Though not completely, lower chlorine contents contribute to decrease in

ash deposition rate. However, significant reduction in ash deposition is achieved by anti-slagging additives as shown in Figure 59.

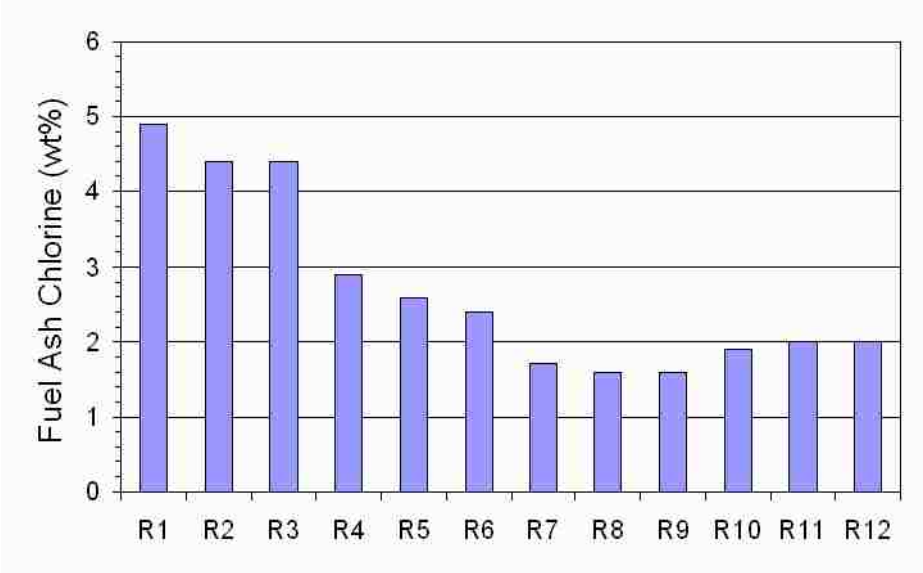

Figure 58: Chlorine presence in fuel ash for R-series fuels

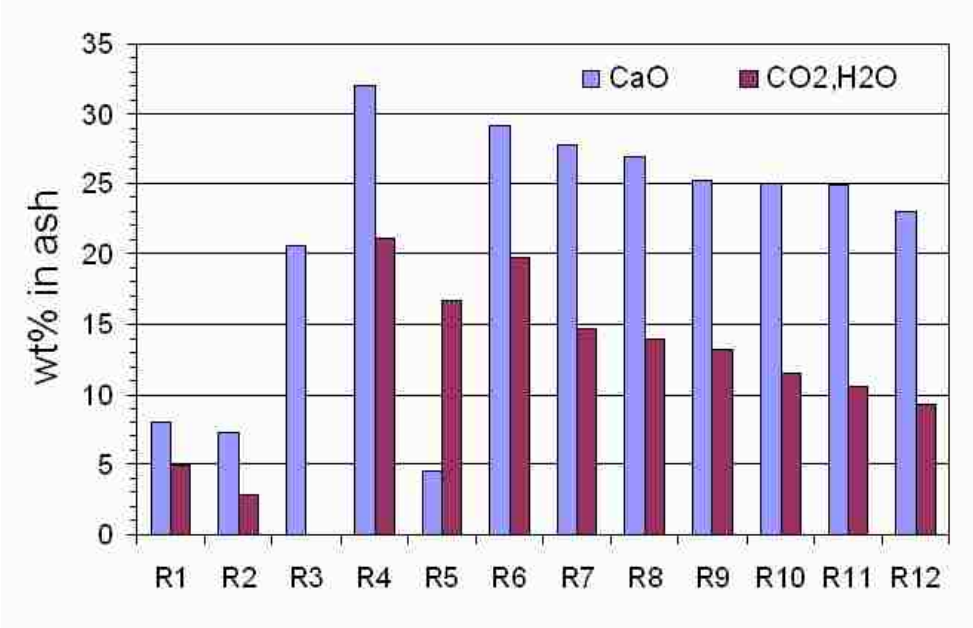

Figure 59: Role of carbonates as anti-slagging agent

Four types of anti-slagging additives were used while preparing the fuel suite. R1, R2 and R3 have 1% $Al(OH)_3$, 2% kaolinite, and 1% CaO as anti-slagging additives, respectively. From the ash deposition rates of these three fuels, it is clear that calcium is one of the main components affecting ash deposition mitigation. For more than half of the fuels (R4, R6-R12) limestone is used as anti-slagging additive. The addition is apparent in ash chemistry analysis in the form of CO_2 and CaO content. Calcium carbonate (Limestone) is known to increase brittleness of ash. Its hydrophilic nature keeps ash particles dry and less sticky, which reduces capture efficiency even further. This effect is exclusively illustrated by the difference in experimental data that accounts for additive chemistry, and the model results, which does not consider the chemistry of additives. Thus, ash deposition control is bettered by adding limestone to the fuels.

6 Summary and Conclusions

6.1 Summary

Experimental examinations of combustion conditions and fuel treatment effects on deposition mechanisms of coal/biomass ash in a pilot-scale reactor facility provide validation for a fundamental deposition model. Ash deposition rates from many fuel types (18 types of biomass, 10 types of coal, and 4 coal-biomass blends for cofiring) and varying combustion conditions, including traditional and oxyfuel conditions, represent a robust and comprehensive data for comparison. Replicated experiments provide a statistical basis for analysis. These deposition data help parameterize an ash deposition model that includes the mechanisms of inertial impaction, condensation, and eddy impaction. Individual mechanisms were also investigated using Fluent simulations (inertial impaction and eddy impaction), C++ programming (inertial impaction), and Microsoft Excel (condensation). Fundamental experiments performed in an entrained flow reactor isolated individual mechanisms except for eddy impaction.

Ash impaction efficiency depends on particle density and size while capture efficiency mainly depends on particle composition and surface type. Computed capture efficiencies for fuel blends based on mass-weighted capture efficiencies of pure fuels provide bases for comparison with experimentally determined fuel blend capture efficiencies. This work suggests substantial improvements relative to both widely used traditional deposition equations and commonly used deposition concepts.

6.2 Conclusions

The most significant conclusions derived from this investigation correlate with the major objectives of this project. Various subsections below present remarks on experimental evaluation of ash deposition potential of several fuels, fuel blends and combustion conditions, followed by the performance of individual mechanisms through experimental and model data. A section on comprehensive ash deposition model performance completes the conclusions on ash deposition. Comments on NO_X behavior under oxyfuel condition conclude this section.

6.2.1 Ash deposition experiments

- Oxyfuel combustion conditions do not affect ash deposition potential of the selected coals, Illinois #6 and PRB (Caballo). Oxyfuel conditions produce higher flame temperatures suggesting a probability of increased ash deposition owing to increased fraction of ash in a molten state. Although, flame temperatures are high, the gas temperatures drop faster in oxyfuel conditions than in traditional combustion, as indicated by wall temperature profiles (Figure 41 and Figure 42). Some proposed oxyfuel systems recirculate fly ash. These experiments did not provide fly ash recirculation and would not reflect the anticipated changes in ash residence time and loading as occur in recirculated conditions.
- Thermal treatment for removing mercury influences lignite deposition more significantly than subbituminous (PRB) coal deposition. The treatment removes a significant portion of volatile matter, which changes combustion behavior of fuels and in turn, the ash deposition potential.

- Coal-straw cofiring leads to reduced ash deposition relative to that of straw or of the linearly interpolated behavior between pure coal and pure straw behaviors. While ash deposition potential drops rapidly for straw mixture fraction < 0.8, cofiring with Illinois#6 presented a strong ash deposition correlation with mixture fraction, but cofiring with blind canyon coal presented a weak correlation.
- Recipe fuels show a strong influence of anti-slagging additives on ash deposition potential. Among all additives, the most successful anti-slagging additive was limestone. Dry and brittle properties of calcium and carbonates reduce sticking propensity of ash particles of such fuels and result in lower ash deposition potentials.

6.2.2 Ash deposition models

- Experimental measurements and independently conducted impaction efficiency analyses using Fluent indicate a reduction in impaction efficiency (up to 40%) relative to that predicted by a previous, widely cited correlation. The viscous effects, which were ignored in the previous analysis, significantly alter bulk flow streamline patterns in the region of a probe and in turn, trajectories of the particles approaching the deposit probe. An improved correlation for impaction efficiency as a function of Stoke's number provides a more accurate model for impaction efficiency and predicts the efficiency within 8-10% of experimental data.
- The C++ model predicts particulate capture on a rigid surface and a surface with a particulate layer. For a rigid surfaces, the model predicts inelastic collisions with no deformation and returns a coefficient of restitution, e ~ 0.9. These results are well supported by impaction data obtained under rigid-surface conditions. For

particulate layers, the model suggests an exponential decrease in rebound velocity with increasing number of particle layers on the surface. For a single layer, the model slightly overpredicts the experimental data due to its inability to account for chemistry and subsequent stickiness behavior, while for many layers (the number of layers depends on the particle size in the particulate layer), the assumption of loosely connected particle takes over to rapidly dissipate incident kinetic energy through particles in the layers.

- The condensation model successfully describes alkali salt condensation rate around the deposit probe and predicts alkali chloride flux within 15% of the experimental data. Model predictions generally exceed experimental data due to the fact that as condensation proceeds, increasing thickness of condensed layer adds to heat transfer resistance, subsequently raising the surface temperature (which was not modeled).
- The overall ash deposition model successfully predicts total ash deposition rates within 10% of experimental data on pure fuels, assuming the ash particle composition to be that of mullite. In all experimental conditions investigated here, particles should be relatively rigid, yet there remained significant variation in capture efficiency. For the first time, the effects of the deposit surface on capture efficiencies have been quantified and validated by comparison to data. However, there remains much work to do. A fundamental particle deformation model, more fundamental means of treating additives, and the remaining deposition mechanisms require additional research and are not developed in this work. The model does distinguish the effects of anti-slagging additives in recipe fuels on ash

deposition by showing the deposition rates differ from interpolations of the pure fuels. The model does not consider chemistry effects caused by anti-slagging additives, the fundamental exploration of which will be the subject of future work.

Appendix A

Following is a step-by-step procedure for operating entrained flow reactor. Please, refer to standard operating procedure (SOP) document for general safety regulations while operating the reactor

Startup for entrained flow reactor

1. Check the status of the reactor — power, gas, cooling water and temperature.
2. Turn on cooling water for feeding probe (inner water and outer water) and collection probe. (Adjust the opening of the valves for reasonable water flow rate)
3. Temperature control and measurement and power control
    a. Check the status of SCR power controller for top section, middle section, and bottom section.
        i. For the top and middle sections, the left knobs (BIAS) should be set as minimum (NEG).
        ii. For the bottom section, there should be four resistors installed on the UBS-100 solderless breadboarding socket (they are used to control the maximum power output to the transformer) the resistances are 325, 500, 500, and 270 Ω.
    b. Set the SV of the fuzzy logic temperature controller to desired value, usually 1200 ^{o}C for reactor and 1200 ^{o}C for preheater.

c. Set the ramp (heating rate) to 5 ^{o}C /min.

d. Turn off the power of fuzzy logic temperature controllers, then turn it on to reset the controllers.

e. Turn on the power of SCR power controllers: top section, middle section, bottom section, and preheater.

f. Use a clamp meter to measure the current in the cable for each section; the current should not exceed 160 A (maximum), otherwise the heating element could burn out.

    i. For the top section and middle section, if the maximum currents are lower than 100 A, use a screw driver to adjust the BIAS knobs; turn clockwise to increase, anti-clockwise to reduce.

    ii. During adjusting, watch the clamp meter, making sure the current won't exceed 150 A (safe value).

    iii. For the bottom section, the four resistors are used to adjust the power output; removing the resistor can increase the power output; to increase the power output, the resistors can be removed in order of 325, 500, 500, and 270 Ω.

g. During the heating up process, the power output for all of the top section, middle section, and bottom section need to be adjusted (usually increased) since the resistance of the heating elements keep changing (increasing) with the temperature increasing.

h. Nine thermocouples are used to measure the reactor wall temperature distribution and one is used to measure the preheater temperature.

4. Gas flow rate control and measurement

   a. Orifice plates are used to measure the gas flow rate for primary gas, secondary gas, quench gas 1, and quench gas 2.

   b. Ball valves are used to control the stagnant pressure before the orifice plates; the stagnant pressure is used to determine the gas flow rate (theory behind can be found in any fluid mechanics textbook).

   c. Turn on the primary gas valve and set the primary gas flow rate to a reasonable value, ensuring the biomass sample particles can be fed to the reactor through the feeding probe.

   d. Turn on the secondary gas value and set the secondary gas flow rate to a reasonable value, ensuring that particles can fall down to the bottom of the reactor (no back flow due to buoyancy or nature convection) and won't move too fast (which can reduce the residence time of the particles).

   e. Both c and d can be determined by experiments.

   f. Turn on the quench gas 1 valve and adjust the flow rate of the quench gas for the collection probe, ensuring that the char sample and exhaust gas can be quenched down to 50 ^{o}C.

   g. Turn on the vacuum and adjust the vacuum flow rate to a reasonable value, ensuring it can match the total flow rate of the hot gas (from primary gas and secondary gas) and quench gas; no extra gas (air) can be sucked into the system

through the porous SiC tube; the reasonable vacuum flow rate will ensure that the particles can be collected into the collection probe too.

5. Sample feeding and char collection

    a. Turn on the feeder controlling computer; the feeder control program should pop up; set the motor rate to 8 Hz at full step.

    b. Adjust the relative distance between the feeding probe and collection probe to obtain desired residence time.

    c. Clean the beakers below the two cyclone separators and make them ready for char collection.

    d. Fill the syringe with sample.

    e. Turn on the vibrator.

    f. Start feeding.

    g. During the feeding process, need to check the feeder, ensuring that the feeder won't get clogged.

    h. Once one run is finished, shut down the screw motor, then the vacuum, the quench gas, and the secondary gas.

Shutdown

1. Turn off SCR power controller for top, middle and bottom sections of the reactor.

    a. For the top and middle sections, the left knobs (BIAS) should be set as minimum.

b. For the bottom section, reinstall the four resistors into the breadboarding socket.

2. Set the SV of the fuzzy logic temperature controller to 0^{o} C.
3. Lower the collection probe out of the reactor. Turn of the cooling water and quench gas which flow through the collection probe.
4. Do not turn off the cooling water to the feeding probe until the reactor has cooled below 100^{o} C. This means that someone must return around two hours after the reactor has been turned off to turn off the cooling water to the feeding probe. Also, it is advisable to leave the primary gas on during the cooling period and turn it off when the cooling water is turned off.

Emergency shutdown

1. Turn off SCR power controller for top, middle and bottom sections of the reactor.

   a. For the top and middle sections, the left knobs (BIAS) should be set as minimum.

   b. For the bottom section, reinstall the four resistors into the breadboarding socket.

Appendix B

```
// Particle Impaction and Capture
// This program calculates rebound velocities for two particle
impaction scenarios:
// 1. Particle Impaction on Hard Surface, 2. Particle impaction on
powdery layer on a hard surface

#include <iostream>
#include <stdlib.h>
#include <math.h>
#include <stdio.h>
#include <fstream>
#include <time.h>


void main(void)
{
	std::ofstream fout1;
	fout1.open("output.txt",std::ios::ate);

	int i,j,k,c;
	double dp, d2, h, rho=2770, rho_part=1300.0, rho_gas=0.331;
	double vp, v1p, Vcr;   //particle velocities
	double mp, m_slag=100.0;   //particle mass
	double u[200][200], ms;

	int N;

	double R=8.314, pi=3.14159265;  //Constants

	double Tp=1100,Ts=800; //Temperature of particle and surface
	double Ep,Es;  //Young's Modulus of particle and surface material
	double nup,nus;//Poisson's Ratio of particle and surface material
	double KEi,KEr,KEloss;  //Kinetic energy of impacting and
rebounding particle and kinetic energy loss
	double A,B,C,D,E,k1,k2; //parameters involved in critical
velocity calculation
	double tf=0.004;   //exposure time in seconds
	double a1,a2,g=9.81;  //acceleration constants

	// Assign particle diameter

	std::cout<<"Enter Particle Diameter: ";
	std::cin>>dp;

	fout1<<"Particle Diameter\t"<<dp<<"\n";

	fout1<<"Particle Density\t"<<rho_part<<"\n"<<"Gas
Density\t"<<rho_gas<<"\n";
```

```
	mp=pi/6.0*dp*dp*dp*rho_part;// Calculate particle mass

	std::cout<<"Enter Particle Velocity: ";// Input particle velocity
	std::cin>>vp;

	fout1<<"Particle Velocity\t"<<vp<<"\nParticle Mass\t"<<mp<<"\n";

	std::cout<<"Enter Case type from following:\n";
	std::cout<<"1. Particle Impaction on Hard Slag Surface\n";
	std::cout<<"2. Particle Impaction on Powdery Layer\n";

	std::cin>>c;

	switch(c)
	{
	case 1:
		{
			std::cout<<"Case 1: Particle Impaction on Hard slag
surface\n";
			fout1<<"Case 1: Particle Impaction on Hard slag
surface\n";

		// Critical Velocity Calculation (Properties of Mullite)
			Es=(130.77+0.0701*Ts-0.00009*Ts*Ts)*1E9;
			Ep=(130.77+0.0701*Tp-0.00009*Tp*Tp)*1E9;
			nus=0.238;
			nup=nus;

			k1=(1.0-nus*nus)/pi/Es;
			k2=(1.0-nup*nup)/pi/Ep;
			A=5.0*pi*pi*(k1+k2)/4.0/pow(rho,1.5);
			E=0.51*pow(A,0.4);
			B=10.0/7.0;
			C=2.0*E/dp;
			Vcr=pow(C,B);

			KEi=mp/2.0*vp*vp;//Kinetic Energy of impacting
particle

			KEloss=mp/2.0*Vcr*Vcr;

			std::cout<<"Loss in KE :"<<KEloss<<"\n";

			KEr=KEi-KEloss;

			D=2.0*KEr/mp;

			v1p = sqrt(D);

			a1=v1p/tf;
			a2=a1-g;

			v1p=a2*tf;

			break;
		}
```

```
      case 2:
            {
                  std::cout<<"Case 2: Particle Impaction on Powdery
Layer\n";
                  fout1<<"Case 2: Particle Impaction on Powdery
Layer\n";

                  std::cout<<"Enter size of particle in powdery layer
(m):";
                  std::cin>>d2;
                  std::cout<<"Enter thickness of powdery layer (m):";
                  std::cin>>h;

                  fout1<<"Size of particle in powdery layer (m)\t"<<d2;

            // Critical Velocity Calculation (Properties of Mullite)
                  Es=(130.77+0.0701*Ts-0.00009*Ts*Ts)*1E9;
                  Ep=(130.77+0.0701*Tp-0.00009*Tp*Tp)*1E9;
                  nus=0.238;
                  nup=nus;

                  k1=(1.0-nus*nus)/pi/Es;
                  k2=(1.0-nup*nup)/pi/Ep;
                  A=5.0*pi*pi*(k1+k2)/4.0/pow(rho,1.5);
                  E=0.51*pow(A,0.4);
                  B=10.0/7.0;
                  C=2.0*E/d2;
                  Vcr=pow(C,B);

                  N=(h/cos(pi/6.0))/d2;

                  std::cout<<"\nNumber of particulate layers\t"<<N;
                  fout1<<"\nNumber of particulate layers\t"<<N;

                  int row=2*N-1;
                  int col=2*N-1;
                  int np=0;

                  for(i=N;i<=row;i++) // Total number of particles in
Impaction Zone
                  {
                        np=np+i;
                  }

                  std::cout<<"\nNumber of particles in impaction
zone\t"<<np;
                  fout1<<"\nNumber of particles in impaction
zone\t"<<np;

                  ms=pi/6.0*d2*d2*d2*rho_part;

                  u[1][1]=mp/ms*vp;

                  for(j=2;j<=row;j++)
                  {
```

```
                        u[j][1]=u[j-1][1]*3.0/8.0; //Left ramp
velocities
                        u[j][1]=sqrt(u[j][1]*u[j][1]-Vcr*Vcr);
//Kinetic Energy loss due to Impaction
                        u[j][j]=u[j-1][j-1]*3.0/8.0; //Right ramp
velocities
                        u[j][j]=sqrt(u[j][j]*u[j][j]-Vcr*Vcr);
//Kinetic Energy loss due to Impaction
                  }

                  for(k=3;k<=N;k++)
                  {
                        for(j=1;j<=k-2;j++)
                        {
                              u[k][j+1]=u[k-1][j]*3.0/8.0+u[k-
1][j+1]*3.0/8.0;
                              u[k][j+1]=sqrt(u[k][j+1]*u[k][j+1]-
Vcr*Vcr); //Kinetic Energy loss due to Impaction
                        }
                  }

                  for(j=1;j<=N;j++) //Kinetic Energy loss due to
Impaction between particles and surface
                  {
                        KEr=mp/2.0*(u[N][j]*u[N][j]-Vcr*Vcr);
                        D=2.0*KEr/mp;
                        u[N][j]=sqrt(D);
                  }

                  for(j=N+1;j<=row;j++)
                  {
                        u[j][1]=u[j-1][1]*3.0/8.0; //Left ramp
velocities
                        u[j][1]=sqrt(u[j][1]*u[j][1]-Vcr*Vcr);
//Kinetic Energy loss due to Impaction
                        u[j][j]=u[j-1][j-1]*3.0/8.0; //Right ramp
velocities
                        u[j][j]=sqrt(u[j][j]*u[j][j]-Vcr*Vcr);
//Kinetic Energy loss due to Impaction
                  }

                  for(k=N+1;k<=row;k++)
                  {
                        for(j=1;j<=k-2;j++)
                        {
                              u[k][j+1]=u[k-1][j]*3.0/8.0+u[k-
1][j+1]*3.0/8.0;
                              u[k][j+1]=sqrt(u[k][j+1]*u[k][j+1]-
Vcr*Vcr); //Kinetic Energy loss due to Impaction
                        }
                  }

                  v1p=ms/mp*u[row][N];

                  a1=v1p/tf;
                  a2=a1-g;
```

```
                v1p=a2*tf;

                if(v1p<=0.0)
                      v1p=0.0;

                std::cout<<"\nmp\t"<<mp<<"\nms\t"<<ms<<"\n";
                fout1<<"\nmp\t"<<mp<<"\nms\t"<<ms<<"\n";

                break;
          }
     }

     std::cout<<"Rebound Velocity\t"<<v1p<<"\n";
     fout1<<"Rebound Velocity\t"<<v1p<<"\n";

     std::cout<<"\n";
     fout1<<"\n";

     fout1.close();
}
```

Appendix C

The mechanism includes diffusion of NaCl vapors (> 800 ^{o}C) through air toward relatively cooler deposit surface (~ 500 ^{o}C). This diffusion process is described by following set of equations (Transport Phenomena, by Bird et al, p. 703-710):

$$N_{NaCl} = \theta_m k_m c \left(\frac{x_s - x_b}{1 - x_b} \right)$$

where,

$$\theta_m = \frac{\ln(1+R)}{R}, \text{ correction factor}$$

$$R = \frac{(N_{A0} + N_{B0})(x_{A0} - x_{A\infty})}{N_{A0} - x_{A0}(N_{A0} + N_{B0})}, \text{ flux ratio}$$

However, there is no counter-diffusion, and $x_{A0}=x_b$ and $x_{A\infty}=x_s$, R becomes,

$$R = \frac{x_{A0} - x_{A\infty}}{1 - x_{A0}}$$

Substituting R in θ_m, and subsequently substituting θ_m in N_{NaCl}, and simplifying, we get

$$N_{NaCl} = k_m c \ln\left(1 + \frac{x_s - x_b}{1 - x_s} \right)$$

Appendix D

Following is the EES program used to estimate thermocouple correction and corrected temperatures.

```
"Heat Transfer analysis for the correction Temperature of a Thermocouple"

T_t  =807+273   {K}
T_wall = T_t-150  {K}
DELTA_X = .15/2  {m}
V_air = 1.50 {m/s}
sigma = 5.667E-08 {W/m2K4}
"epsilon = 1.0"

D_wire = 0.0150*25.4/1000  {m}
A_cross_wire = 3.14159*D_wire^2/4   {m2}
k_wire = k_('Platinum', T_t)  {W/m-K}
D_bead = 3*D_wire
k_air = conductivity(air, T=T_film)
"k_air = .1"
A_sphere = 4*3.14159 *( D_bead/2)^2 {m2}


"Finding the Re and Nusselt number for the spherical thermocouple bead"

T_film = (T_gas + T_t)/2
rho_air = density(air, T=T_film, P = 85)
mu_air = viscosity(air, T=T_film)
Pr=prandtl(air,T=T_film)

Re = rho_air * V_air * D_bead / mu_air
Nuss = 2.0 +0.6*(Re)^0.5*Pr^.333
Nuss = h_air*D_bead/k_air

"Finding heat transfer"
q_cond = k_wire * A_cross_wire * (T_wall - T_t) / DELTA_x   {W}
q_rad = sigma * epsilon * A_sphere * (T_wall^4 - T_t^4)
q_conv = h_air * A_sphere * (T_gas - T_t)
             0   = q_rad + q_conv + q_cond
```

References

Andres, R. P. (1995). "Inelastic Energy-Transfer in Particle/Surface Collisions." Aerosol Science and Technology **23**(1): 40-50.

Bakker, R. R., Jenkins, B.M. and Williams, R.B. (2002). "Fluidized Bed Combustion of Leached Rice Straw." Energy and Fuels **16**(2): 356-365.

Baxter, L. L. (1993). "Ash Deposition During Biomass and Coal Combustion: A Mechanistic Approach." Biomass and Bioenergy **4**(2): 85-102.

Baxter, L. L. (1998). "Influence of ash deposit chemistry and structure on physical and transport properties." Fuel Processing Technology **56**(1-2): 81-88.

Baxter, L. L. (2000). "Ash Deposit Formation and Deposit Properties: A Comprehensive Summary of Research Conducted at Sandia's Combustion Research Facility - Final Report" Sandia National Laboratory, Livermore, CA**:** 92-118.

Baxter, L. L. (2005). "Biomass-coal co-combustion: Opportunity for affordable renewable energy." Fuel **84**(10): 1295-1302.

Baxter, L. L., Fletcher, T.H., Ottesen, D.K. (1988). "Spectral Emittance Measurements of Coal Particles." Energy and Fuels **2**: 423-430.

Baxter, L., G. Hatch, S. A. Sinquefield and W. J. Frederick (2004). "An experimental study of the mechanisms of fine particle deposition in kraft recovery boilers." International Chemical Recovery Conference, Jun 6-10 2004, Charleston, SC, United States, Technical Assoc. of the Pulp and Paper Industry Press, Norcross, GA 30092, United States.

Baxter, L. L., Lind, T., Kauppinen, E., and Robinson, A. (2001). "Thermal properties of recovery boiler deposits." International Chemical Recovery Conference, Jun 11-14 2001, Whistler, BC, Technical Assoc. of the Pulp and Paper Industry Press.

Baxter, L. L., Miles, T.R., Miles(Jr.), T.R., Jenkins, B.M., Milne, T., Dayton, D., Bryers, R.W., and Oden, L.L. (1998). "The behavior of inorganic material in biomass-fired power boilers: field and laboratory experiences." Fuel Processing Technology **54**: 47-78.

Brach, R. M., and Dunn, P. F. (1992). "Mathematical model of the impact and adhesion of microspheres." Aerosol Science and Technology **16**(1): 51-64.

Brach, R. M., and Dunn, P.F. (1998). "Models of Rebound and Capture for Oblique Microparticle Impacts." Aerosol Science & Technology **29**(5): 379-388.

Bryers, R. W. (1996). "Fireside slagging, fouling, and high-temperature corrosion of heat-transfer surface due to impurities in steam-raising fuels." Progress in Energy and Combustion Science **22**(1): 29-120.

Coda, B., Aho M., Berger R. and Hein, K.R.G (2001). "Behavior of Chlorine and Enrichment of Risky Elements in Bubbling Fluidized Bed Combustion of Biomass and Waste Assisted by Additives." Energy and Fuels **15**: 680-690.

Costen, P. G., Lockwood, F.C., and Siddique, M.M. (2000). Mathematical modeling of ash deposition in pulverized fuel-fired combustors. 28th International Symposium on Combustion, Jul 30-Aug 4 2000, Edinburgh, United Kingdom, Combustion Institute.

Das, S. K., Srikanth, S., Rao, D.S., Ravikumar, B., Nandakumar, K., Dhanuskodi, R., and Vijayan, P. (2003). "Combustion and deposit formation behavior on the fireside surfaces of a pulverized fuel boiler fired with a blend of coal and petroleum coke." Combustion Science and Technology **175**(9): 1625-1647.

Davis, R. H., Rager, D.A., and Good, B.T. (2002). "Elastohydrodynamic Rebound of Spheres from Coated Surfaces." Journal of Fluid Mechanics **468**: 107-119.

Dayton, D. c., Belle-Oudry, D. and Nordin, A. (1999). "Effect of Coal Minerals on Chlorine and Alkali Metals Released during Biomass/Coal Cofiring." Energy and Fuels **13**: 1203-1211.

Dayton, D. C., Milne, T.A. (1996). "Laboratory Measurements of Alkali Metal containing vapors released during Biomass Combustion." Applications of Advanced Technology to Ash-Related Problems in Boilers: 161-179.

Eisner, A. D., Rosner, D. E. (1986). "Experimental and Theoretical Studies of Submicron Particle Thermophoresis in Combustion Gases." PhysicoChemical Hydrodynamics **7**(2/3): 91-100.

Fan, J. R., Zha, X.D., Sun, P., and Cen, K.F. (2001). "Simulation of ash deposit in a pulverized coal-fired boiler." Fuel **80**(5): 645-654.

Green, J. H. (1994). "Trends and outlook for biomass energy." Energy engineering **91**(5): 18-28.

Hansen, L. A., Nielsen, H.P., Frandsen, F., Dam-Johansen, K., Horlyck, S. and Karlsson, A. (2000). "Influence of deposit formation on corrosion at a straw-fired boiler." Fuel Processing Technology **64**: 189-209.

Hein, K. R. G., Bemtgen, J.M. (1998). "EU clean coal technology- co-combustion of coal and biomass." Fuel Processing Technology **54**: 159-169.

Hein, K. R. G., Heinzel, T., Kicherer, A. and Spliethoff, H., Ed. (1996). Deposit formation during the co-combustion of coal biomass blends. Applications of Advanced Technology to Ash-Related Problems in Boilers, Plenum Press, New York.

Heinzel, T., Siegle, V., Spliethoff, H., and Hein, K.R.G. (1998). "Investigation of slagging in pulverized fuel co-combustion of biomass and coal at a pilot scale facility." Fuel Processing Technology **54**: 109-125.

Huang, L. Y., Norman, J.S., Pourkashanian, M., and Williams, A. (1996). "Prediction of ash deposition on superheater tubes from pulverized coal combustion." Fuel **75**(3): 271-279.

Israel, R. a. R., D.E. (1983). "Use of a Generalized Stokes Number to Determine the Aerodynamic Capture Efficiency of Non-Stokesian Particles from a Compressible Gas Flow." Aerosol Science & Technology **2**: 45-51.

Jenkins, B. M., Miles, T.R. Jr, Baxter, L.L. and Miles, T.R. (1998). "Combustion properties of Biomass." Fuel Processing Technology **54**: 17-46.

Jensen, P. A., Stenholm, M., and Hald, P. (1997). "Deposition Investigation in Straw-fired Boilers." Energy and Fuels **11**(5): 1048-1055.

Kantak, A. A., and Davis, R.H (2004). "Oblique Collisions and Rebound of Spheres from a Wetted Surface." Journal of Fluid Mechanics **509**: 63-81.

Kaufmann, H., Nussbaumer, Th., Baxter, L. and Yang, N. (2000). "Deposit formation on a single cylinder during combustion of herbaceous biomass." Fuel Processing Technology **79**: 141-151.

Konstandopoulos, A. G., and Rosner, D. E. (1997). "The initial sticking fraction of inertially impacting particles on cylindrical and spherical collectors." Journal of Aerosol Science **28**(SUPPL 1): 89-90.

Kweon, S. C., Ramer, Everett, and Robinson, Allen L. (2003). "Measurement and simulation of ash deposit microstructure." Energy and Fuels **17**(5): 1311-1323.

Lee, F. C. C., and Lockwood, F.C. (1999). "Modelling ash deposition in pulverized coal-fired applications." Progress in Energy and Combustion Science **25**(2): 117-132.

Lokare, S. S. (2003). Investigation of Ash Deposition and Corrosion Mechanisms in Combustion of Bio-fuels and Fuel Blends in a Pilot-Scale Facility. Chemical Engineering Provo, Brigham Young University.

Lokare, S. S., Dunaway, J. D., Moulton, D., Rogers, D., Tree, D. R., and Baxter, L. L. (2006). "Investigation of Ash Deposition Rates for a Suite of Biomass Fuels and Fuel Blends." Energy & Fuels **20**(3): 1008-1014.

Lokare, S. S., Dunaway, J.D., Rogers, D., Anderson, M., Baxter, L.L., and Tree, D. (2006). Effects of Fuel Ash Composition on Corrosion in Biomass-Fired boilers. Science in Thermal and Chemical Biomass Conversion, Victoria BC, Canada, CPL Press.

Lu, H. (2006). Experimental and Modeling Investigations of Biomass Particle Combustion. Chemical Engineering Provo, Brigham Young University.

Mackowski, D. W. (1990). "Phoretic behavior of asymmetric particles in thermal nonequilibrium with the Gas. Two-sphere aggregates." Journal of Colloid and Interface Science **140**(1): 138-157.

Mackowski, D. W. (1994). "Effect of Radiative Heat Transfer on the Coagulation Dynamics of Combustion-Generated Particles." Aerosol Science & Technology **20**: 83-99.

Nielsen, H. P., Baxter, L.L., Sclippa, G., Morey, C., Frandsen, F.J. and Dam-Johansen, K. (2000). "Deposition of potassium salts on heat transfer surfaces in straw-fired boilers: a pilot-scale study." Fuel **79**: 131-139.

Nielsen, H. P., Frandsen, F.J., Dam-Johansen, K. and Baxter, L.L. (2000). "The implication of chlorine-associated corrosion on the operation of biomass-fired boilers." Progress in Energy and Combustion Science **26**: 283-298.

Pyykonen, J. and J. Jokiniemi (2003). "Modelling alkali chloride superheater deposition and its implications." Fuel Processing Technology **80**(3): 225-262.

Robinson, A., Buckley, S.G. and Baxter, L.L. (2001). "Experimental Measurements of the Thermal Conductivity of Ash Deposit: Part 1. Measurement Technique." Energy and Fuels **15**: 66-74.

Robinson, A., Buckley, S.G., Yang, N. and Baxter, L.L. (2001). "Experimental measurements of the Thermal Conductivity of ash deposits: Part 2. Effects of Sintering and Deposit Microstructure." Energy and Fuels **15**: 75-84.

Robinson, A., Junker, H., Buckley, S.G., Sclippa, G. and Baxter, L.L. (1998). "Interaction between coal and biomass when cofiring." Twenty-Seventh Symposium (International) on Combustion/The Combustion Institute: 1351-1359.

Rosner, D. E. (1986). Transport Processes in Chemically Reacting Flow Systems. Stoneham, Butterworth Publishers.

Rosner, D. E., and Khalil, Y. F. (2000). "Particle Morphology and Knudsen Transition-Effects on Thermophoretically Dominated Total Mass Deposition Rates from "Coagulation-Aged" Aerosol Population." Journal of Aerosol Science **31**(3): 273-292.

Sami, M., Annamalai, K., and Wooldridge, M. (2001). "Co-firing of coal and biomass fuel blends." Progress in Energy and Combustion Science **27**: 171-214.

Smith, K. L., Smoot, L.D., Fletcher, T.H., and Pugmire, R.J. (1994). The Structure and Reaction Processes of Coal. New York, Plenum Press.

Srinivasachar, S., Helble, J.J., and Boni, A.A. (1990). "Mineral behavior during coal combustion. 1. Pyrite transformations." Symposium on Ash Deposition, Apr 1989 Progress in Energy and Combustion Science **16**(4): 281-292.

Srinivasachar, S., Helble, J.J., Ham, D.O., and Domazetis, G. (1990). "Kinetic description of vapor phase alkali transformations in combustion systems." Symposium on Ash Deposition, Apr 1989 Progress in Energy and Combustion Science **16**(4): 303-309.

Thornton, C., and Ning, Z.M. (1998). "A Theoretical Model for the Stick/Bounce Behavior of Adhesive, Elastic-Plastic Spheres." Powder Technology **99**(2): 154-162.

van Beek, M. C., Rindt, C.C.M., Wijers, J.G. and van Steenhoven, A.A. (2006). "Rebound Characteristicsfor 50-mu Particles Impacting a Powdery Deposit." Powder Technology **165**(2): 53-64.

Wall, S., John, W., Wang, H.C., and Goren, S.L. (1990). "Measurements of Kinetic-Energy Loss for Particles Impacting Surfaces." Aerosol Science & Technology **12**(4): 926-946.

Wall, S. M., John, W., and Goren, S. L. (1989). "Modified elastic-plastic impact adhesion theory applied to particle kinetic energy loss measurements." Proceedings of the 1989 European Aerosol Conference, Sep 18-23 1989 Journal of Aerosol Science **20**(8): 983-986.

Wall T.F., B. S. P., Baxter L.L., Young B.C. and Grisanti A.A., Ed. (1996). Ash deposit properties and radiative transfer in coal fired plant - Current understanding and new developments. Applications of Advanced Technology to Ash-Related Problems in Boilers, Plenum Press, New York.

Wall, T. F. (1992). Mineral matter transformations and ash deposition in pulverized coal combustion. Proceedings of the 24th International Symposium On Combustion, Jul 5-10 1992, Sydney, Engl, Publ by Combustion Inst, Pittsburgh, PA, USA.

Wall, T. F., Bhattacharya, S.P., Baxter, L.L., Richards, G. and Harb, J.N. (1995). "The character of ash deposits and the thermal performance of furnaces." Fuel Processing Technology **44**: 143-153.

Wall, T. F., Bhattacharya, S.P., Zhang, D.K., Gupta, R.P., and He, X. (1993). "Properties and thermal effects of ash deposits in coal-fired furnaces." Progress in Energy and Combustion Science **19**(6): 487-504.

Wang, H. and J. N. Harb (1997). "Modeling of ash deposition in large-scale combustion facilities burning pulverized coal." Progress in Energy and Combustion Science **23**(3): 267-282.

Wessel, R. A. and L. L. Baxter (2003). "Comprehensive model of alkali-salt deposition in recovery boilers." Tappi Journal **2**(2): 19-24.

Zbogar, A., F. J. Frandsen, P. A. Jensen and P. Glarborg (2005). "Heat transfer in ash deposits: A modelling tool-box." Progress in Energy and Combustion Science **31**(5-6): 371-421.